Compton Imaging for Homeland Security

Thesis submitted in accordance with the requirements of
the University of Liverpool for the degree of Doctor in Philosophy
by
Anthony Sweeney

April 2014

Abstract

This work marks the first use of a fully digital trigger system and new CAEN V1724 digitisers to create a Compton camera from two semiconductor double sided strip detectors. The system was designed to be able to identify and locate gamma ray emitting radionuclide within an energy range of 60 to 1408keV. Compton images were produced at AWE Aldermaston and the University of Liverpool across an energy range of 80 to 1408keV, using point sources, extended sources and also including special nuclear materials. The image at 80keV is the lowest recorded energy for a Compton image using a two detector cryogenically cooled Compton camera. GAMOS simulations have been used to check the experimental data and provide evidence that indicates if pulse shape analysis was applied to the experimental data the image resolution would be improved by up to 4mm at 662keV.

Contents

List of Tables

List of Figures

Acknowledgement

Well it appears, viva pending, that things have come to an end. The inevitable thank yous must be said, after all a PhD is never done single handedly! To start thanks must be said to my supervisors, Andy and Helen Boston, who looked after me and kept me going despite a few setbacks along the way! Thanks for your advice, guidance, the drinks around the pool bar in Florida and the many trips to UnI.

Thanks also need to go to the rest of the academic staff in the nuclear group, in particular Paul, Robert, Dave, Pete and Rodi. Your advice on presentations, writing and help while demonstrating on multiple courses was always appreciated. In addition without John Creswells help via email the work at Aldermaston could never have been carried out with the new electronics! Dave Seddon should also be thanked for designing and building the frame for Aldermaston, though I do apologise for losing the screw that made it work properly.

Thanks to Dan and Laura, I am sure you will not miss the pestering through my PhD! In particular thanks for those no doubt seemingly endless hours of proof reading Dan! The nights out also helped during the long three years. Also in the list of postdocs, for their help thanks to Scraggo, Ste and John though the help from John was more on the drinking side. To the other students, thanks for your help, sage (at times anyway, Drummond I am looking at you!) advice and the nights out! You shall all be remembered and are welcome to meet up for a pint or two at any time, to mention but a fewSlee, Heidi, Danny, Mark, Jonesy, Faye, Sam, Jamie, Pete,Pete Wu, Bahadair, Mo, the Joes and Carl . This list is not extensive and if I have missed your name out I do apologise, but know I will also remember you!

Thanks must also go to the staff at Aldermaston and Burghfield, in particular the members of NNS who aided on the project. Paul, Bob, Mark and Caroline thanks for all your help, despite leaving me alone for almost a week in Burghfield! It was an experience working at AWE and one I may look to repeat one day, if any of you are up around Oxford/Newbury let me know and we can go for a pint. Also while working onsite I was looked after superbly by the staff of the Hinds Head who appeared to feel sorry for this young lad working there alone for three months! Thanks to Shaun, Sue and Sonia for looking out for me, waiting up on a Sunday night for my arrival more often than not with a nightcap ready as soon as I arrived, your hospitality made the

pub a home away from home. Lastly there are a number of people who I would not have been here without and some who helped along the way with pokes, kicks and the occasional scream! Thanks to my parents, brother sister in law and the rest of my family (far too many of you to name) you have been a constant support throughout both the masters degree and PhD as well as being there in the years before despite hard times. To the Houghton family, thanks for all the Sunday dinners, advice and the pokes along the way. At least now I am too far away to turn up expecting to be fed every week, though the downside is not getting mobbed by four dogs!

To Sarah, my rock, thanks I owe you for pushing me through the difficult times and actually making me finish something! Thanks to the woman I love, three years of looking after a PhD student and even pushing him to job hunt before finishing, no idea what I did to deserve you but happy your there.

To the rest of my friends away from Liverpool, thanks for generally being there before, during and after the last four years! Sunain we need another Freddie Mercury impression in a kilt from you, Joe you are insane but always present, those at the rec who put up with me for years on both sides of the bar, the old crew from Glasgow now scattered to the winds (you know who you are) without whom I would not of got a degree in the first place, Andy the other ginger from school, the rest of the survivors from St. Nichs and lastly the mad ninja Greek Stavros who made my masters possible and enjoyable hope Oxford has survived since you moved down!

Think that is it. PhD and student life are now over, already I am working for a living so the final thank you should go to Helen and Mike from Nuvia, after all they now have to put up with me!

"Learn from yesterday, live for today, hope for tomorrow. The important thing is not to stop questioning." Albert Einstein

"Both the man of science and the man of action live always at the edge of mystery, surrounded by it." J. Robert Oppenheimer

Chapter 1

Introduction

Governments that have signed up to the International Atomic Energy Authority (IAEA) treaties now have an obligation to monitor the movement of nuclear materials across their borders and also within the territories they are responsible for. The signatories are asked to pay particular attention to special nuclear material (SNM), which are fissionable materials and related material such as ^{235}U, ^{233}U and the plutonium isotopes. These types of material are the main radioactive components in conventional nuclear weapons.

In 1996 the IAEA published the reported number of events involving nuclear materials being moved illicitly across borders that had been reported since 1993 [1]. This report identified 168 events where material was found being trafficked illegally, including a number of events involving the shipment of SNM. Within the United Kingdom the emphasis for enforcing the regulations regarding shipment of nuclear materials falls on the Office for Nuclear Regulation (ONR) while the United Kingdom Border Force (UKBF) provide the first line of defence with regard to detecting illegal smuggling of nuclear material into the UK. The Atomic Weapons Establishment (AWE) based at Aldermaston and Burghfield are the technical authority for radiological and nuclear (TARN) to the UKBF.

The detection of other illicit materials is also of concern to governments as radiological material is used within hospitals, building sites, homes and research facilities. This material is not directly usable in a device, however it could be used in a so called dirty bomb. A dirty bomb is created by packing radioactive material around an explosive device, the material is then subsequently scattered across an area by the explosion created. This is seen as a likely root for terrorist groups to take given the restrictions and monitoring placed on known stockpiles of SNM. Radioisotopes that are commonly used within areas easily accessed by the public are of primary concern, for example sources used within hospital radiotherapy or radio imaging departments which would include ^{137}Cs, ^{60}Co and ^{99m}Tc. This work will concentrate on the detection of gamma-ray emitting nuclides, these are only one area of interest and in truth a combination of neutron,

gamma-ray, beta and alpha particle detection is required to allow the identification of all materials of interest.

Current gamma-ray detector technologies provide a means to do this though they are limited. Detectors that provide an indication of the presence of gamma-ray radiation are readily available and deployed by numerous agencies worldwide, the majority are based on scintillator detectors due to their low cost, high detection efficiency, reliability and ease of maintenance. The ability of the detector to identify the nuclides present may be poor due to the relatively low resolution for the most readily available scintillator materials, when compared to the resolution of semiconductor detectors. The ability to locate the source of radiation can be provided by a heavily collimated detector system though these tend not to be available to the front line agencies due to their cost.

Collimation reduces the detection efficiency of the system used, by using electronic collimation a Compton camera can make use of more of the incident gamma-rays while providing a location for the source. Using semiconductor detectors will provide a system that has good energy resolution which will enable it to identify multiple nuclides and locate them individually. A combination of electronic collimation and also the use of semiconductor detectors is therefore advantageous and would improve upon the current detector technology.

1.1 AWE

AWE exist primarily to maintain the existing nuclear weapons inventory in the UK and also to maintain the ability to design and manufacture a weapon system if the government requests it. The company is now privately run, with the Ministry of Defence as its primary customer.

In addition to their primary role, AWE also provide technical assistance to the front line services enforcing the IAEA treaties, is the TARN for the UKBF and also as part of the wider international community. This assistance takes the form of expertise in the detector systems required to locate any illicitly transported material along with a research team working on the latest detector technology. The research is lead by the National Nuclear Security (NNS) group and the work presented here was carried out in partnership with the Enhance Detection team.

AWE involvement in this project allowed the University of Liverpool to gain experience working with an industrial partner including access to SNM on the Aldermaston site. AWE gained knowledge on the use of state of the art digital electronics and the use of research grade detectors alongside the experience of using a new detector technology.

AWE require an imaging system that can identify the radio nuclides present as well as their position within an object. By looking at the shape of the radioactive component present it may be possible to identify the threat type, whether a suspect device is actually a conventional nuclear warhead or a so called dirty bomb. The

identification of nuclides present can be used to provide evidence of this and may also provide the ability to check shipments of radioactive material for unidentified nuclides which may have been placed within a shipment.

1.2 Research work

The Compton camera detector system was first theorised in these papers, [2, 3]. New detector technologies and also the accessibility of high powered computers has allowed Compton cameras to be developed for medical and also defence requirements, examples can be found in[4, 5]. Convential gamma cameras use a heavy metal, typically lead or tungsten, collimator to provide the position of the gamma ray source. This method removes up to 99% of the incident gamma rays before they reach the detector, a Compton camera however uses an electronic collimation method removing the need for the metal collimator and hence increasing the detection efficiency. The field of view of a collimated device is also small, requiring the detector to be scanned across an area slowly to identify the source, a Compton camera has a 2π field of view allowing offline sources to be located and can also provide information on the distance to the source.

AWE requested that a Compton camera was designed and built by the University of Liverpool. This detector system was then used both at Aldermaston and Liverpool to produce images of a variety of sources including SNM. Within this work images taken at Aldermaston and Liverpool for initial testing of the system will be presented. The results include raster scans across the detector face, showing the effects of a source being away from the centreline of the detector, images from ^{239}Pu and ^{235}U, images of common laboratory sources and also simulations to show the improvement on the final image resolution achievable if pulse shape analysis was applied to the experimental data.

The systems ability to detect source across its 2 pi field of view will be tested. The effect on the final images produced will also be presented, along with the imaging performance of the detector system (in terms of angular resolution and energy resolution) will also be presented.

1.3 Current technologies

Compton cameras are not currently deployed within the decommissioning or homeland security areas, due to their experimental nature. Coded aperture and pin hole collimated systems are used to provide images, with the systems being commercially available for example the RadScan 800 is manufactured and marketed by BIL, while CARTOGAM is produced and sold by Canberra. Both of these systems are in use with a number of agenices within the UK.

A brief introduction of the current gamma ray imaging devices currently in use will

be given in this sub section. Please check the references provided for further reading on the individual systems shown. Other systems are also available commercially and in development, some of these will be introduced later in this text.

1.3.1 RadScan 800 and CARTOGAM

The RadScan 800 has been at a number of UK nuclear licensed sites, such as Dounreay, Harwell, Aldermaston and Sellafield for a number of years. The system is a remotely controlled, highly collimated scanning gamma detector. The system consists of a sodium iodide detector mounted behind a tungsten collimator. The collimator can be altered to provide four different fields of view, 2, 3 or 4 degrees. The system is limited by the thickness of the collimator, as the gamma ray energy increases the chance of the gamma ray penetrating the collimator will increase, resulting in a loss of image resolution.

Radscan has been used to assay radioactive cells [6], test uranium hold up [7] and to scan environments [8] which are being decontaminated for hotspots which may be missed using more conventional hand held monitoring. This work shows that the system performs well for γ ray energies of up to 662keV for uranium and also ^{137}Cs sources. Its ability for higher energy sources is touched upon however no images are presented. The quoted energy resolution is the angle of opening for the fitted collimator, this may not be a true measure but no point source measurement results could be found in publications.

CARTOGAM is a coded aperture system [9] utilising a 2 to 4mm thick caesium iodide detector with a computer generated tungsten mask. The system is lightweight and can be held in position in one hand or can be mounted as required. The energy range is quoted as being 50keV to 2MeV with a 30 or 50 degree field of view. Images are produced with a 1 to 3 degree angular resolution depending upon the collimator used. By taking an image with a mask and then an anti mask hot spots can be identified more clearly removing some of the background. Coded apertures do still suffer from poor resolution when a high energy gamma ray source is imaged, as the gamma ray is more likely to penetrate the mask. The size of the system limits the amount of shielding that can be used, alongside the limited crystal size this has limited the systems use on some sites.

Both systems use scintillator detectors, the crystals used have limited energy resolutiion capabilities. This can lead to the misidentification of nuclides present and possibly missing any illicit material packed with genuine radioactive shipments. The limited field of view of both systems (and similar systems that are available) limits their use in some situations, if a room is to be passively monitored for the movement of a gamma ray source these detectors would not be a viable choice. For scannig across large areas or looking at fixed objects the systems can provide useful results, depending

upon the energy of the gamma rays present. They will perform better for lower energy gamma ray sources.

1.3.2 Use of Compton camera systems

Compton cameras have been used for gamma ray astronomy for a number of years, NASA's COMPTEL (imaging Compton telescope) [10] being one of the largest historical projects. COMPTEL was a space based system, mounted on the NASA gamma ray observatory, launched in 1991 and subsequently deorbited in 2001. The system consisted of two sodium iodide detectors, looking at the energy range of 1 to 30MeV. The system had a field of view of 1 steradian (around 38 degrees) providing images with a few degrees of angular resolution. An astronomy Compton telescope has been tested at Fukishima within the exclusion zone [11], the results from this indicate that Compton camera systems can be used within the same situations as those in which RadScan and CARTOGAM have been tested producing results that are as good.

Chapter 2

Principles of gamma ray detection

Gamma rays are emitted as an excited nucleus decays to a less excited state, the gamma-ray photon will have an energy equal to the energy difference between the two states (less a normally negligible correction due to the recoiling atom). Gamma-ray emission is characteristic of a nuclide as the energy of the nuclear states in each nucleus are specific to that nuclide. This provides a method of identifying the radioactive material that is present. Gamma-ray emission normally follows a fission, α or β decay as these can leave the daughter nuclei in excited states [12].

To understand how gamma-ray detectors function some fundamental knowledge about how gamma rays interact with materials is required. In addition, for this project, the operation of semiconductors as gamma-ray detectors and the method used to connect the detector to a signal chain are an important part of the knowledge base required. The three dominant interaction processes that occur between 1keV to 10MeV are photoelectric absorption (PA), Compton scattering (CS) and pair production (PP).

2.1 Gamma ray production

The radioactive decay of a nucleus can take the form of particle emission (alpha, beta, neutron, proton and electron), fission resulting in two nuclei being produced along with additional particles and via the release of energy by the creation of gamma rays [12]. Nuclear decays release energy in the form of gamma rays and most nuclear decays and reactions will leave the resulting nucleus in an excited state with excess energy. The excited nucleus will then rapidly decay back to its ground state by the release of one or more gamma rays and particles. Gamma rays are photons of electromagnetic radiation typically with an energy range of 0.1 to 10MeV.

Each excited state of a nucleus has an energy associated with it and therefore will release a specific energy of gamma ray during the decays to another state. Each nuclear excited state has a specific angular momentum associated with it [12].

2.2 Interaction of radiation with matter

The cross section of a particular interaction occurring within a material depends upon the atomic number, Z, and the incident gamma ray energy, E_γ. This is illustrated in Figure 2.1. This plot shows lines where the probability of the dominant interactions within an energy band are equal. T is the probability of a photoelectric effect, σ is the probability of a Compton scatter and κ is the probability of a pair production.

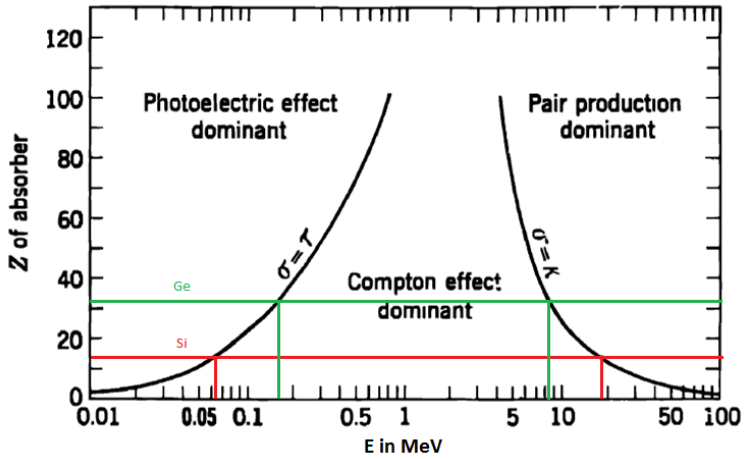

Figure 2.1: Relative importance of the three major interactions of gamma rays with matter. The lines indicate values of Z and E_γ for which the neighbouring effects are just equal. Diagram reproduced from [13].T is the probability of a photoelectric effect, σ is the probability of a Compton scatter and κ is the probability of a pair production. The green and red lines indicate the detector materials used in this project, germanium and silicon respectively.

2.2.1 Photoelectric absorption

Photoelectric absorption occurs when an incident gamma ray interacts with a bound atomic electron, transferring all of its energy to the electron as illustrated in Figure 2.2(a). This is the dominant process for low energy gamma rays incident on materials with a high Z as seen from Figure 2.1. The electron travels away from the atom with a kinetic energy E_e and is called a photoelectron, the kinetic energy is calculated via Equation 2.1 where E_b is the binding energy of the electron (energy required to remove the electron from the atom) and E_γ is the incident gamma ray energy.

$$E_e = E_\gamma - E_b \tag{2.1}$$

The photoelectron is most likely to be ejected from the most tightly bound electron shell of the atom, the K-shell. Following the photoelectron escaping from the atom, the atom is left in an ionised state. Orbital electrons from higher states will rearrange themselves to fill the vacancy resulting in characteristic X-rays being emitted.

The probability of photoelectric absorption occurring, τ, depends upon the atomic number of the material and the energy of the incident gamma ray. To approximate the probability Equation 2.2 can be used.

$$\tau \propto \frac{Z^n}{E_\gamma^{3.5}} \tag{2.2}$$

The variable n varies between 4 and 5 depending upon the energy of the incident gamma ray.

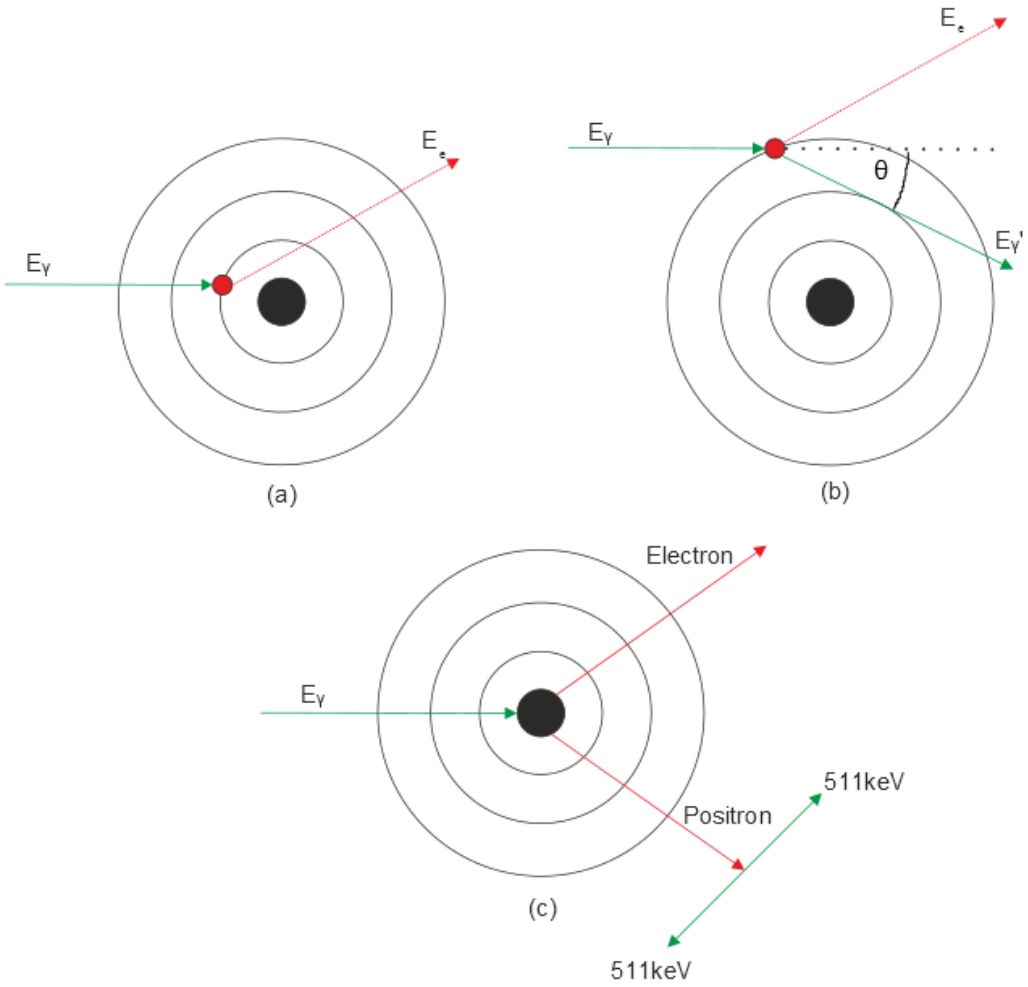

Figure 2.2: Illustration of the main gamma-ray interaction mechanisims that occur with matter. (a) shows photoelectric absorption, (b) is Compton scattering and (c) is pair production. Red lines indicate particle movement, green lines are γ rays.

2.2.2 Compton scattering

Compton scattering occurs when an incident gamma ray interacts with a weakly bound atomic electron, transferring a fraction of its energy and subsequently the gamma ray is deflected from its path by an angle θ, as depicted in Figure 2.2(b). The energy

transferred to the electron E_e depends upon the gamma-ray scattering angle, it retains an energy $E_{\gamma'}$. Assuming the electron is initially at rest and unbound, with a rest mass of $m_e c^2 = 511\text{keV}$, Equation 2.3 can be derived from the conservation of energy and momentum.

$$E_{\gamma'} = \frac{E_\gamma}{1 + \frac{E_\gamma}{m_e c^2}(1 - cos\theta)} \tag{2.3}$$

The scattering angle can vary up to 180 degrees where the maximum energy transfer occurs. This gives a range of energies for $E_{\gamma'}$ and E_e. In reality the recoil electron is not initially at rest, it is bound to an atom and moving within an atomic orbital. This results in a further spread of energies called Doppler broadening. This effect is more prominent when the absorbing material has a high Z and also for lower energy incident gamma rays [14].

To predict the angular distribution for scattered gamma rays a differential scattering cross section $\frac{d\sigma}{d\Omega}$ can be used, this is the Klein-Nishina distribution as described by Equation 2.4.

$$\frac{d\sigma}{d\Omega} = Z r_0^2 \left(\frac{1}{1 + \alpha(1 - cos\theta)}\right)^2 \left(\frac{1 + cos^2\theta}{2}\right) \left(1 + \frac{\alpha^2(1 - cos\theta)^2}{(1 + cos^2\theta)[1 + \alpha(1 - cos\theta)]}\right) \tag{2.4}$$

where

$$\alpha = \frac{E_\gamma}{m_e c^2} \tag{2.5}$$

Figure 2.3 represents this graphically as a polar plot of the number of gamma rays scattered at an angle θ for different gamma-ray energies. It can be seen that higher gamma-ray energies are preferentially scattered in a forward direction, while lower energy gamma-rays are scattered in a more symmetrical distribution about the 90 degree axis.

The probability of a Compton scatter increases linearly as the Z of the scattering material increases due to the number of target electrons increasing linearly with Z. Compton scattering is the dominant process within the energy range of 0.2 to 6 MeV in germanium as shown in Figure 2.1, this range is wider for silicon, going from 0.06 to 19 MeV.

2.2.3 Pair production

Pair production occurs when an incident gamma ray interacts within the Coulomb field of a nucleus and disappears. The gamma ray is replaced by an electron-positron pair as shown in Figure 2.2(c). By the conservation of energy this process can only occur if the incident gamma ray has energy sufficient to create an electron-positron pair. Assuming that the pair is created at rest, the minimum energy possible is twice the electron mass,

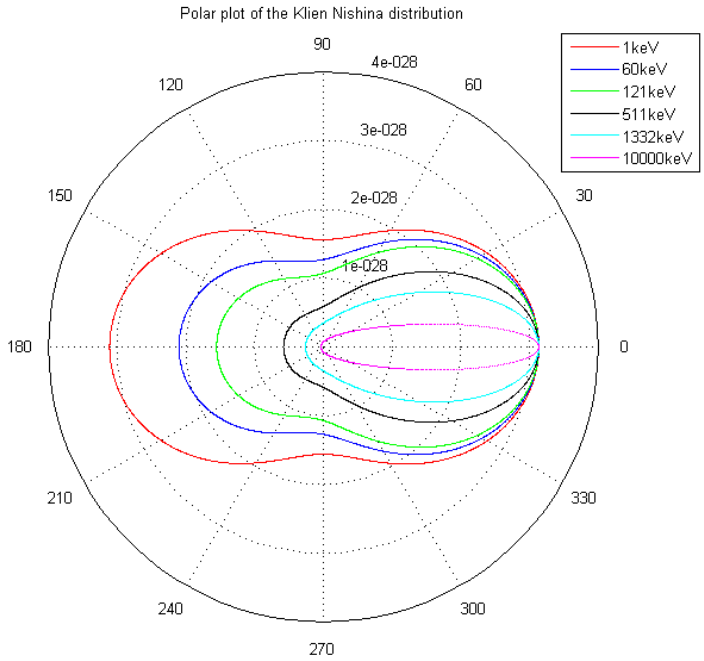

Figure 2.3: The Klein Nishina distribution shows that for higher energy gamma rays it is more probable that they will Compton scatter in a forward direction. For energies around 10MeV the gamma rays are preferentially scattered in a forward direction where as for energies less than 100keV the distribution becomes more symmetrical about the 90 degree axis.

1.022MeV. Any additional energy from the gamma ray is shared between the pair as kinetic energy. The positron will travel through the material, thermalising as it goes until it annihilates with an electron within the material producing two 511keV gamma rays at 180 degrees from each other assuming the electron and positron are both at rest. A small variation in energies and angles is seen in actuality due to the momentum of both particles. These two gamma rays can be absorbed within the material although one or both may escape, resulting in escape peaks being visible in gamma-ray spectra [15].

2.2.4 Linear attenuation coefficient

A material's ability to absorb an incident gamma ray's energy completely is defined by its linear attenuation coefficient, μ. Its measured for a given gamma-ray energy and is a property of the material. The relationship for a fixed energy is given in Equation 2.6.

$$\mu_{total} = \mu_{PA} + \mu_{CS} + \mu_{PP} \tag{2.6}$$

where the attenuation for each interaction is taken individually, μ_{PA} is the attenuation due to photoelectric absorption, μ_{CS} is the attenuation due to Compton scattering and μ_{PP} is that due to pair production.

If a monoenergetic beam of gamma rays is incident on a material, the intensity I measured after a thickness of material z is given by Equation 2.7, where I_0 is the initial beam intensity.

$$I = I_0 e^{\mu_{total} z} \tag{2.7}$$

2.3 Interactions of charged particles with matter

Electrons can be emitted from atoms during the processes described previously. Within a semiconductor detector electrons are one of the charge carriers of interest. Understanding how these particles interact with material is therefore a vital part of understanding the workings of a semiconductor gamma-ray detector.

Unlike gamma rays which lose energy via discrete processes, electrons lose energy continuously as they travel through a material via collisions with other electrons and by emitting radiation. Energy losses due to collisions $\left(\frac{dE}{dx}\right)_c$ and losses due to the emission of radiation $\left(\frac{dE}{dx}\right)_r$ combine to give the linear stopping power $\left(\frac{dE}{dx}\right)_{total}$ for a material for electrons and as given in Equation 2.8.

$$\left(\frac{dE}{dx}\right)_{total} = \left(\frac{dE}{dx}\right)_c + \left(\frac{dE}{dx}\right)_r \tag{2.8}$$

2.3.1 Collisional energy loss

Electrons travel through a material, Coulomb scattering via elastic and inelastic methods from bound atomic electrons. The energy loss for an electron with velocity v incident on a material with atomic number Z and density N can be described by the collisional Bethe-Bloch formula,

$$-\left(\frac{dE}{dx}\right)_c = \frac{2\pi e^4 N Z}{m_0 v^2}\left(\ln\left[\frac{m_0 v^2 E}{2I^2 k}\right]\right) \tag{2.9}$$

where

$$k = 1 - \beta^2 \tag{2.10}$$

$$\beta = \frac{v}{c} \tag{2.11}$$

and I represents the average excitation and ionisation that takes place with each collision.

2.3.2 Radiative energy loss

Electrons entering the Coulomb field of a nucleus will be decelerated and deflected from their original path, emitting Bremsstrahlung radiation as a result. A continuous

spectrum of photons is seen as the energy is transferred. These photons can be absorbed within the material or if they have enough energy they can escape. The energy loss of electrons due to this radiation emission is described by the radiative Bethe-Bloch formula, Equation 2.12 (this equation uses the same notation as Equation 2.9).

$$-\left(\frac{dE}{dx}\right)_r = \frac{NEZ(Z+1)e^4}{137m_0^2c^4}\left(4\ln\left[\frac{2E}{m_0c^2}\right] - \frac{4}{3}\right) \tag{2.12}$$

The energy loss caused by radiative means is less than that from collisions for an electron kinetic energy below 1MeV. The ratio of the energy losses seen from both processes can be seen in Equation 2.13.

$$\frac{\left(\frac{dE}{dx}\right)_r}{\left(\frac{dE}{dx}\right)_c} \approx \frac{EZ}{700} \tag{2.13}$$

Radiative losses are only significant if the material has a high Z value or if the electron energy is in the MeV or above range. This thesis will concentrate on materials with Z of 14 (silicon) and 32 (germanium) along with gamma-ray energies of 1.332MeV and below. Radiative energy loss for the electrons will therefore be minimal.

2.4 Solid state gamma-ray detectors

Gamma rays interact with the material of a detector via the processes described previously. Energy is transferred to the electrons within the material from the incident gamma rays. The electrons subsequently transfer their energy into the bulk of the material via exciting other electrons, ionising atoms or emitting Bremsstrahlung radiation until they come to rest. The resulting net charge deposition can be detected as an electrical signal, this is processed through electronics to produce the gamma-ray spectra of interest. Solid state gamma-ray detectors fall into two distinct categories, either scintillators where a light pulse is produced for each gamma-ray interaction or semiconductor diodes where electron-hole pairs are produced.

2.4.1 Semiconductors

Typically materials are separated into three categories, conductors, insulators or semiconductors. The separation depends upon the occupation of energy bands by the electrons within the material. A simplified view assumes that there are two bands, the valence and conduction bands, separated by a forbidden region which no electrons will occupy, the band gap. The valence band corresponds to outer shell electrons bound to specific lattice sites within the crystal, creating part of the covalent bonding forming the inter-atomic forces within the crystal. The conduction band contains electrons that are free to migrate through the material and which contribute to the material's electrical conductivity. The size of the band gap determines whether the material is a conductor,

insulator or semiconductor. The bands can be described by the relationship between the electron energy E and the effective electron momentum k as shown in Figure 2.4 where the grey shaded area is the band gap, this diagram is for germanium.

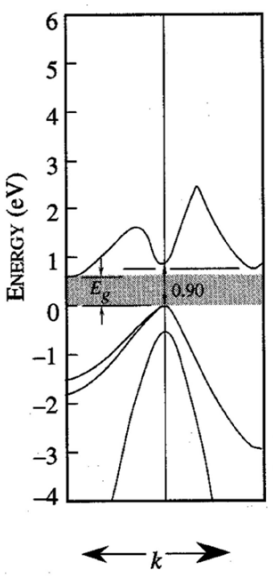

Figure 2.4: Band structure of germanium, shown in terms of the electron energy, E and the effective electron momentum, k. The shaded region corresponds to the band gap, the region of forbidden energies. The valence band and conduction band are therefore the bands below and above the shaded area respectively.

Within a conductor there is essentially no band gap so the electrons are free to move, and the material will conduct an electric charge freely. An insulator has a large band gap, typically 5eV or more, resulting in all of the electrons occupying the valence band. This leads to the material resisting an electrical current, until the current is so great that a break down occurs when electrons are promoted to the conduction band and can freely carry the electric current. A semiconductor at 0K is an insulator however, at temperatures above this there is a finite probability that electrons in the valence band can be promoted to the conduction band due to thermal excitations because of the smaller band gaps of these materials when compared to insulators (around 1eV). The difference between an insulator and semiconductor is presented visually in Figure 2.5. A comparison of properties between two semiconductors, intrinsic silicon and germanium can be found in Table 2.1.

Charge carrier production

If energy is deposited in an intrinsic semiconductor material, electrons are promoted to the conduction band and a corresponding hole is created in the valence band. Thermal excitation of the electrons within the material can also cause the creation of electron-hole pairs due to the small band gap. These thermal excitations are a cause of noise

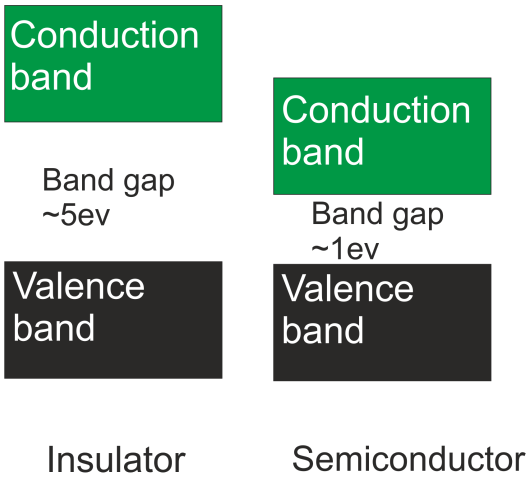

Figure 2.5: Illustration of the electron energy bands allowed within semiconductors and insulators. The band gap is a forbidden region in which no electrons can remain, an insulator has a band gap of 5eV or more compared to around 1eV for a semiconductor.

Table 2.1: Properties of intrinsic silicon and germanium, from [15]

	Si	Ge
Atomic number	14	32
Atomic weight	28.09	72.60
Band gap at 300K (eV)	1.115	0.665
Band gap at 0K (eV)	1.165	0.746
Electron mobility at 300K ($cm^2/V.s$)	1350	3900
Hole mobility at 300K ($cm^2/V.s$)	480	1900
Electron mobility at 77K ($cm^2/V.s$)	2.1×10^4	3.6×10^4
Hole mobility at 77K ($cm^2/V.s$)	1.1×10^4	4.2×10^4
Energy per electron hole pair at 77K (eV)	3.76	2.96

within a detector system, to reduce the magnitude of the noise semiconductors can be cooled cryogenically commonly using liquid nitrogen or mechanical cooling, this is especially true if a small band gap semiconductor is used, such as germanium. Semiconductors such as silicon, cadmium telluride (CdTe) and cadmium zinc telluride (CZT) can be used at room temperatures due to their comparatively large band gaps however cooling them will reduce any noise from thermal excitations.

The production of electron-hole pairs is a discrete quantised process and the number of pairs produced is proportional to the energy deposited in the material. For an incident gamma ray, of energy E_γ, the number of electron-hole pairs produced N is given by

$$N = \frac{E_\gamma}{E_{pair}} \tag{2.14}$$

where E_{pair} is the energy required to create an electron-hole pair. If a gamma ray of 1MeV deposits all of its energy within a semiconductor with an ionisation energy of 1eV, 100,000 electron-hole pairs would be produced. In germanium at 77K this figure would be 33,780 and for silicon at 77K 26,595.

Under the influence of an external electric potential, the initial electron-hole pairs produced will move through the material producing secondary electron-hole pairs. This charge cloud will be generated in a small space, sub-millimetre in germanium, and will drift within the material until the particles either recombine or are collected via an electrical contact.

Doping

A pure or intrinsic semiconductor would only have electrons within the conduction band due to thermal excitation if no ionising radiation was present. Each electron in the conduction band has been promoted from the valence band therefore, there must also be an equal number of holes within the valence band to electrons in the conduction band.

In practise intrinsic semiconductors are very difficult to manufacture. Impurities within materials will dominate the electrical properties even with very small concentrations. Impurities can occur due to manufacturing process and even the purification processes used but may also be added intentionally in small concentrations as a dopant. Adding a dopant tailors the properties of a semiconductor. These dopants can either be donors from group V (pentavalent) of the periodic table or acceptors from group III (trivalent) of the periodic table.

Taking silicon as an example, a commonly used donor dopant is phosphorous. Phosphorus atoms will occupy a substitutional site within the silicon's crystal lattice, taking the place of a silicon atom. There are five valence electrons surrounding the dopant atom, four of which form covalent bonds with the neighbouring silicon atoms. One

electron is left very lightly bonded to the impurity atom, and will therefore take very little energy to promote it to the conduction band. These electrons can also occupy a position within the normally forbidden band gap lying just below the conduction band, see Figure 2.6. This creates an n-type material which has a larger number of conduction electrons than the number of holes within the valence band. Electrons are the majority charge carrier in this case, with holes being the minority charge carrier.

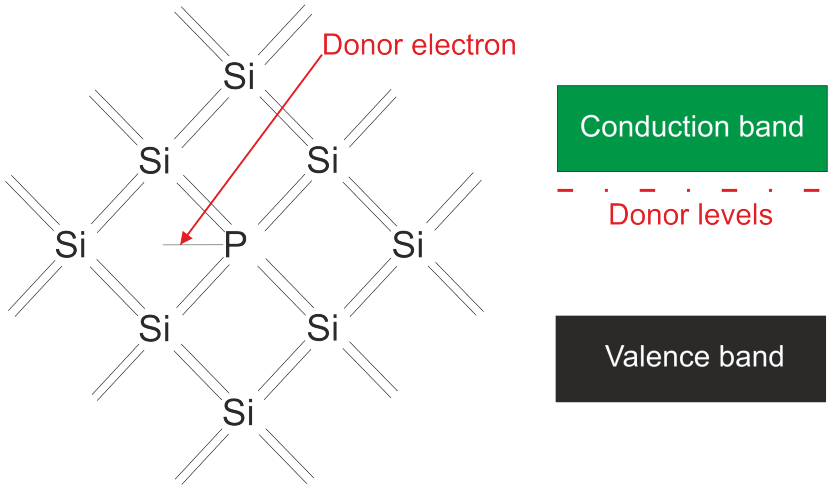

Figure 2.6: Doping with phosphorus creates an n-type semiconductor. A phosphorus atom substitutes for a silicon atom within the crystal in this example, creating a donor level due to its extra electron. This donor level exists within the band gap of the material close to the conduction band.

A commonly used acceptor dopant is boron. Adding this dopant creates a p-type material with an excess of holes in the valence band when compared to the number of electrons in the conduction band. The impurity atom will occupy a substitutional place within the silicon's crystal lattice but this time only has three valence electrons. This leaves one covalent bond unsaturated, see Figure 2.7, creating a vacancy within the valence band. An electron can be captured to fill this vacancy, participating in the covalent bond but is not as firmly bound as a typical valence electron. These acceptor impurities create electron sites within the band gap, lying just above the valence band.

p-n junction

Semiconductor radiation detectors rely upon the properties created near a junction between p and n type materials. Charge carriers are able to migrate across the junction if the materials are brought together in thermal equilibrium. The junction is normally formed in a single crystal by causing a change in the doping conditions from one side of the crystal to the other.

The density of electrons within the p-type material is much lower than in the n-type material. This results in a net diffusion of conduction electrons from the n-type to the p-type material where they quickly fill the holes within the valence band. This diffusion

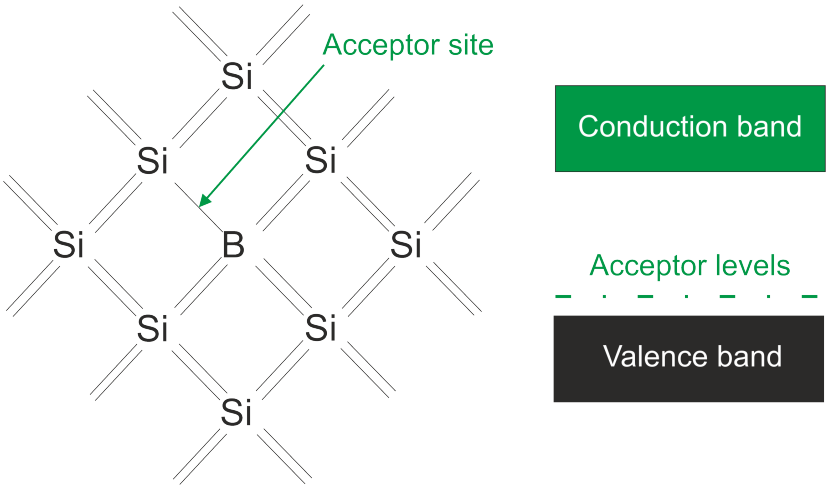

Figure 2.7: Doping with boron creates an p-type semiconductor. A boron atom substitutes for a silicon atom within the crystal in this example, creating an acceptor level due to the non covalent bond formed with one neighbouring silicon atom. This acceptor level exists within the band gap of the material close to the valence band.

leaves behind immobile positive charges in the form of ionized donor impurities. A similar and symmetric argument leads to the diffusion of holes across the junction from p-type to n-type. Each hole removed leaves behind an acceptor site that has picked up an extra electron and therefore represents a fixed and immobile negative charge. The combined effect produces a negative space charge on the p side and a positive space charge on the n side.

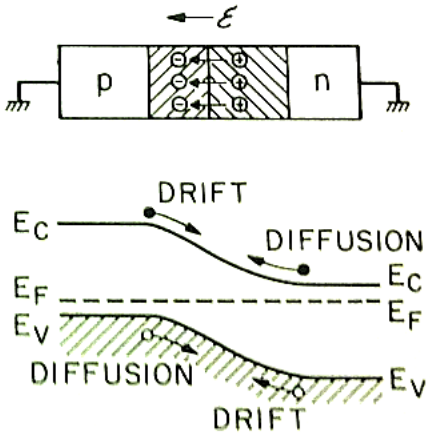

Figure 2.8: A depiction of a p-n junction, indicating the direction of electron diffusion, from n-type to p-type and also the drift of the holes. The depletion region formed is shown by the shaded area. Figure reproduced from [16].

The accumulated space charge creates an electric field which reduces the probability of further diffusion. The region over which the charge imbalance exists is called the depletion region and extends into both sides of the junction. By treating the boundary

as an abrupt junction and using the appropriate boundary conditions the one dimensional Poisson equation for the built in potential V_{bi} can be solved for a planar detector, this solution is given in [16] and shown here as Equation 2.15. The thickness of the depletion region x tends to be very small and dependent upon the concentration of donor N_D and acceptor N_A impurities.

$$\frac{d^2V_{bi}}{dx^2} = -\frac{\rho(x)}{\epsilon} \tag{2.15}$$

where ϵ is the dielectric constant of the material and $\rho(x)$ is the charge density. If V_{bi} is increased the depletion region width will also be increased. The total depletion region width is given by Equation 2.16.

$$d = \sqrt{\frac{2\epsilon}{q}\left(\frac{N_A + N_D}{N_A N_D}\right)V_{bi}} \tag{2.16}$$

The depletion region is essential to the operation of semiconductor radiation detectors made from p-n junctions. To maximise the sensitive region of the detector the depletion region must be made as large as possible. By applying a bias voltage V, across the depletion region the depleted area is made larger by increasing the electric field within the material. To ensure the proportional response of the detector is maintained it is essential that charge carriers produced from gamma-ray interactions do not recombine. The application of a reverse bias across the junction meets these requirements. Reverse bias is used as the current across the material tends to a saturation level, I_o, in comparison a forward bias causes the current to increase exponentially becoming strongly conducting. This is illustrated in Figure 2.9. To avoid dielectric breakdown the maximum reverse bias voltage that can be applied to a detector is limited by the thickness and material. The thickness of the depletion region for a planar detector can be calculated using Equation 2.16.

The reverse bias is applied until the full volume of the detector crystal is depleted, this is reached at the depletion voltage V_D. Operating voltages are higher than V_D, this ensures that the charge carrier drift velocity is saturated, optimising the charge collection performance.

Electron and hole mobility

The electron hole pairs will diffuse away from their creation sites with time due to the small electric field from the built in p-n junction potential. They may eventually recombine. By applying a potential difference an additional electric field ε will be formed across the material, forcing the charge carriers to migrate in opposite directions parallel to the electric field. The drift velocities of holes, v_h and electrons, v_e are affected by their respective mobility through the materials, μ_h and μ_e for electric fields $<10^3$ $\mathrm{Vcm^{-1}}$.

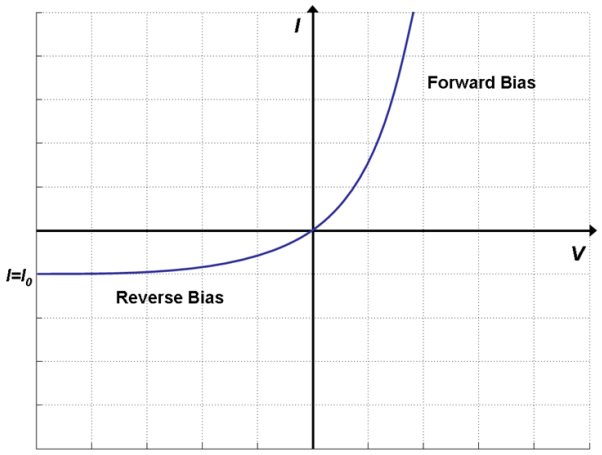

Figure 2.9: Current flow across a p-n junction when a bias voltage is applied.

$$v_h = \mu_h \varepsilon \tag{2.17}$$

$$v_e = \mu_e \varepsilon \tag{2.18}$$

As the applied electric field is increased, the drift velocity increases proportionally. Drift velocities reach a saturation level once an electric field of around $10^4 V cm^{-1}$ is applied. Within this saturation region drift velocities are independent of the applied electric field. Semiconductor detectors are typically operated within this region.

Crystalline structure of germanium and silicon

Germanium and silicon crystallize into a structure which is a diamond cubic, this is based on the face centred cubic bravais lattice [17] as shown in Figure 2.10.

A number of the materials properties including the electron and hole mobility will vary along different crystal planes. Miller indices are a standard way of defining the plane within a crystal, examples of the Miller indices for germanium and silicon can be seen in Figure 2.11.

The crystals chosen for semiconductors will be cut with their depth profile along the plane where the electron mobility is the highest this is found to be the <100>plane [18]. The electron drift velocity in germanium along the <100>, <111>and <110>planes at 80K is shown in Figure 2.12.

Detector segmentation

This work will concentrate on semiconductor crystals with a planar geometry. In their simplest form planar semiconductor detectors are made by sandwiching a piece of semiconductor material between two contacts, one of n-type and one of p-type. The contacts

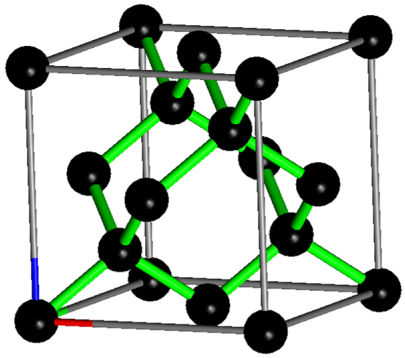

Figure 2.10: A schematic of the diamond cubic crystal lattice, based on the face centered cubic (fcc) bravais lattice. This is the crystal formed by both silicon and germanium.

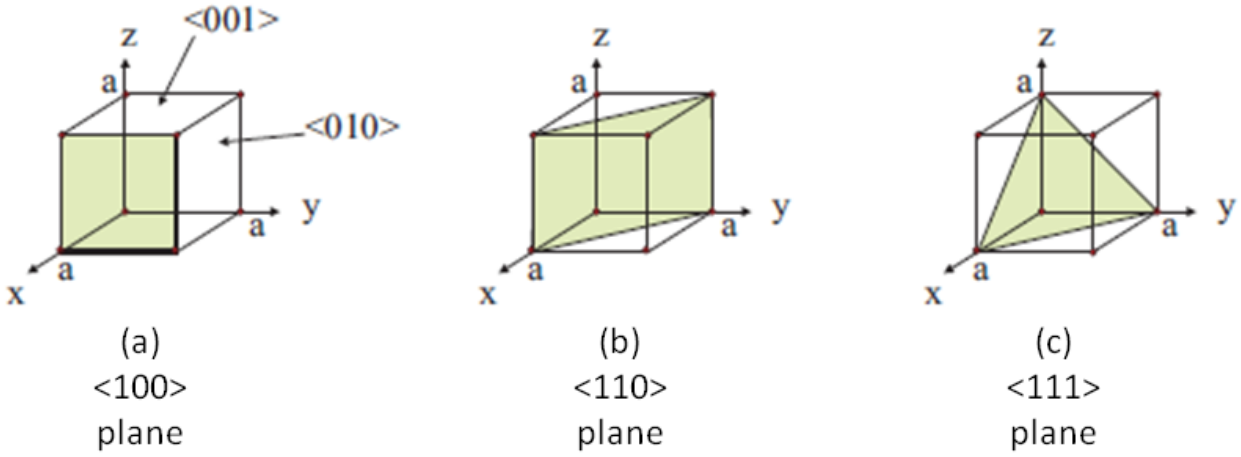

Figure 2.11: A schematic showing the lattice planes of an fcc crystal structure <100>, <110>and <111>marked (a),(b) and (c) respectively, in terms of the Miller indices.

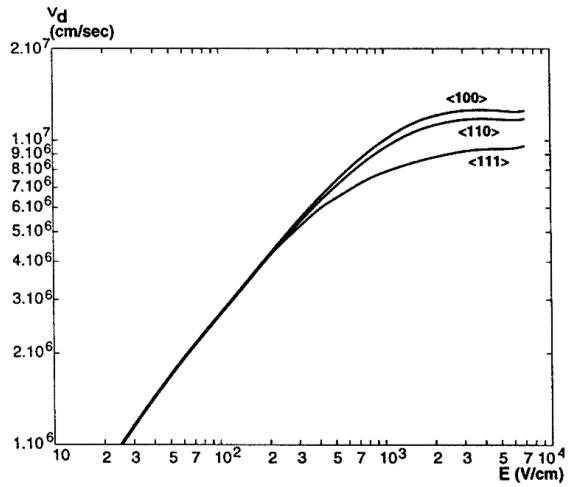

Figure 2.12: Experimental electron drift velocities in germanium along the <111>and <100>planes. The <110>direction is also shown, this has been simulated. Diagram reproduced from [18]

themselves can be manufactured by implanting a material such as boron to create a p-type contact and drifting or implanting materials such as lithium into the opposite side to create an n-type contact. The silicon detector used in this work is thought to have been manufactured using boron implantation and lithium drifting to create the contacts while the germanium detector contact were made using implantation for both side. As detector manufacturers use proprietary methods the exact details are not known.

Non-segmented detectors are used for a variety of applications however, they rarely provide information about where an interaction occurred. To do this detector manufacturers have created different methods of pixellating the active area of a detector. One method is to use stripped contacts, with a very small interstrip gap, running perpendicular to one another on the different sides of the detector. In this way an interaction can be located by identifying the strip on either side which contains a pulse. This type of detector is known as a double sided strip detector (DSSD).

Another method used is to physically pixellate the detector, creating small detectors which are linked to the electronics as an array. This method is can be more expensive than using strips depending upon the number of pixels created due the the cost of creating and instrumenting a potential large number of contacts.

2.4.2 Scintillation detectors

Scintillation detectors are one of the oldest methods used to detect ionising radiation. In general they are relatively inexpensive, efficient, reliable and robust. Common applications would be in classic gamma camera systems as used by homeland security agencies worldwide and also for general monitoring systems. An overview of their op-

eration will be provided here for a more indepth discussion please refer to [15] and a schematic diagram of the operation can be found in Figure 2.13.

Scintillation detectors rely on the collection of scintillation light produced following the interaction of ionising radiation with the detector material. The interactions with the detector crystal release electrons, the excited electrons then lose energy as they fall into lower energy states, releasing photons of light. The photons produced are the information carriers in this case. Typically it takes around 100eV to produce 1 photon, so for a 1MeV gamma ray depositing all of its energy, 10,000 photons would be produced. This light is collected in a photomultiplier tube (PMT). This device converts the photons into electrons, the number of electrons is subsequently amplified by a series of electrodes. Photodiodes can be used instead of a PMT however, they are not commonly used. The electrical signals produced provide spectroscopic information on the incident gamma rays. An ideal material for a scintillation detector would have the following characteristics [15]:-

- Efficient conversion of deposited energy into scintillation light.
- Linear conversion of deposited energy into light yield.
- The material should be transparent to its own light emission wavelength.
- Short decay time for the generation of fast electrical pulses.
- Manufacturable in large sizes appropriate for practical radiation detection applications.
- Refraction index of 1.5 for efficient coupling of the scintillation light to a PMT.

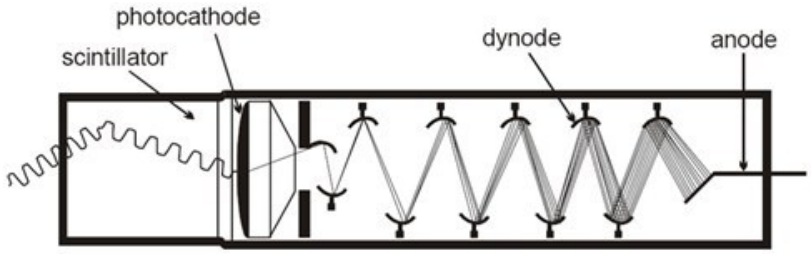

Figure 2.13: A schematic diagram showing the function of a scintillator and PMT when incident radiation interacts within the detector material. Electrons are produced by the gamma ray interaction, the subsequent de-excitation of these electrons produces light. The light photons are collected by the photocathode, and the subsequently produced electrons are accelerated through the PMT, being amplified as they pass through the dynodes to produce an output signal on the anode.

Inorganic crystals, plastics and organic compounds can be used as scintillators. The choice of a detector material will lead to a compromise between these characteristics,

physical properties such as the size of crystal which can be manufactured, difficulty of manufacture and the costs involved. Thalium doped sodium iodide (NaI(Tl)) is an inorganic crystal which has been used widely for the detection of gamma rays within the defence, medical and academic communities due to the high Z of iodine (53), short decay time and an excellent light yield which also matches in wavelength to readily available PMT's.

The typical energy resolution seen from a NaI(Tl) detector is around 12% at 121keV, if multiple isotopes with an energy within 12% of 121keV were present this would not be sufficient to separate the different isotopes. Examples of other commonly used inorganic scintillators are caesium iodide (CsI) and bismuth germinate (BGO). In addition plastic scintillators are commonly used for industrial applications due to their low cost, ease of maintenance and ability to manufactured to large sizes, these include stilbene, anthracene and naphthalene. Each have disadvantages and advantages for various different situations, these are discussed in [15].

2.4.3 Energy resolution

Taking a mono energetic source of gamma-rays the energy resolution of the detection system can be defined as the full width at half maximum (FWHM) of the photopeak produced in the gamma-ray energy distribution, assuming that the distribution is Gaussian in shape, and that there is negligible background (or it has been subtracted). If the peak is assumed to be Gaussian in shape the FWHM can be related to the standard deviation σ, as FWHM i= 2.35σ. The energy resolution will be dependant upon the energy of the photopeak.

A detector with better energy resolution will have a lower value. The resolution can also be presented as a percentage of the total photopeak energy, this is normally only the case for scintillators. Gamma-ray energies separated by more than plus or minus the FWHM should be resolvable as separate peaks. Fluctuations within the system may cause increased energy resolution, drifting of electronic components and variation in temperature are two examples. Statistical noise caused by the discrete creation of charge carriers will also contribute to the overall energy resolution measured.

The creation of charge carriers which generate the charge, Q, within a detector is a discrete statistical process. For a mono-energetic gamma-ray source depositing energy within a detector the number of charge carriers created will fluctuate between each deposit. Assuming that the charge carrier formation follows Poisson, statistics an estimate of the fluctuation can be made. If the total number of charge carriers generated is N, a standard deviation of $\sqrt{N}$ is expected. The response of a detector is approximately linear so the average pulse height $H_0 = KN$ with K being a proportionality constant. The standard deviation σ for the peak's pulse height will be given by $\sigma = K\sqrt{N}$ and the $FWHM = 2.35K\sqrt{N}$. An ideal detector would therefore

produce as many charge carriers as possible for each gamma ray incident upon it to reduce the limiting resolution, semiconductor detectors are very popular due to their high production of charge carriers.

A limiting resolution R due to the statistical fluctuations of the charge carrier creation can be calculated by Equation 2.19. As the number of charge carriers N increases, the resolution R will decrease.

$$R_{\text{PoissonLimit}} \equiv \frac{FWHM}{H_0} = \frac{2.35K\sqrt{N}}{KN} = \frac{2.35}{\sqrt{N}} \tag{2.19}$$

The formula above relies on the production of charge carriers being independent from each other. This is not the case however and a factor is used to quantify the differences seen between the Poisson statistical model and reality, the Fano factor F.

$$F \equiv \frac{\text{observed variance in N}}{\text{Poisson predicted variance}} \tag{2.20}$$

This modifies Equation 2.19 to Equation 2.21.

$$R_{\text{FanoLimit}} = \frac{2.35K\sqrt{N}\sqrt{F}}{KN} = 2.35\sqrt{\frac{F}{N}} \tag{2.21}$$

Fano factors of less than one are observed for semiconductor detectors, with germanium having a value of around 0.13 at a temperature of 77K [19].

In addition to this statistical fluctuation there are other factors which combine to affect the energy resolution of a detector. These include the charge collection efficiency and electronic noise contributions. The three factors can be added in quadrature to give a theoretical FWHM for a detector system, Equation 2.22.

$$FWHM = \sqrt{W_D^2 + W_x^2 + W_E^2} = W_T \tag{2.22}$$

where the W terms provide the peak widths observed if no other factors were involved. W_D refers to the statistical uncertainty and Fano factor, W_X is due to incomplete charge collection and W_E results from electronic noise contributions from all system components. In general, for an undamaged fully biased detector system charge collection should not be a major factor assuming the detector is fully depleted and operated with a sufficiently high bias voltage to saturate the charge carrier drift velocities. Each factor varies with respect to the incident gamma-ray energy, at low energies the contribution of electronic noise and collection efficiency dominate the peak width while at higher energies the carrier statistics term becomes more significant. This is illustrated in Figure 2.14 for a germanium detector.

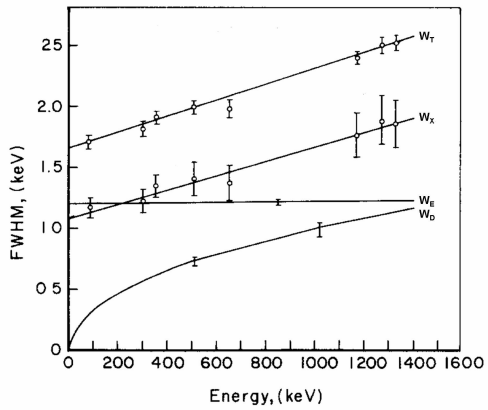

Figure 2.14: Variation of the FWHM of a full energy peak within a germanium detector with incident gamma-ray energy. Each factor discussed is represented individually and the combination W_T of these factors is shown. Figure reproduced from [15]

2.5 Signal generation

A single gamma ray interacting within a detector provides an output which is a burst of charge Q. The charge is proportional to the energy deposited and is measured as a transient current $I(t)$ where Q is the integral of the current pulse with respect to time. Exposure to a number of gamma rays will result in a series of pulses occurring at random times, with varying amplitudes and durations due to the random nature of gamma-ray emission.

2.5.1 Weighting potential

The motion of charge carriers through the material causes charge to be induced on the contacts. This induced charge causes a signal to be seen, this signal starts when the charge carriers are formed and the signal magnitude increases with time as the charge carriers are collected. Once the charge carriers are fully collected the pulse will be fully formed. The timing properties of the signal can provide information on the location of radiation interactions within the material. The Shockley-Ramo [20, 21] theorem provides a method to calculate the induced charge on an electrode due to the motion of charge carriers within a detector. This gives rise to the non-physical concepts of weighting potential and weighting field.

The instantaneous current induced on an electrode $i(t)$ can be calculated as a function of the charge of the carrier, q, the drift velocity v_d, the intensity of the electric field at the charge carriers position, E and the electric potential of the electrode, φ.

$$i(t) = q\frac{E(x,t)v_d(x,t)}{\varphi} \tag{2.23}$$

The weighting field and potential describe the coupling between an electrode and charge carrier and vary only with device geometry, this allows the instantaneous current to be computed by treating the problem electrostatically as a function of the charge carrier position, x. To do this we assume

1. The electrode collecting the charge carriers is at unit potential.
2. No space charge is present.
3. All other electrodes have zero potential.

These assumptions are not true for a real detector system however it has been shown in [22] that the induced charge on any electrode cannot depend upon the applied potentials or any stationary space charge. This allows the Shockley-Ramo theorem to be applied to semiconductor devices. A moving charge will induce a current, i given by

$$i = qv_d.E_0(x) \tag{2.24}$$

and a charge, Q given by

$$Q = -q\phi_0(x) \tag{2.25}$$

where ϕ_0 and E_0 are the weighting potential and field respectively. The charge, Q will vary as a function of time, t as the charge is collected, this is given by

$$Q(t) = -q\phi_0(x(t)) \tag{2.26}$$

The numerically calculated weighting field within a planar strip detector is shown in Figure 2.15, reproduced from [23].

2.5.2 Preamplifier

The charge pulses created within a semiconductor detector are very small and amplification is required before they can be processed through any electronics. Initially a field effect transistor (FET) stage is used, this is placed as close as possible to the detector providing an initial small amplification. Following this a preamplifier is used to further amplify the signal by a factor of A and shape the signal, the output signal is then passed to the detection chain. Charge sensitive preamplifiers as shown in Figure 2.16 are normally used for semiconductor detectors. This type of preamplifier produces an output voltage proportional to the total integrated charge in the input pulse. The duration of the input pulse must be short compared to the time constant R_fC_f of the circuit for a charge sensitive preamplifier. The rise time of the preamplifier is largely dependent upon the charge collection time within the detector as long as there is no

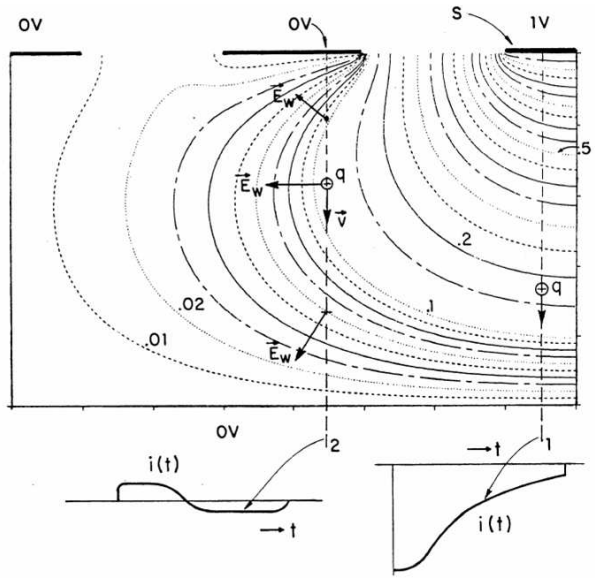

Figure 2.15: Schematic representation of the weighting field within a strip detector, reproduced from [23]. The current pulses induced by the movement of a charge carrier (q) are shown at the bottom of the diagram. As charge travels along line 1, it can be seen that the induced current decreases with distance from electrode 1. As charge moves along line 2 the induced current shape is bipolar due to the weighting field direction changing along the path.

resistance from any undepleted regions within the detector, or imperfect electrical contacts to the detector. The time constant of the capacitor and resistor chosen sets the preamplifier fall time, for this work the fall time is $\sim 150\mu$s.

Preamplifiers need to have good signal to noise properties and they are therefore placed as close to the detector as possible, minimising capacitive loading which can introduce noise into the system [15]. For a typical charge sensitive preamplifier the feedback resistance is 1GΩ (R_f) while the resistive capacitance is 1pF (C_f).

A sample preamplifier pulse can be seen in Figure 2.17, this is taken from a 20mm thick high purity germanium detector and represents an energy deposit of 662keV from a ^{137}Cs gamma-ray source.

2.5.3 Parametric pulse shape analysis

Improvements to the identification of interaction positions within a detector crystal can be made by using pulse shape analysis. This allows each event to be identified to a position within the raw segmentation created by strips or pixellation. There are two different methodologies used for pulse shape analysis, parametric and basis set comparison. Parametric pulse shape analysis within a DSSD will be discussed within this section. Basis set comparison utilises a full database of pulses from known interaction positions. The database pulses are then compared on an event by event basis where the best match in the database is used to provide the interaction location.

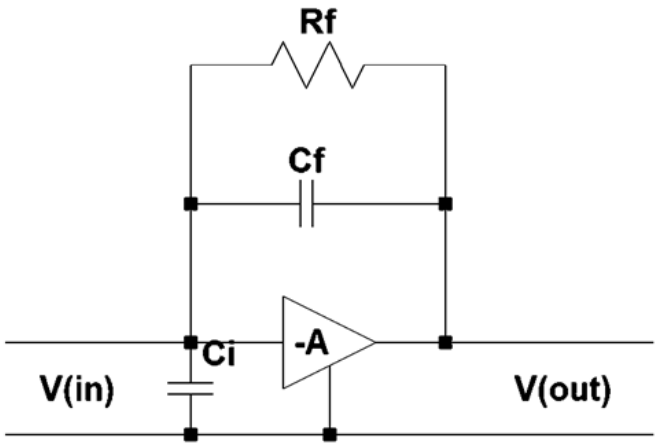

Figure 2.16: Circuit diagram of a typical charge sensitive preamplifier as used with semiconductor detectors.

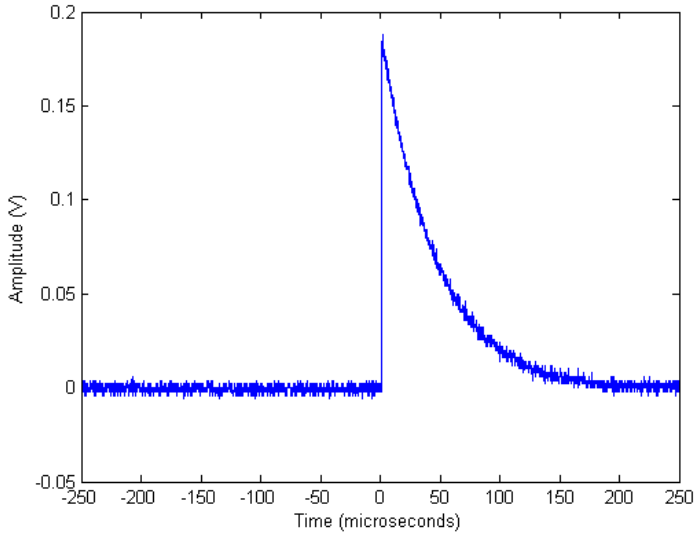

Figure 2.17: A typical preamplifier output pulse seen from a semiconductor detector.

An example of this can be found in [24].

Parametric pulse shape analysis techniques study the preamplifier waveform to extract three dimensional position information allowing a more accurate position to be associated with each interaction than that found using the raw segmentation. For parametric pulse shape analysis techniques two different methods are employed, one which provides information on the depth of interaction within a crystal between the two contacts, while the other is used to determine the interaction position relative to a segment boundary. In the case of a planar double sided strip detector this is the lateral position within a strip, thus providing positions in the X and Y planes within each strip.

The first method relies upon the Schokley-Ramo theorem discussed previously. Assuming the bias voltage supplied to a detector is sufficient enough to saturate the electron and hole drift velocities, the time taken to collect the charge carriers at their appropriate electrodes can only be a function of the distance they have travelled. Therefore the charge collection time is indicative of the interaction position, which is represented by the risetime of the charge pulse. The time taken to rise to 30% of the final amplitude is closely related to the collection of the charge carrier with the shortest drift distance to the collecting electrode (T30). while the time taken to reach 90% of the final amplitude is indicative of the full charge collection time (T90). These points are shown in Figure 2.18 which shows a pulse from a HPGe DSSD.

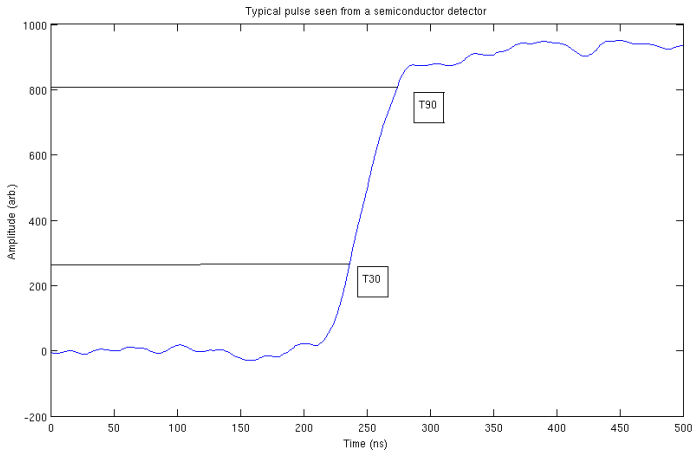

Figure 2.18: A typical pulse seen from a HPGe DSSD. T30 marks the point at which the majority of primary charge carriers for the contact have been collected, while T90 represents the time at which the majority of the secondary charge carriers have been collected.

The second component analyses the transient charges induced on neighbouring strips by the movement of charge carriers within a strip containing an interaction, these are called mirror or image charges. The electrostatic coupling between the moving charge carriers and the electrodes gives rise to the image charges, the signals have

no net charge. Within a planar detector, assuming the strips are of equal length and width the relative magnitude (and area) of the image charges seen on the strips either side of one containing an interaction will vary depending upon where within the width of the strip the interaction occurred. The closer an interaction occurs to a neighbouring strip the larger the image charge will be. This method is called image charge analysis (ICA).

By comparing the size of the image charges, IC on either side of the strip containing an interaction the lateral position within the strip can be found. This is done using Equation 2.27 where A is the asymmetry parameter of the image charges on either side of the strip containing an interaction. These methods are described in more detail in [25] for the HPGe detector used.

$$A = \frac{IC_L - IC_R}{IC_L + IC_R} \tag{2.27}$$

The typical pulses seen from a silicon strip detector and a germanium strip detector can be seen in Figure 2.19. The main pulses are shown with the pulses seen from neighbouring strips. The image charges cannot be seen in the silicon detector, Figure 2.19a as the energy deposit is very low. An image charge is typically at most 20% of the size of the inducing charge pulse, the noise level seen in this silicon detector compared to the charge pulse indicates that any image charges produced will be below the noise level and therefore lost. The germanium detector however shows image charges on both sides of the real pulse, showing that this can be used for ICA.

Within the plots there is an image charge to both sides of the real pulse for the germanium. The amplitudes are approximately the same though the one to the left appears to have a slightly larger area, indicating that the interaction took place to the lefthand side of the strip.

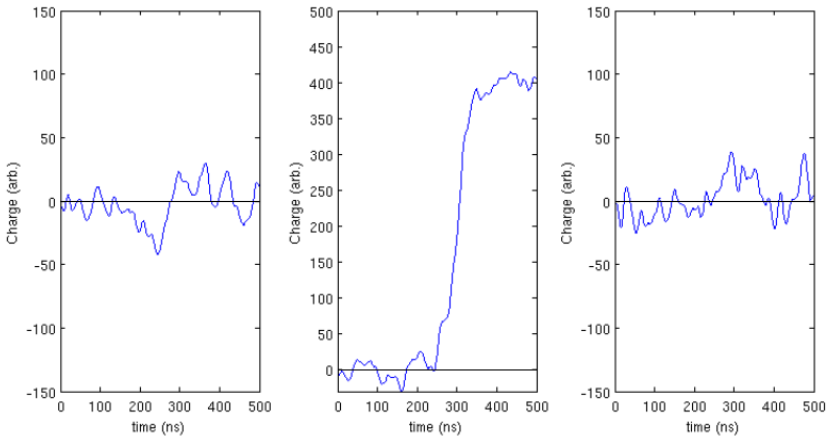

(a)

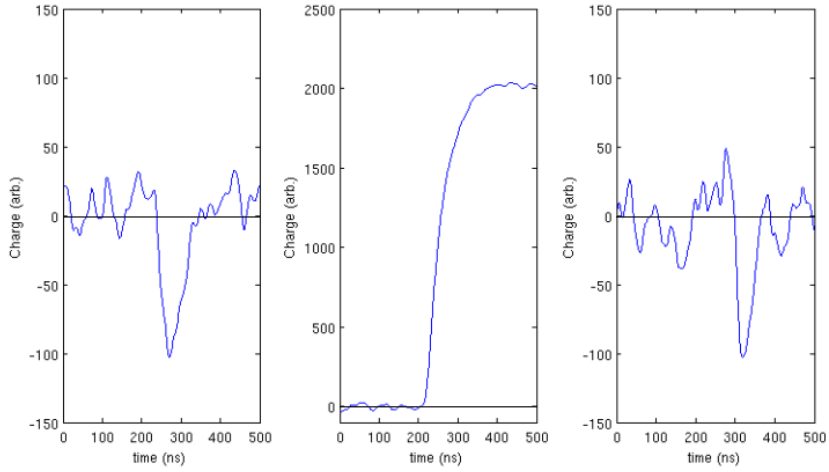

(b)

Figure 2.19: Typical pulses seen from a silicon (a) and a germanium (b) detector with the pulses seen in neighbouring strips included alongside. The image charges are lost in the silicon detector due to being below the noise level, however they are clearly visible in the germanium detector.

Chapter 3

Compton camera principles

There are a number of different detector devices utilised worldwide to identify and locate illicit radioactive material including handheld Geiger Muller tubes [26], fixed position portal monitors [27], portable spectroscopy devices [28] and vehicle mounted systems [29]. The references here are just a small selection of detectors available on the market today. Most of these devices do not provide any imaging capability but can identify if radioactive material is present and possibly identify the radioisotope present. If a detector lacks any position sensitivity or imaging capability an operator can move the detector around, typically using a grid type search pattern however, this method can lead to the operators being exposed to possibly large radiation doses and a non trivial exposure time depending upon the size of the area/object being examined. The detectors which fall into this class would include Geiger Muller tubes [26], handheld scintillation counter systems [30] and dose rate meters.

Mechanically collimated devices allow for a degree of positional information to be obtained allowing for less exposure to the operator. They are generally made from scintillator detectors due to their high detection efficiency. Mechanical collimators are typically made from high Z materials such as lead and tungsten and reduce the number of gamma rays which are incident upon a detector. The most commonly used collimation is a pin hole, where a single hole is made through the collimator allowing gamma rays to pass through to the detector if the collimated device is pointed directly at the radiation source.

Compton cameras remove the mechanical collimator and utilise electronic collimation. By removing the standard collimator more gamma rays will be incident upon the detector, increasing the quantity of data available for analysis. By identifying two or more interaction positions precisely Compton kinematics can be used to locate the source. This can be done using one detector with either pulse shape analysis or pixellisation, or using two or more position sensitive detectors. The use of this method also allows the detection of sources which are away from the centre of the detector's field of view, opening up the sensitive range to 2π around the front of the device.

3.1 Mechanical collimation

A brief introduction of the most commonly used mechanical collimation methods will be presented. There are two methods which are used, either pin hole or coded aperture. The usefulness of a collimator is determined by its effective thickness which is a combination of the material used and linear thickness. Both of these methods utilise high Z materials to prevent gamma rays penetrating through the collimator.

3.1.1 Pin hole collimated detectors

A pin hole collimator requires that the radiation source is directly in front of the detector. The collimators used are typically made from lead or tungsten so are relatively heavy. As the gamma-ray energy increases the collimator thickness has to be increased to prevent gamma-rays penetrating the collimator. If gamma-rays penetrate the collimator the position information starts to become degraded due to gamma-rays not in line with the pin hole being recorded. This type of detector will be rasta scanned across an area, and the count rates will be monitored as it moves, the point at which the highest count rate is measured provides the location of the source. Pin hole collimators have been used for a number of years in the medical imaging sector and have also found a place within the arsenal of homeland security agencies.

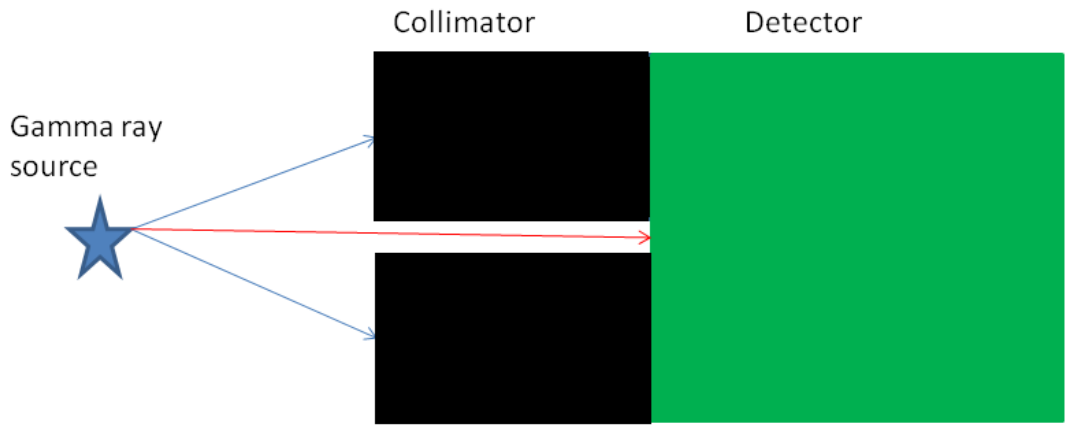

Figure 3.1: Schematic diagram of a pinhole collimator. The blue lines represent gamma rays that are absorbed by the collimator, only the red gamma ray will be enter the detector material.

Pin hole collimators are generally used with scintillator detectors due to their relatively high efficiency. A typical example is the RadScan 800 [31] using a non segmented NaI(Tl) scintillator mounted on a remotely controllable tripod utilising a tungsten collimator. The detector can be setup and left in position while it is controlled via a control cable allowing the minimum possible dose to the operator.

3.1.2 Coded aperture

Coded apertures systems are seen as the replacement for pin hole collimators in a variety of areas including homeland security. They offer a slightly wider field of view by replacing the pin hole with a coded mask. Coded apertures are grids or other patterns which are opaque to gamma rays. Analysing the shadow cast by the aperture on a position sensitive detector will create an image of the source. An anti mask is often used in addition to produce another image which can be used to remove background radiation from the measurements. The coded aperture mask is typically made of lead or tungsten as is the case with a pin hole collimator and the energy restrictions still apply, if the gamma ray energy is too high the collimators linear stopping power may not be enough to prevent the gamma ray penetrating the mask.

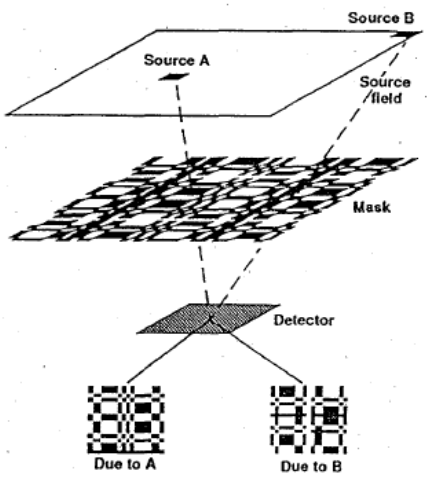

Figure 3.2: Coded aperture mask, showing the shadows created by two different sources A and B. Diagram reproduced from [32].

Coded aperture systems tend to be quite expensive in comparison to pin hole collimated systems due to their use of position sensitive detectors, complex computer algorithms to match the shadows and generate images and also the mask production itself. Their uptake has therefore been relatively slow. US agencies and AWE have employed the GRIS (Gamma Ray Imaging Spectrometry) developed at the Lawerence Livermore National Laboratory [32], Canberra also manufacture a comparable device using a NaI(Tl) scintillator called CARTOGAM. GRIS consists of a caesium iodide (CsI) detector with a position sensitive PMT [32] and is designed to be man portable. New systems are underdevelopment, one such device utilises a mechanically cooled HPGe detector [33] offering a better energy resolution and hence improved spectroscopic information.

3.2 Compton camera principles

Compton cameras have been tested since the 1970's [3, 2]. Developments in gamma-ray detectors and the associated acquisition electronics have lead to other applications of Compton cameras being researched including homeland security [5] and medical imaging [4]. Compton cameras use an active form of collimation usually referred to as electronic collimation. This removes the requirement for a collimator increasing the field of view of the detector and also the amount of data available for analysis as more gamma rays will be incident on the detector.

3.2.1 Detector setup

In general a Compton camera will consist of two detectors, a scattering detector (scatterer) and an absorber detector (absorber) though multi detector [34] and single detector systems [5] have been developed. A proportion of any incident gamma rays will Compton scatter within the scatterer. Subsequently a proportion of these scattered gamma-rays, will then undergo photoelectric absorption within the absorber as shown in Figure 3.3.

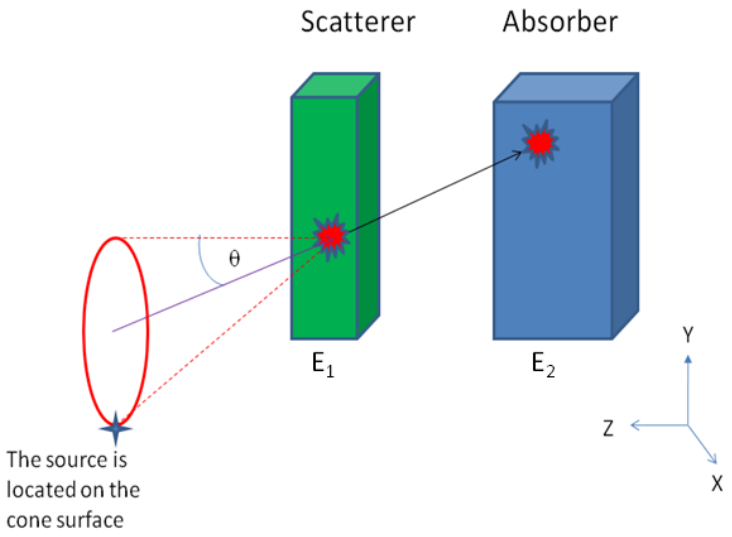

Figure 3.3: A two detector Compton camera. Gamma-rays Compton scatter in the scatterer and are subsequently absorbed via photoelectric absorption. The back projected cone has an opening angle θ calculated from the Compton scattering equation (Equation 2.3). The cone axis is positioned using the vector between the two interaction points.

In an ideal case where the gamma ray is fully absorbed, the energy deposited in the scatterer, E_1 plus the energy deposited in the absorber, E_2 gives the energy of the incident gamma ray, E_γ. The Compton scattering equation, Equation 2.3, can be rearranged to calculate the angle of scatter θ, as shown in Equation 3.1.

$$cos\theta = 1 - m_e c^2 \left(\frac{1}{E_1} - \frac{1}{E_1 + E_2} \right) \tag{3.1}$$

The position of the source will be somewhere at an angle θ from the interaction point in the scatterer. As the direction of the incident gamma ray is unknown the source could be anywhere on the surface of a cone with an opening angle θ.

Multiple events will generate a number of cones. To generate an image a slice perpendicular to the z-axis is taken, this is presented as an intensity pattern and the area of most overlap between the conic sections is the most probable location for the source as depicted in Figure 3.4. If the electron energy and direction of travel was known the cone would be reduced to a spot, with the size of the spot being determined from the uncertainties in measuring the energy deposited and the electron's direction of travel.

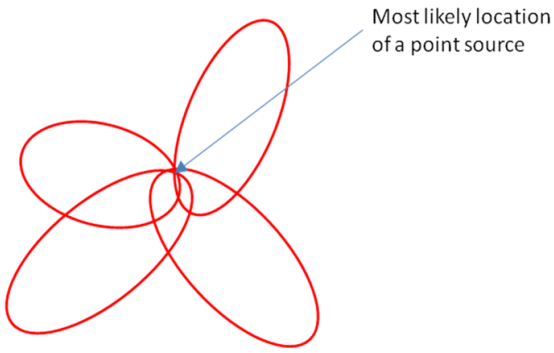

Figure 3.4: Multiple events will allow multiple cones to be generated. Taking a slice perpendicular to the z axis, the area of most overlap of the conics in this slice is the probable source location.

By taking the energies deposited in both detectors and adding them together, an addback spectra can be produced. This provides spectroscopic information, allowing the identification of the radioactive source.

This two detector setup is one of the most commonly proposed for medical and homeland security purposes however single crystal systems have also been tested such as that described here [5] where the interaction positions are calculated from pulse shape analysis techniques. Multiple detector setups for example the one found here, [34] which can produce images from three Compton scattered events in different detectors, alternative geometries are also available such as using rings of detectors as found in [35].

3.2.2 Detector qualities for a Compton camera

The scatterer in a two detector Compton camera should be made of a material which has a high Compton scattering cross section, compared to its photoelectric cross section.

This implies that a low Z material should be used. A good energy resolution is also required, reducing the uncertainty in the energy measurements made and hence the final images produced. Low noise characteristics are an essential quality for a scatterer, the amount of energy deposited by a Compton scatter will be small so a detector with a low noise level is required.

The absorber should be made from a high Z material with a very high efficiency to allow the full absorption of as many of the scattered gamma rays as possible. High efficiency will allow the number of Compton scattered events that are subsequently absorbed to be maximised, efficiency increases with the detector size as there is more area in which photons may interact. A large detector would also be favourable as it increases the range of scattering angles that gamma rays are detected at, a variety of scattering angles will be produced in the scatter detector so to maximise the number of these that are detected, an ideal Compton camera would have an absorber detector which covers as much of the solid angle from the scatter detector as possible.

In practise the detectors used will have to be a compromise between these factors, for example a very large absorber may not be possible due to the constraints of the system size through cost, crystal manufacturing techniques and physical size limitations. Pixellised or strip detectors will offer an interaction position sensitivity which is better than a bulk crystal, the choice of which segmentation to use will be dependant upon the number of pixels or voxels that are required. As the number of pixels increases the cost of the electronics required will also increase, while a strip detector could offer a lower cost for the same number of voxels.

3.2.3 Errors in Compton cameras

The images produced by a Compton camera are influenced by three main factors

1. Energy resolution of the detectors used Δ_{energy}.
2. Position resolution for the interactions within a detector $\Delta_{position}$.
3. Doppler broadening caused by the assumption used for the Compton scattering equation $\Delta_{Doppler}$.

The overall uncertainty in the reconstructed image Δ_{image} is given by

$$\Delta_{image} = \sqrt{(\Delta_{energy})^2 + (\Delta_{position})^2 + (\Delta_{Doppler})^2} \tag{3.2}$$

These factors are briefly described below.

Energy resolution

The energy deposited within the scatterer is used to calculate the opening angle of the cone, θ. Using a detector with poor energy resolution will result in θ having a greater

uncertainty and the resulting image will also have a greater uncertainty as a result. This is more important in the scatterer detector, as can be seen from Equation 3.1 as this energy is directly used to create the final image, within the absorber a poor energy resolution will result in a smaller error on the cone angle, an uncertainty on the energy of the incident gamma ray and will be visible within the addback spectra. Detectors with a good energy resolution are preferable as scatterers, if the system is to be used for identifying an unknown radiation source the absorber should also have a good energy resolution.

Position resolution

Position resolution of the interaction points within the detector is vital to positioning the cone axis. With the strip segmentation used for this work, the position of interaction is determined by checking which strip contains energy on each side of each detector. Utilising the raw segmentation the position can be determined within the strip pitch of the detector, so for a 5mm pitch strip detector the position resolution would $\pm$2.5mm. The depth of interaction would be assumed to be at the centre point of the detector. Pulse shape analysis can be used to improve this, allowing the position resolution to be reduced to below the strip pitch and also identifying the depth of interaction more accurately.

Doppler broadening

Doppler broadening has already been discussed briefly in Chapter 2. The use of Compton kinematics introduces an error assuming that the electron with which a gamma ray interacts via a Compton scatter is stationary and unbound. This in reality is not the case as the electron is bound to an atom and is moving in orbit around the nucleus so has a non zero momentum. This momentum will lead to an error on the measured energy deposition as the recoil electron will have a slight variance on its kinetic energy. Utilising a lower Z material for the scatterer reduces the effect of Doppler broadening as the electrons have potentially less momentum for a lower Z material. The momentum differences become negligible as the gamma ray energy increases above 100keV reducing the Doppler broadening effect.

3.3 Image reconstruction

Various methods are available for reconstructing images from Compton cameras. They can be broken down into two methodologies, analytical and iterative. The images produced within this thesis are created utilising an analytical unfiltered back projection algorithm so this will be discussed further and for completeness iterative methods will also be introduced. A general overview of image reconstruction can be found in [36, 37].

3.3.1 Analytical back projection

To produce an image analytical algorithms generate a back projection utilising Compton kinematics, in the case of this work the back projection is a cone described by the Equation 2.3. A two dimensional approach is taken within the analytical method utilised for this work. This method projects s series of two dimensional conics onto a plane in z, generating an image on an intensity map. This two dimensional method removes the need to generate a full cone, reducing the computational time required. The trigonometry used to build the cone is shown in Figure 3.5

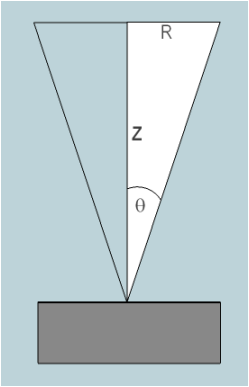

Figure 3.5: A simple case showing a gamma-ray Compton scattering from the front edge of the scatterer. Knowing the scattering angle θ the half radius R of the cone can be calculated for a given distance Z using trigonometry.

The conics are traced onto an intensity map. As the number increases the conics overlap, producing the images seen in Figure 3.6 shows this for 10 (a), 100 (b) and 1000 (c) cones.

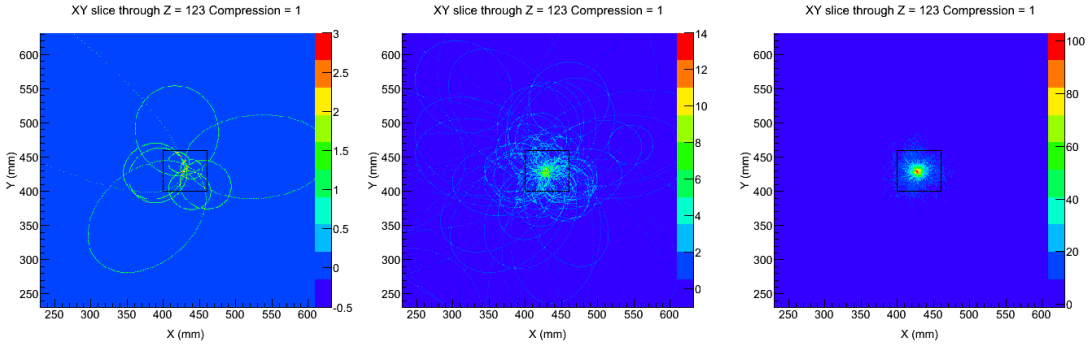

(a) (b) (c)

Figure 3.6: Examples of images created with 10 (a), 100 (b) and 1000 (c) conics. As the number of cones increases the source position is located more accurately, with the source positioned at the point of most overlap. These images are taken from the same GAMOS simulated data set. The black box on the image indicates the position of the absorber detector in relative space.

From Figure 3.6 it can be seen that as more cones are projected the image becomes

clearer with the area of maximum overlap indicating the source position, this is true until around 10,000 cones when additional cones do not make a significant difference. A measure of the image quality can be found by taking cuts through each axis at the maximum point in the intensity distribution, the FWHM of the image can then be found in both directions to quantify the image quality, examples can be seen in Figure 3.7. A quadratic background fit is performed and the peak is then fitted using a Lorentzian function based on this background, providing the FWHM measurement. The maximum point also provides an estimate of the x and y position of the source, a fit can be used to locate the source more accurately. The image quality can also be presented as an angular resolution, this removes the dependence upon source to detector distance.

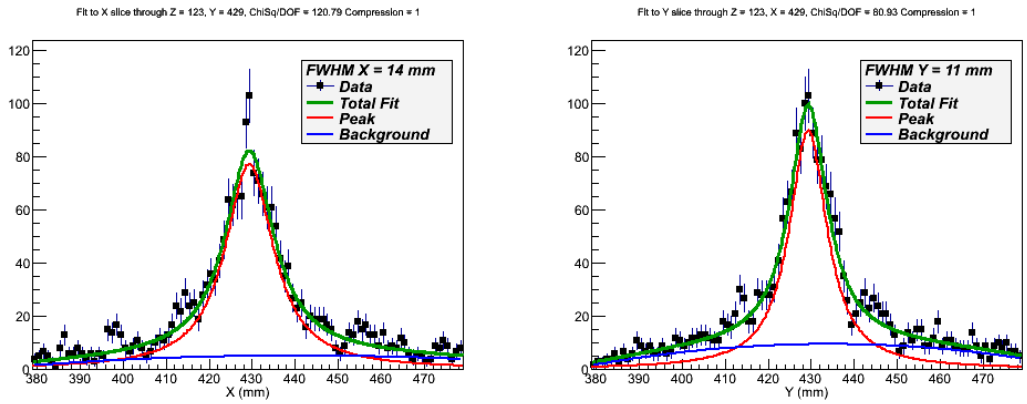

(a) (b)

Figure 3.7: Examples of the cuts taken through the X (a) and Y (b) axes taken from the GAMOS simulated data set. The Lorentzian fit is shown for each overlaid in green with the quadratic background in blue. This fit is used to provide the location of the source from the mean value and also the FWHM of the image, taken from the standard deviation of the fitted curve.

Imaging different z slices across a range will make the image come in and out of focus. The best FWHM value should be at the z slice in which the source is located. To find the distance to the source the FWHM of the reconstructed image is calculated for a number of different z slices and then plotted against the slice number. This plot will show a parabolic function as shown in Figure 3.8, where the minima gives the approximate location of the source. This method is not accurate however it does provide a guide, this will be investigated further in a later chapter.

Analytical methods in general utilise less computational power than iterative methods allowing the images to be produced faster and online imaging is also possible. Analytical images are of a poor quality when compared to iterative images, this is due to the simple back projection retaining a number of artifacts from conics which do not add to the image.

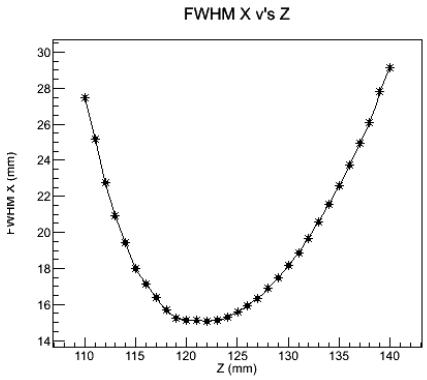

Figure 3.8: Plot of the FWHM found in X against the Z slice. The source position in Z is estimated by the minima of the curve.

Methods used

In this work the detectors used are both double sided strip detectors. The simplest events to reconstruct are made up of single voxel interactions within the scatterer and absorber so only events which have energy in one strip from each side of each detector are recorded. These events are called fold 1,1,1,1.

The interaction is assumed to have occurred at the centre of the rectangular voxel, in X, Y and Z. Within our detectors this leads to an error of ± half of the strip pitch in X and Y and a ± half of the thickness error in Z when raw segmentation is used. The Z slice is defined as zero at the back edge of the absorber and increases in units of millimetres as shown in Figure 3.9.

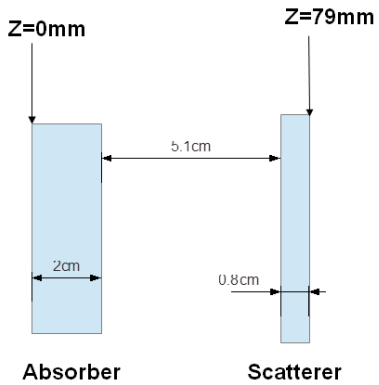

Figure 3.9: Schematic diagram showing the zero of Z for imaging purposes as being the back edge of the absorber crystal.

To generate an image the interaction point is taken to be the centre of a square voxel with a size equal to the pitch strip and a thickeness equal to that of the detector. This will introduce a slight error when applied to the circular silicon detector used for this project however the number of interactions that occur in the affected edge voxels means that error is negligible from this. The use of the centre point of a voxel produces

an error on the position of interaction of a half strip pitch (2.5mm in this case) and a half of the thickness (4mm and 10mm in the case of the two detectors used here). The images presented represent the 2π view of the detector.

A Lorentzian fit is used to provide both the position in X and Y of the source, using the mean fit values along the cuts taken where the bin with the maximum number of conic intersections is and the image FWHM. The fit is placed on a quadratic background allowing an improved measurement of the FWHM to be made, as not all of the conic overlaps present on the distribution add to the final image. Conics are rejected which will not fit onto the intensity map however others will be present due to random coincidences and also coincident events which do not fully deposit their energy.

The imaging code provided uses a series of gates to select data, these are selected on energy and also scattering angle. The energy gate will be used to place a gate around the photopeak seen within an addback spectra, the image will therefore only be created from events which have an addback energy within this selection. The angle gate is used to select data which scatters within a given selection of angles, this is especially useful at lower gamma ray energies as the increased likelihood of backscattered events can cause the source location to become lost in the image generated. All the images produced will have the detector system centred on (430,430), the use of this offset is required by the imaging code.

A variable bin size is used for the 2D image intensity map. This bin size, called the image compression, can be optimised by the user to match the available statistics, provide a good quality of image visually, allow the fitting program to fit the data properly and also the image size if known. As the image compression is increased the associated error on the source position and the image FWHM will also increase, the likelihood of a conic crossing a bin will also be increased so the statistics will not be scaled by the compression value. Examples of this can be seen in Figure 3.10. In these examples a 3mm and 5mm compression have been used, showing that the fit is better with the 5mm compression, but the image is visually more diffuse while the FWHM is actually better at 3mm. The user must decide on the compression to be used, the value used for each image created will be stated. The compression of the image and the error in the fit to measure the FWHM and position provide an estimation of the error in the final image. Half of the compression value will be added in quadrature to the error associated with the fit to provide an estimate of the error on the reconstructed image position and FWHM.

3.3.2 Iterative

Iterative reconstruction algorithms generate an image by using successive estimations of the source location. The projections produced from the estimate are compared to the measured projections and the result of the comparison is used to create a new estimate.

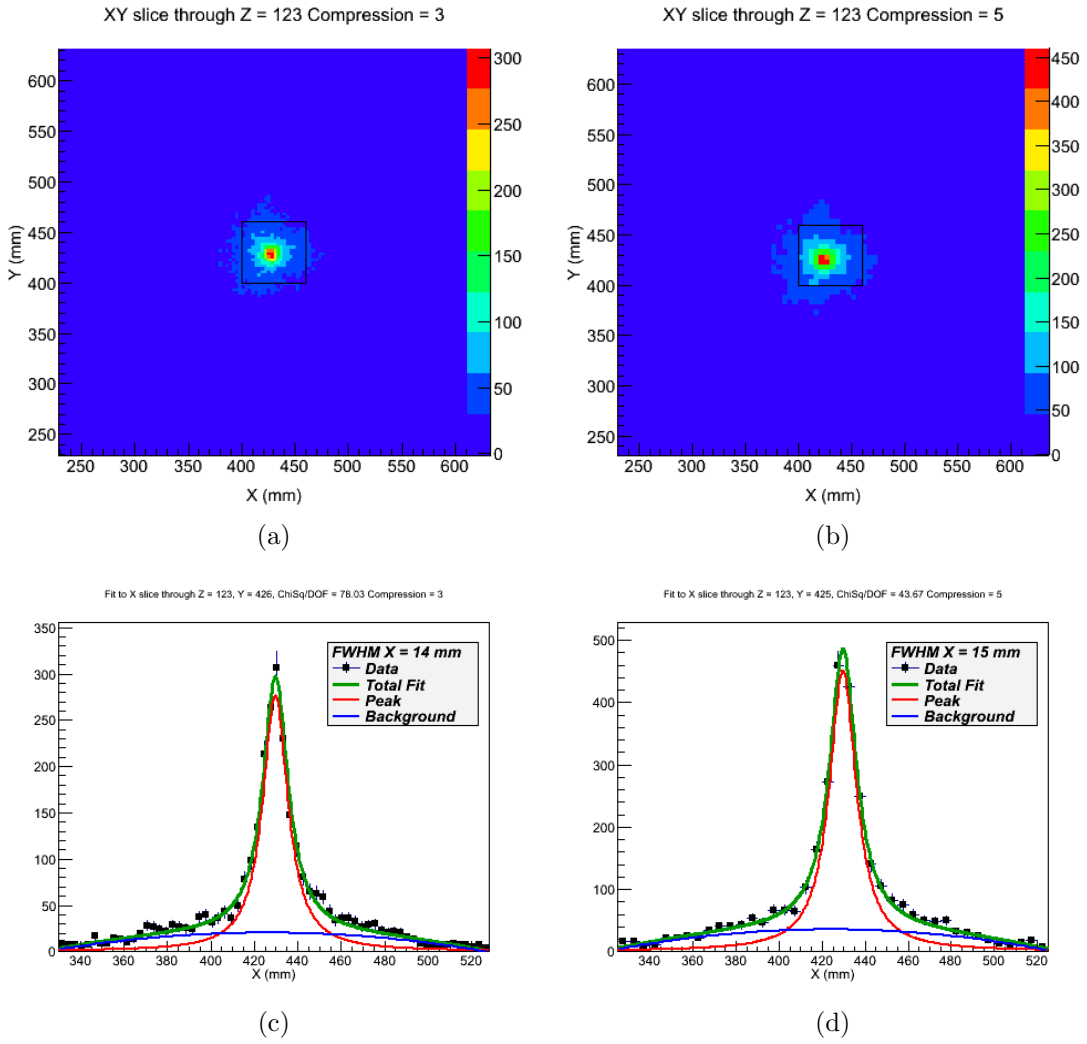

Figure 3.10: Examples of different compression factors, 3 and 5 mm. The image and cut through shown in (a) and (c) are using a 3mm compression, while those in (b) and (d) are using a 5mm compression. From these examples it is clear that although the statistics improve the FWHM of the image increases as the compression increases.

The majority of algorithms discretize the image into pixels, treating each pixel value as an unknown. A system of linear equations can be setup using the detector and source geometry along with Compton kinematics. The iterative algorithm then solves the linear equations. The first estimate of the image is normally to set every pixel to a constant value, usually 0 or 1 depending upon the algorithm being used.

An iterative algorithm will converge at first to a recognisable image and will subsequently diverge to noise. Iterative algorithms will in general produce better images then an analytical method as they can deal better with noise, non-uniform attenuation and other factors. The computational power required is much larger than that needed for an analytical algorithm so the image will take a longer time to generate.

A variety of different algorithms are available which principally differ by the methods

used to compare the measured projections with the current estimate. Large numbers of different iterative algorithms are available, the most commonly used iterative method is Maximum Likelihood Expectation Maximisation (MLEM) which is used widely in nuclear medicine for SPECT imaging, an indepth description of the MLEM algorithm can be found in [37].

Chapter 4

Detector and electronics overview

This chapter will introduce the two detectors chosen for this work along with providing information on the electonics setup used. Both detectors are double sided strip detectors (DSSD's) to provide the position sensitivity required. The electronics system includes state of the art digitisers and a fully digital trigger system.

4.1 Detectors used

The details outlined in Chapter 3 were used to select two detectors for this project. Two DSSD's, one made from silicon and another made from hyper pure germanium were selected. The silicon scatterer is a low Z semiconductor, allowing a minimum of Doppler broadening, good Compton scattering cross section and a good energy resolution. The germanium absorber has an excellent energy resolution allowing good spectroscopic performance.

4.1.1 Silicon lithium (SiLi) scatter detector

A Si(Li) detector manufactured by Canberra was chosen for use as a scatterer and is characterised in [38]. The detector is a circular DSSD. The detector has an active volume of 3500mm^2 with a strip pitch of 5mm with 13 strips per side and a thickness of 8mm. It has a guard ring which is 8mm in depth and had a width of 5mm.

The detector can be operated at room temperature but to minimise any leakage currents and thermal excitations a Canberra Cryo-Pulse 5 mechanical cooler is used, cooling the detector to 99K. The Cryo-Pulse 5 unit is a modified Sterling engine, designed to be stable and maintain the required temperature while providing the minimum of vibration at the detector crystal hence reducing any microphonic effects. A +150V bias voltage is required to fully deplete the detector and the detector was biased to +460V for this work.

Each strip is connected to a Canberra charge sensitive preamplifier providing 26 output channels. The output of the preamplifiers is 500mV for an energy deposit of 1MeV. The preamplifiers are configured with a cold FET (Field Effect Transistor) to

provide a low noise level. The strips are arranged orthogonally on either side of the detector. The AC side has a p-type contact (strips 1-13, termed AC01 to AC13) while the DC side has a n-type contact (strips 14-26, termed DC01-DC13). The strip layout can be seen in Figure 4.1a.

The detector is contained within a purpose built cryostat which Canberra designed to have a minimum of shielding materials while providing a large number of outputs. A cross section of the cryostat can be seen in Figure 4.1b with the detector unit as a whole shown in Figure 4.1c.

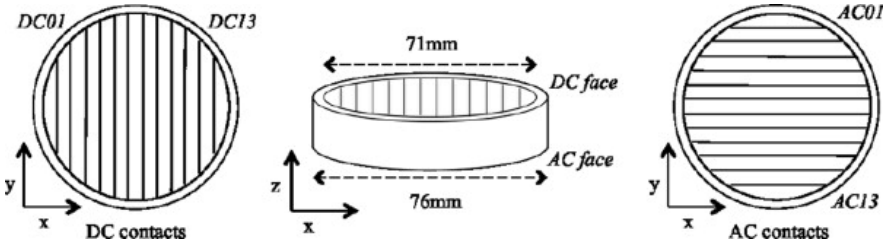

(a)

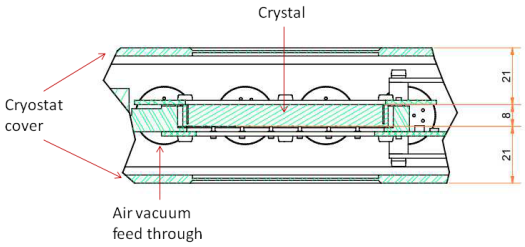

(b)

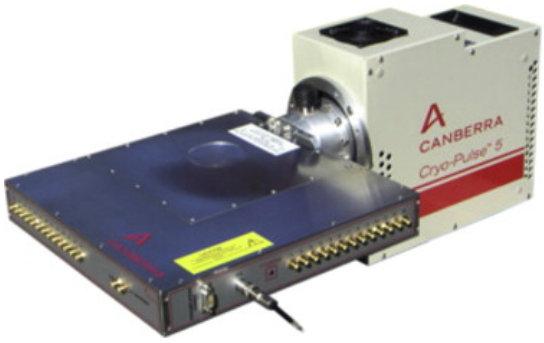

(c)

Figure 4.1: Schematic diagram of the strip configuration of the SiLi detector used as a scatterer (a) along with pictures of the detector unit itself (b) and (c). Images (a) and (c) are reproduced from [38]. Image (b) was provided by Canberra France.

4.1.2 DC01 and AC13

One channel of the SiLi detector was found to be not working. Channel DC01 produced no output when connected to an oscilloscope, and replacing the preamplifier for this channel did not correct this. The fault appears to be on the cold side of the feed through which would require the detector to be opened to atmosphere for an investigation to take place, which would lead to the loss of valuable time and the possibility of further damage to the detector's performance following any repair work. As the strip affected is an edge strip and there were only 24 channels of electronics available to instrument the Si(Li) detector the decision was taken to use the detector but not instrument DC01 and AC13, removing two of the small edge strips which should have a negligible effect on the efficiency of the detector.

Energy Resolution

The energy resolution for each strip of the SiLi detector was measured using an ^{241}Am and a ^{137}Cs source. These sources provide gamma rays of 60keV and 662keV respectively and the results are shown in Figures 4.2a and 4.2b. An Ortec 671 spectroscopy amplifier (Shaping time of 3μs) and Ortec MCA were used to take the measurements with Maestro 6 being used for the analysis. Measurements were taken with the sources on the AC side and then the DC side. The manufacturers measurements are also shown, taken at 60keV with a 3μs shaping time in Figure 4.2a. The values measured at Liverpool have a 10% error.

The results taken at Liverpool compare favourably to those provided by Canberra. The measured energy resolution is between 0.9 and 1.4keV at 60keV for all channels.

4.1.3 High purity germanium absorber detector

The absorber detector used for the system is a 75x75x20mm HPGe DSSD with an active area of 60x60x20mm surrounded by a guard ring. The detector has 12 strips on each side with a strip pitch of 5mm. Each strip is connected to a charge sensitive Ortec preamplifier with a warm FET configuration. The preamplifiers used have a response of 300mV for a 1MeV energy deposit. This detector has been previously used as part of the SmartPET project at Liverpool and was fully characterised and described in the following references [39, 40, 41, 42, 43] among others.

Capacitive charge sharing is commented on in [41] for the DC11 strip of the HPGe crystal used. This causes the strip to share charge between the two neighbouring strips. The result of this charge sharing is a reduction in the number of fold 1 events which occur in DC11, reducing its effectiveness when used for Compton imaging. The detector shows excellent energy resolution with values of $\leq$ 1.5keV for all strips at 122keV apart from DC11, which has a broadened photopeak due to the charge sharing [43].

4.2 Digital electronics

This work utilised state of the art digital electronics manufactured by CAEN, allowing the pulse shapes of each channel to be recorded for analysis and digital triggering to be used. This is the first time these electronics have been used for a multichannel detector system used as a Compton camera. The digital electronics can fit into one standard VME crate, while the detectors and preamplifiers are powered from a standard NIM crate using appropriate modules. This makes the system more portable compared to using analogue electronics modules to create an appropriate trigger system which can use up to three NIM crates for triggering, another for HV and preamplifier power supply and either a VME or NIM crate to output signals to the DAQ.

A schematic of the electronics used to process the data signals can be seen in Figure

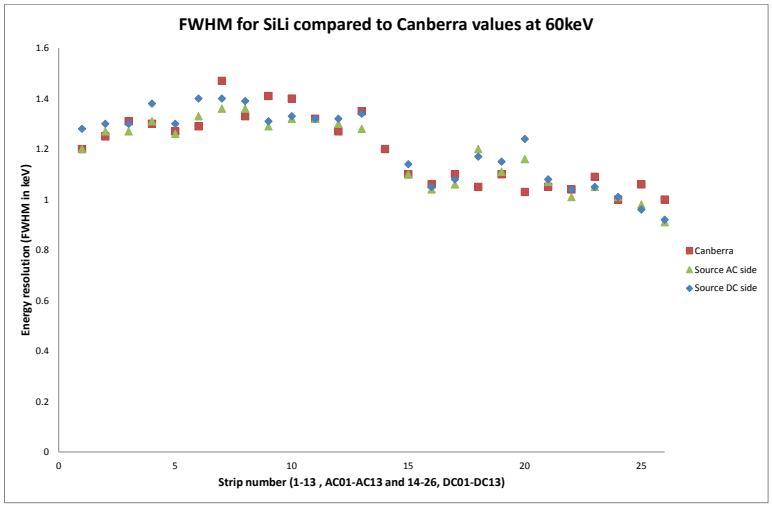

(a)

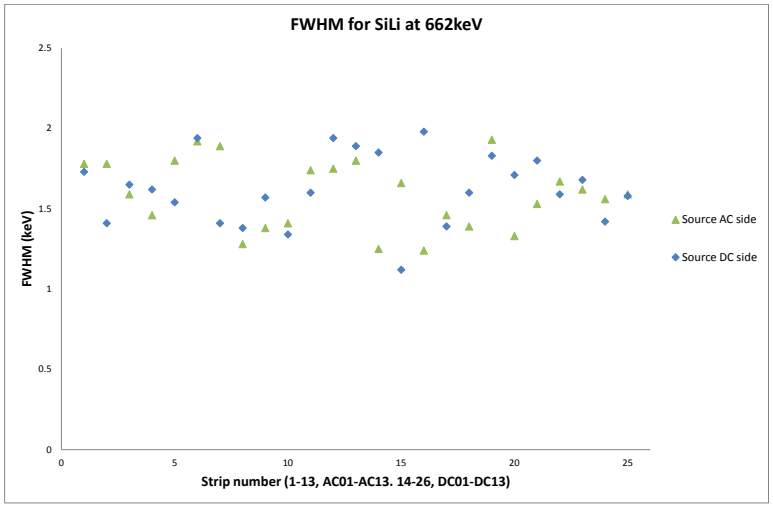

(b)

Figure 4.2: Energy resolution measured for the SiLi detector. (a) shows the energy resolution at 60keV for the AC side and DC side compared to measurements taken by Canberra, with the source in different locations.(b) shows the energy resolution at 662keV for both sides of the detector.

4.4. The function of each unit will be introduced briefly, for further information please refer to the manufacturers handbooks for the appropriate modules.

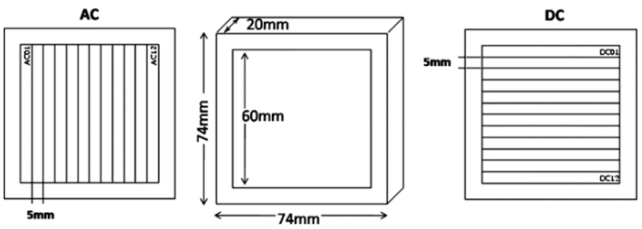

(a)

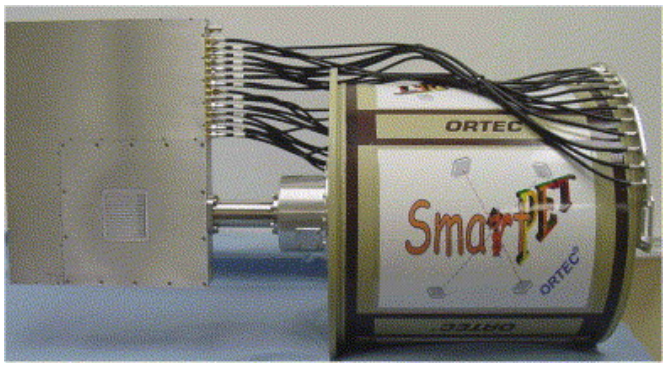

(b)

Figure 4.3: Schematic diagram of the strip configuration of the HPGe detector used an absorber (a) along with a picture of the detector unit itself (b). Image (a) reproduced from [41]. Image (b) reproduced from [42].

4.2.1 High voltage (HV) and preamplifier power

To provide the bias voltages to the detectors two HV units were used. Two Ortec 671 amplifiers were used to provide the preamplifiers with power. The four units are NIM powered and placed into one high power crate, allowing for simple grounding and easier transportation.

The two detectors require different bias shutdown methods. A bias shutdown prevents HV being applied in the event that the detector warms up, preventing any damage that may occur due to contaminants being released into the vacuum from the molecular sieve. Typically this out-gassing will result in a spark across the crystal if the HV is still applied, leading to the FET on the preamplifiers blowing or in extreme cases the crystal itself cracking.

To provide the correct bias shutdown methods a Canberra 3106D HV supply was used with the SiLi detector, while an Ortec 659 HV supply was used with the HPGe detector.

4.2.2 GO Box

The dynamic range available on the CAEN V1724 card is 2.25V. This is very large compared to the output voltages per 1MeV of energy deposited that the detector preamplifiers provide. To better match the dynamic range of the cards to the energy range

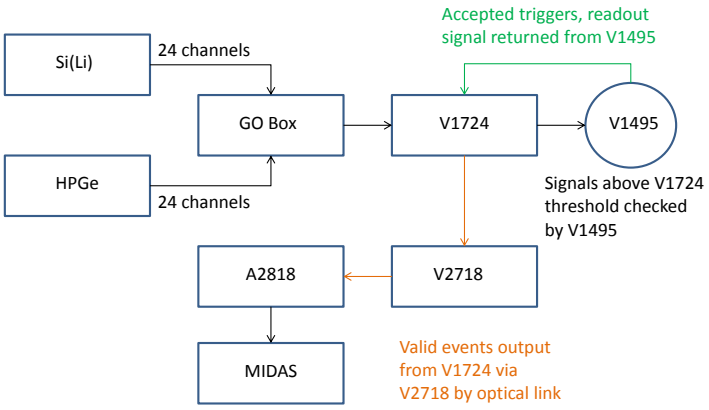

Figure 4.4: Flow diagram of the digital electronics used for this work. The GO Box provides an amplified signal from each detector output to the CAEN V1724 digitiser cards. Energy thresholds are set on the V1724's and the signal from any channel which is above the appropriate threshold is passed to the CAEN V1495 trigger control card. The trigger logic programmed onto the V1495 is checked and if passed a signal is sent back to the V1724's to read out the appropriate data to the MIDAS data acquisition software via an optical link using the V2718 and A2818.

of interest a fixed gain of a factor was put into place by using a gain offset box (GO Box). This GO Box allows a separate offset for each channel to be applied, as each pre amplifier has its own DC offset this allows them all to be set to a common level. The gain is fixed at a factor of 10, 5 or 2 and is set by changing an electronics board inside the unit, with the 5 and 10 times boards being used for the work discusses in Chapters 5 and 6 respectively. The GO Box was designed and built at the University of Liverpool.

4.2.3 CAEN V1724 Digitiser

The CAEN V1724 digitiser was used during this work. The digitiser has 8 channels on each card, running at a sampling rate of 100MHz with 14 bit resolution. Each channel is processed and controlled individually, with trigger levels, moving window deconvolution and other settings being set within the browser based control software. Six of these cards were used providing 48 channels of electronics. The cards are placed in a VME crate. Full information on the V1724 can be found at [44].

The 100Mhz clock of the first card is daisy chained across all the others allowing a common clock to be used for all the cards. This clock is used to check whether events are correlated correctly and allows us to be certain that events recorded occurred within a set time window.

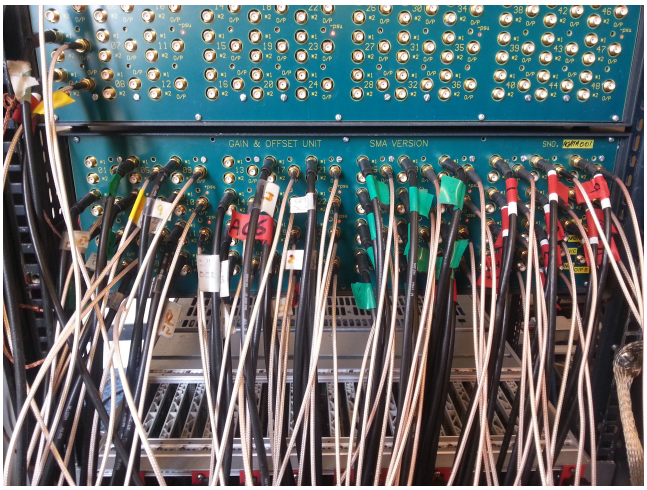

Figure 4.5: Picture showing the gain/offset (GO) box used to provide additional amplification to the preamplifier signals and also provide a common baseline level.

Figure 4.6: Picture showing the CAEN V1724 digitiser cards in a VME crate. 3 cards are shown with the clock and optical readout cables in place, along with the V2718 optical link bridge card which is at the left hand side of this image.

The cards can provide a data readout from either the VME databus or an optical link. The optical link provides a faster readout and was chosen for this work. Within the software it is possible to enable only certain channels, this makes checking individual channels trigger levels easier as the channel does not have to be disconnected from the electronics.

4.2.4 CAEN V1495 Trigger logic controller

The trigger outputs from each V1724 are fed to the V1495 trigger logic card, full details of this card can be found here [45]. This card is programmed with the trigger methodology used for a particular project. The trigger outputs from the V1724 for each event are checked against this logic and the card will either accept or reject the event. There is also an option to write out only the channels which trigger the system or all of the channels which are enabled or the channels which trigger along with their nearest neighbour.

For this project the trigger could be used to two ways, either singles mode used for calibration or in Compton mode for data collection. Singles mode will allow the system to record any triggering event, so if any channel activates the trigger the DAQ will record this event. Compton mode sets the requirement that an event must include at least one channel on each side of each detector activating the trigger within a given time window. The time window width is set within the software.

4.2.5 CAEN V2718 Optical link bridge

The outputs from the V1724's are passed to a CAEN V2718 using optical fibres. This card acts as the VME controller, passing the configuration from the control PC to the cards via a A2818 PCi controller using optical fibre. The data is also transmitted through the bridge to the PC for analysis software, MIDAS, to process. The data transfer rate is up to 100MBytes/s using CONET2 (Chainable Optical Network) protocols.

4.2.6 MIDAS

MIDAS, Multi-Instance Data Acquisition System, is a data acquisition software package designed for the STFC at Daresbury. This package runs under a Linux, Windows or Sun OS environment, allowing full control of the system via a PC. An HTML link is used to control the settings on individual V1724 channels and also the V1495 settings.

4.3 Energy calibration

Each individual channel and preamplifier will have its own response to energy deposition resulting in slightly different voltages from each one, therefore calibration must be carried out on each individual channel to align all of the signals to the same energies.

Calibration is carried out using one or more gamma ray sources which have gamma-ray decays with well defined, known energies. Ideally the source or sources used should have a number of energies with a wide energy range, an example would be ^{152}Eu which has multiple gamma rays ranging from 121keV to 1408keV.

Due to the limitation of getting a high energy gamma ray to deposit all of its energy in the Si(Li) detector used for this work an ^{241}Am and a ^{137}Cs source are used to calibrate. These provide energies from 17keV to 662keV utilising X-rays and gamma rays from the ^{241}Am and ^{137}Cs sources. A quadratic fit is applied using the 17.05 and 32.2keV X-rays with the 59.5keV and 661.7keV gamma rays present from these two sources. This method is used unless otherwise stated.

For the HPGe detector calibration is carried out using a ^{152} source A quadratic fit is performed using the 122, 344, 778, 964 and 1408keV gamma rays. Multiple peaks provide a better fit for a quadratic function. The fit is then used to shift the energy spectra seen from each channel to an bin/energy ratio which is the same for all of the channels.

An example of two input channels can be seen in Figure 4.7(a), this is a calibration using strips AC01 and AC12 of the HPGe detector showing the 122keV photopeak from each. In Figure 4.7(b) the channels have been calibrated to the same channel to energy ratio of 0.5keV/channel.

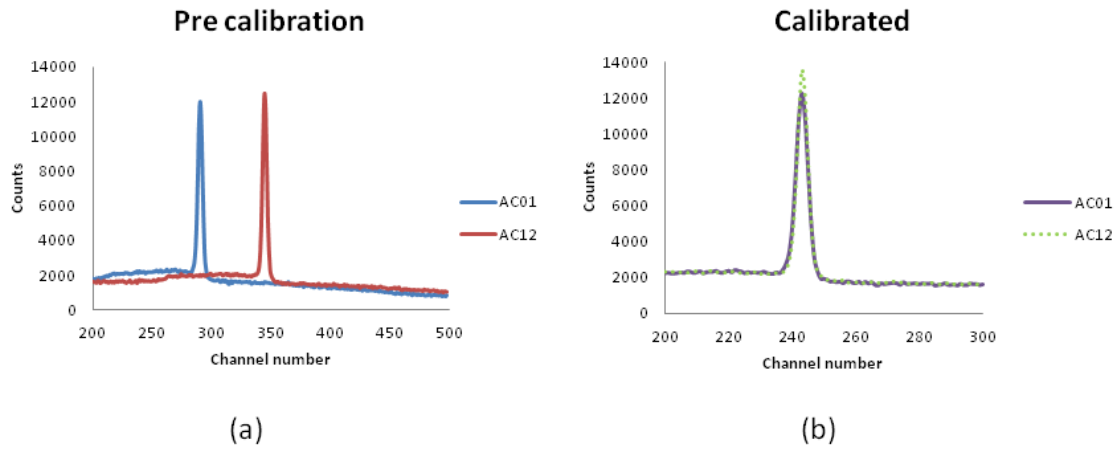

Figure 4.7: Energy spectra demonstrating the calibration of two channels of the HPGe detector. The calibration matches all of the channels to the same bin to energy ratio. A quadratic fit is used across a wide energy range using sources that provide known gamma ray energies, this example shows the 122keV gamma ray in ^{152}Eu with a channel to energy ratio of 0.5keV/channel.

Chapter 5

Experimental results from Liverpool

Measurements were taken at Liverpool to provide information on the energy response, image reconstruction and Compton efficiency of the detector system. These measurements were taken after those presented in Chapter 6, they are presented first as they show the best possible results from the detector system as it currently stands. A variety of different point sources and an extended source were imaged with the results presented in this chapter. The time resolution between the scatterer and absorber will also be investigated to set a trigger width correctly.

A scanning table was used to align the detectors properly and also to position the sources within ± 5mm in X and Y. The source placement error in Z was also ± 5mm. The mounting of the detectors and the positioning of sources for measurement can be seen in Figure 5.1.

5.1 Detector setup

The detectors were mounted co-planar to one another above a scanning table containing a 1GBq ^{137}Cs source which is pin hole collimated to provide a 1mm beam. This source was used to check the alignment of the detectors by performing a scan across the face of the scatterer in 1mm steps producing histograms of the number of hits at each position for each detector, the results can be seen in Figure 5.2.

When a different source was used lead shielding was put over the collimator hole allowing only the source of interest to be detected. The detectors were placed with a 13mm separation between the cryostats.

The Si(Li) detector was connected using 12 channels on each side, with one edge strip missing from each. Double peaking was noticed from DC02 however so this was removed from the DAQ, so 12 strips on the AC side and 11 strips on the DC side were used hence the shape seen in Figure 5.2.

Figure 5.1: Pictures of the Compton camera system mounted above the scanning table at Liverpool. The scanning table was used to align the detectors to within ± 1mm using the 1GBq ^{137}Cs collimated source contained within the table, this source was shielded with lead to prevent any interference with measurements taken after the alignment.

5.2 Energy Calibration

To calibrate the silicon detector an ^{241}Am and a ^{137}Cs source were used. These sources were chosen as the full energy deposition peaks are readily visible and the energy spacing is as wide as possible. A ^{152}Eu source could not be used as the full energy peaks above 300keV were not visible, this is due to the Compton scattering cross section in silicon dominating in this energy region so the photopeaks are not discernible due to a high Compton background. The 17.1keV X-ray and 59.5keV gamma ray from ^{241}Am along with the 661.7keV gamma ray from ^{137}Cs were used to perform a quadratic calibration.

The HPGe detector was calibrated with a quadratic fit using an ^{152}Eu source. The 121.8, 344.3, 778.9 and 1408.0keV gamma rays were used.

Energy thresholds of 13keV in the scatterer and 30keV in the absorber were set channel by channel. These values were set to minimise the noise levels seen from the detectors. All energy information has been taken from [46], branching ratios for multiple energy sources used can be found in Appendix C.

The image resolution will be presented as an average of the values found in X and Y when the source is assumed to be a point or circular. An angular resolution will also be calculated for the point source measurements. By taking the average FWHM

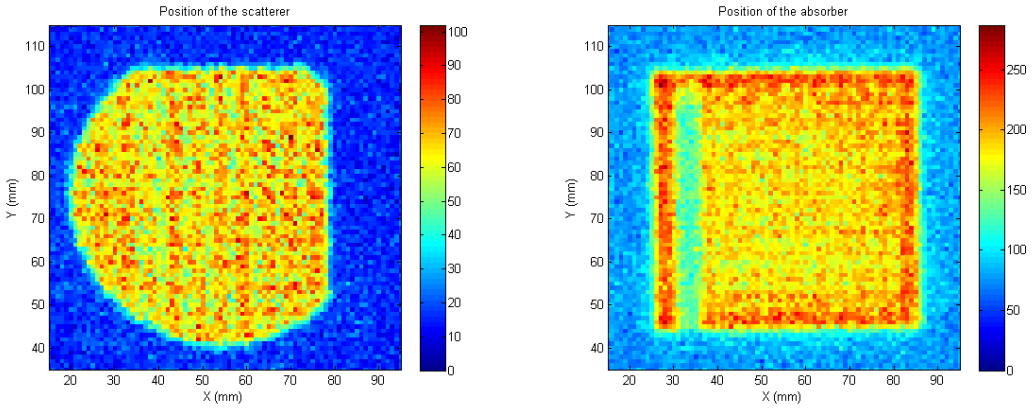

(a) (b)

Figure 5.2: Position histograms showing the scatterer (a) and absorber (b) generated by scanning the Compton detector system with a 1Gbq ^{137}Cs source mounted in a scanning table. The raster scan was carried out in 1mm steps with the source in one position for 10 seconds. The centres of each detector are aligned to within 1mm of each other in X and Y. The scatterer is missing one strip from the AC (AC13) side and also two strips from the DC (DC01 and DC02) side, this is due to double peaking being seen from DC02 and DC01 and AC13 being removed for previously stated reasons. The images here are fold 1 gated, so DC11 on the absorber is missing due to its lack of fold one events.

for each of the images we can use one figure to compare the image resolutions. This value can also be converted into an angular resolution so comparisons can be made for sources at different distances as the angle removes the image resolutions dependence upon source to detector distance. The equation used for this can be seen in Equation 5.1, where D_z is the distance to the source from the centre of the scatterer.

$$\text{Angular resolution (degrees)} = 2 * \left[tan^{-1} \left(\frac{\left(\frac{\text{Average FWHM}}{2} \right)}{D_z} \right) \right] \tag{5.1}$$

5.3 Timing resolution

Coincidence timing between two detectors is an important factor when designing a coincidence counting system including a Compton camera. The timing interval between coincident events can be measured using a time to amplitude converter (TAC), this provides a voltage output based on the difference in time between a start and a stop pulse. True coincident events will generate a peak if the TAC output is measured on a multi channel analyser, the FWHM of this peak generated will provide the time resolution for the system, thus giving a measurement for the trigger width required to measure true coincident events between the two detectors.

The trigger coincidence window at Aldermaston, Chapter 6, was set arbitrarily to

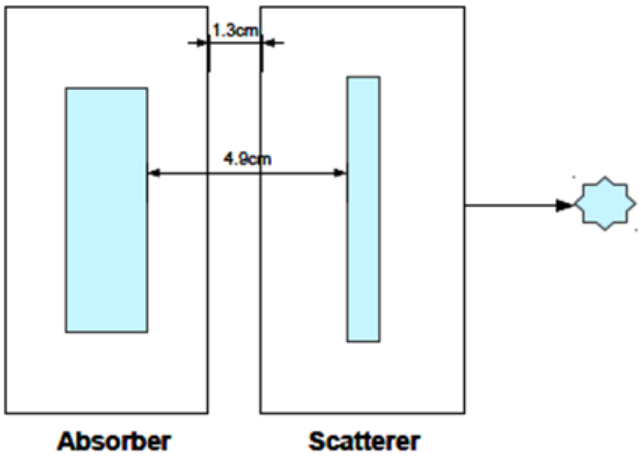

Figure 5.3: Schematic diagram showing the detector separation used for the experiments at Liverpool.

75ns in width, this was thought at the time to be enough to provide a wide enough trigger between the two detectors. To check this the time resolution was measured between the detectors.

To measure the time resolution between the Si(Li) and HPGe detectors, one channel from each was instrumented. Channel 8 of the Si(Li) was chosen as this is a central strip and on the side facing the source position, AC6 was used on the HPGe as this strip was located on the side closest to the source position. A Ortec TFA was used for both detectors, along with a LeCroy leading edge discriminator (LED). Delay was introduced to the Si(Li) signal as this was chosen to be the stop for the TAC. An Ortec TAC was used, the output was then passed to an Ortec MCA and Maestro 6 was used to view the output. The threshold of the LED's was set to be 500keV and a ^{22}Na line source was placed between the two detectors, providing back to back 511keV gamma rays from its positron emission. The source was slightly closer to the HPGe due to the detector cryostat layouts and crystal thickness involved. The setup can be seen in Figure 5.5.

The result from MAESTRO can be seen in Figure 5.5, this peak has a FWHM of 152ns and a FWTM of 298ns for 511keV gamma rays, indicating that a trigger length of around 250ns will encompass $\sim$ 88% of the true coincidence events between the detectors. The trigger coincidence window was set to 250ns for the work at Liverpool. The width of the TAC peak is due to the large variances seen in the rise times from both detectors. Ideally a width of 350ns would encompass the full peak but this measurement was taken after all the Compton data was collected.

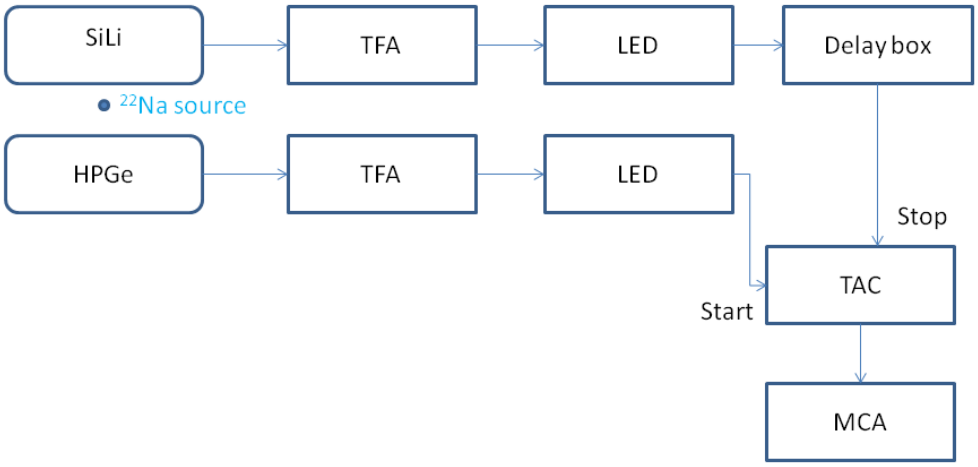

Figure 5.4: Flow diagram of the electronics used to measure the time resolution between the two detectors. The time to amplitude converter (TAC) provides an output with a voltage proportional to the time difference between signals received at its start and stop inputs.

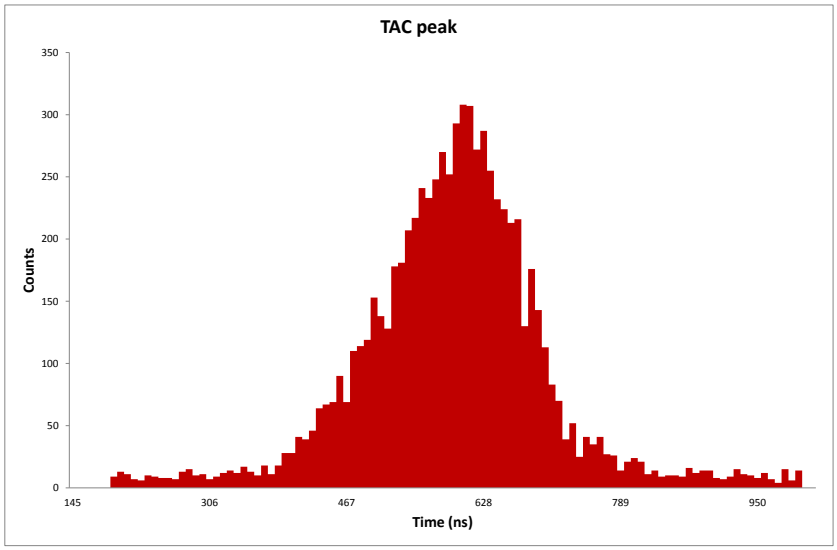

Figure 5.5: Time coincidence peak seen in MAESTRO between the scatterer and absorber detectors. The FWHM of this peak is measured as 150ns, with a FWTM of 298ns. These values indicate that a coincidence trigger window of 250ns should be adequate to encompass the majority of true coincident events between the detectors. The measurement was carried out at 511keV.

5.4 Point source measurements

A selection of point sources was chosen to examine the energy response and efficiency of the detector system. The method for finding the distance to a source was also investigated using the point sources and pulse shape analysis was applied to some of the data to indicate the improvements in imaging resolution it can provide.

Initial measurements were taken with sources held central to the detector, at different distances. The sources unless otherwise stated are mounted in glass slides, with very small embedded points of the appropriate nuclide so approximate to point sources. The positioning of each source has an error of ± 5mm in three directions.

5.4.1 Compton efficiency

The absolute efficiency, ϵ_{abs} of the detector is measured using a ^{152}Eu source with a known activity. This source provides a range of gamma rays (122 to 1408keV). Equation 5.2 is used to present the absolute efficiency [15], this measurement takes into account the source and detector geometry. The Compton efficiency measurement here uses the data from the addback spectra, Figure 5.6 generated in Compton mode for the source

$$\epsilon_{abs} = \frac{\text{number of pulses recorded}}{\text{number of radiation quanta emitted from source}} = \frac{\text{Net counts}}{\gamma_b * \text{Activity (Bq)} * \text{LT (s)}} \tag{5.2}$$

The branching ratio, γ_b represents the probability of emission for a particular gamma ray and live time, LT takes into account any dead time in the system. The time for the measurement to be taken has to be corrected for any possible dead time, caused by events piling up, the detectors being insensitive to incident radiation for a brief period following an interaction and any processing time in the digital electronics. To achieve this a single strip on each detector was connected to an analogue pulse counting chain with an energy threshold set to the same as that on the digital system. The analogue system should have no dead time as fast timing electronics were used, comparing the average count rate seen on the analogue setup to that seen on the digital electronics provides an estimate of the dead time. AC06 of the scatterer and AC06 of the absorber were chosen as they are central strips in each detector.

Digital electronics should be dead time free however the act of writing out traces for each channel introduces dead time as each pulse is processed, recorded and stored. The system uses 48 channels, and writes out 128 samples from each one whenever an event is processed. A comparison to analogue electronics can provide a guide to the dead time in the system. Utilising single strips from each detector will provide an underestimate of the dead time as only a single trace is being processed for each event, results are shown in Table 5.1. The maximum dead time measured was 9.9% provided by the absorber, a value of 10% is used for the efficiency calculation. This value is likely

to be an underestimate however without a full dead time analysis when the system is writing out 48 channels with the pulse traces associated to them an exact value cannot be calculated.

Scatterer		Absorber	
Analogue (cps)	Digital (cps)	Analogue (cps)	Digital (cps)
831	743	698	643
861	727	718	660
806	831	783	669
856	784	741	664
856	801	729	648
851	768	776	699
827	771	769	671
831	756	709	679
824	790	724	661
809	757	741	661
Average values			
835	773	739	666

Table 5.1: This table shows the counts per second (cps) recorded for a single strip on each detector through an analogue system compared to the digital system. The analogue circuit should have no dead time, so this provides an estimate of the dead time caused by the digital electronics. The average values of each are compared as a percentage to give a 7.5% dead time for the scatterer and a 9.9% dead time for the absorber. A value of 10% will be used for the efficiency calculation to allow for the reading out of 48 channels worth of data rather than just single channels.

For this measurement a 158.6kBq ^{152}Eu source was placed 11.6cm from the front face of the scatterer for 442036s, this time is adjusted to a live time by applying a 10% correction. The net counts and energy resolution are shown in Table 5.2. The energy resolution is important for identifying the radionuclides present within an object and is a combination of the energy resolutions of both detectors. The efficiency is measured and plotted against the gamma ray energy in Figure 5.7, a counting error is shown for each point and systematic errors are estimated to be 10% for each point is used to allow for errors in the placing of the source and source activity this does not allow for any errors in the dead time calculation however.

The energy resolution measured at Liverpool is slightly larger than that measured in Aldermaston (see Table 6.3). This is due to the calibration performed at Liverpool being different to that at Aldermaston, as this data uses a linear calibration for the SiLi detector across a much smaller range than that calibration used at Liverpool.

^{152}Eu images

For comparison to the data collected at Aldermaston, images were generated for the 122, 244, 344, 443 and 778keV peaks. In addition images were also generated for the

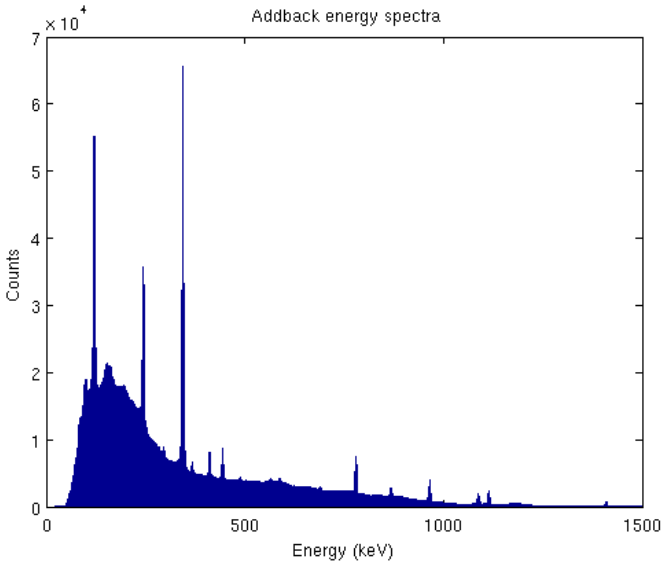

Figure 5.6: Addback energy spectra from a ^{152}Eu source. This energy spectra was used to produce an absolute efficiency curve for the Compton camera.

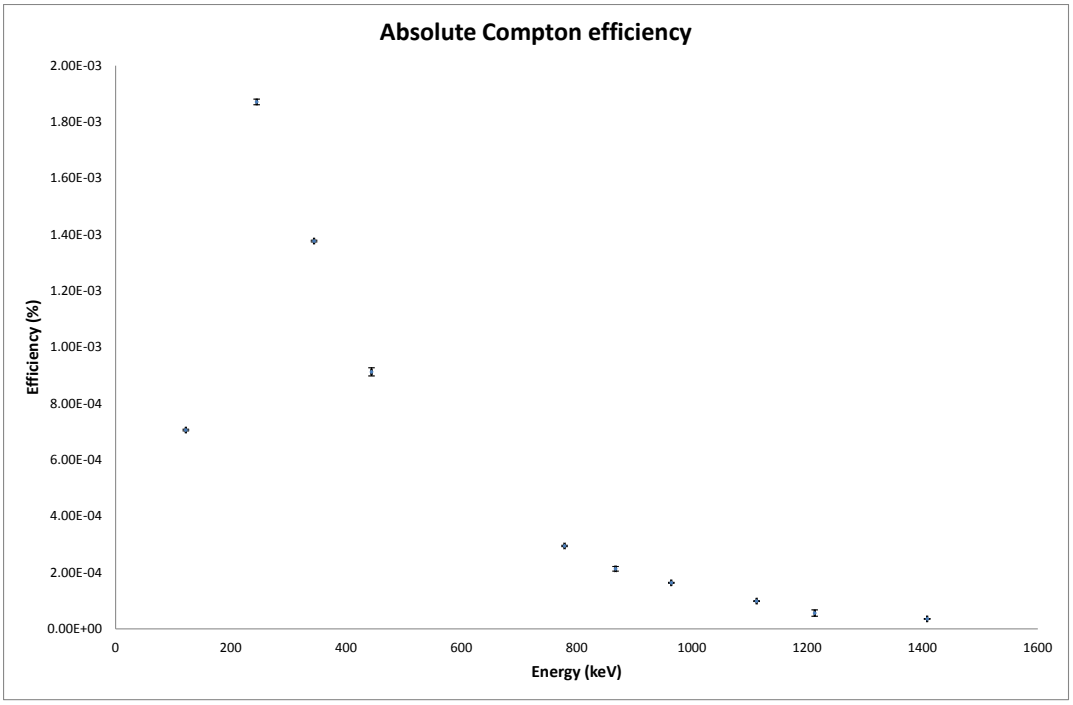

Figure 5.7: Absolute Compton efficiency for a ^{152}Eu source placed 11.6cm from the scatterer crystal. The error is estimated at 10% for each point allowing for counting errors, timing errors and any errors in the source activity.

Energy (keV)	Net counts	±	Energy resolution (keV)
122	126371	615	3.40
244	88875	533	3.85
344	230813	590	3.96
443	17990	318	3.95
778	24106	218	4.36
867	5671	241	4.48
964	15119	170	4.72
1112	8447	138	4.54
1212	498	110	4.80
1408	4705	73	5.92

Table 5.2: This table shows the spectroscopic information gained from the ^{152}Eu Compton run taken at Liverpool used for an absolute efficiency calculation. There is a 10% error on the energy resolution measurements.

1112 and 1408keV peaks as these are clearly visible on the addback spectra. The image produced for 122keV initially indicates that the source position is distributed widely across an area in the form of an annulus, this is due to the increased number of back scatter events caused by having the threshold levels so low in both the scatterer and absorber. By applying a gate on the Compton scattering angle calculated for each event the back scattered events can be removed, allowing a clear image to be formed, Figures 5.8a, 5.8b and 5.8c show the differences between a 0 to 180, 0 to 90 and 0 to 70 degree gate respectively. To create the image presented in Figure 5.9a an angle gate of 0 to 60 was applied to the data. This angle gate was chosen as it reduces the back ground on the image significantly but still allows enough cones to be used to generate the image.

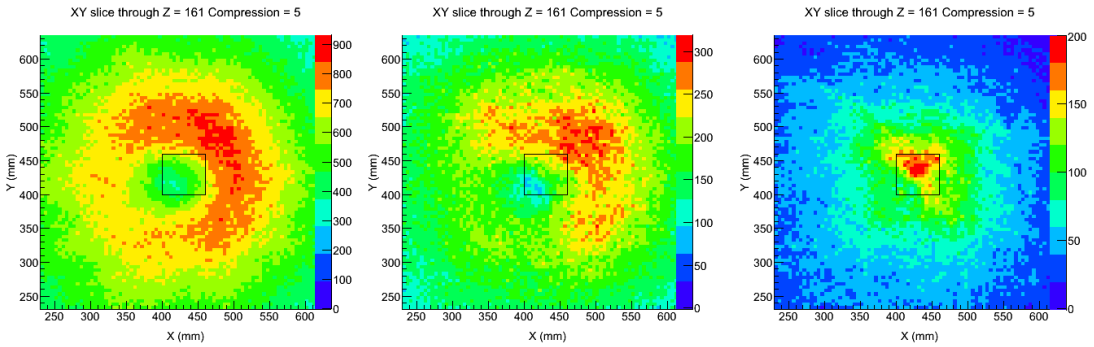

(a) (b) (c)

Figure 5.8: Images created by applying an energy gate around the 122keV photopeak of ^{152}Eu. The images have different angle gates applied, (a) 0 to 180, (b) 0 to 90 and (c) 0 to 70. The application of an angle gate on the Compton scattering angle for each event removes the back scattered events present creating a clearer image.

Angle gating removes data which does not contribute to the image directly. This

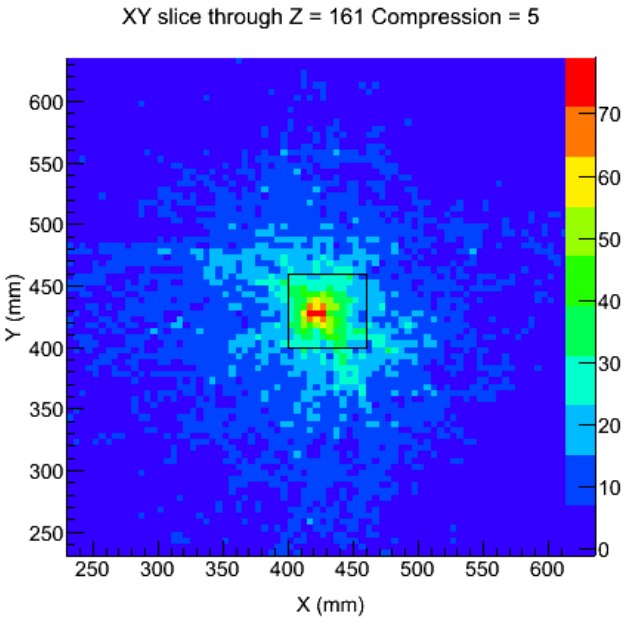

(a)

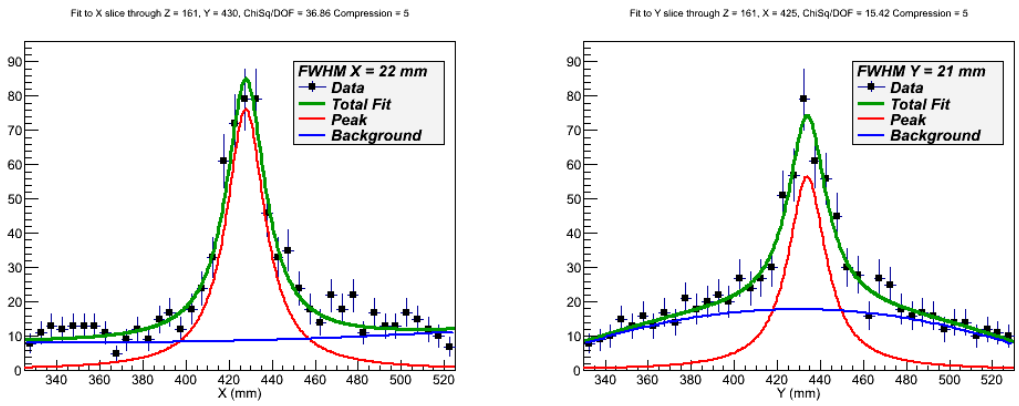

(b) (c)

Figure 5.9: The image produced by gating on the 122keV γ ray from ^{152}Eu with a 0 to 60 degree angle gate included is shown in (a) with a 5mm compression. The average FWHM of the image is 21.7mm $\pm$ 2.9mm. (b) and (c) are cross sections through the X and Y axis respectively, showing the Lorentzian fit to the data used to create the image.

includes gamma rays which are not fully absorbed in the absorber detector which contribute to the Compton continuum which is large under this peak. Back scattered events will also play a part in adding to the cones which are in the initial ungated image. The noise contribution at lower energy levels is higher, due to the low energy deposits from Compton scatters from low energy gamma rays resulting in more uncertainty in the cone angle.

Images were produced for all the peaks available and the information can be found in Table 5.3, the images not presented in this chapter can be found in Appendix A.1.

For comparison to the Aldermaston images, the image resolution has been converted to an angular resolution in Table 5.4. The image should reconstruct the point source to (430,430).

Energy (keV)	Position X (mm)	±	Position Y (mm)	±	FWHM X (mm)	±	FWHM Y (mm)	±
122	427.7	2.6	433.8	2.7	21.8	3.6	21.5	3.7
244	428.8	1.5	434.1	1.5	21.7	1.5	21.6	1.5
344	428.5	1.5	434.3	1.5	20.5	1.5	20.2	1.5
443	428.5	1.5	434.5	1.5	17.2	1.5	16.9	1.5
778	428.5	1.5	434.8	1.5	19.5	1.5	19.5	1.5
964	428.8	1.5	434.7	1.5	18.9	1.5	18.3	1.5
1112	428.5	1.5	434.1	1.5	19.6	1.6	19.5	1.6
1408	428.2	1.5	434.3	1.5	16.2	1.6	17.2	1.6
122,244,344,443,778	428.6	1.5	434.3	1.5	20.6	1.5	20.3	1.5

Table 5.3: Position and FWHM of the image from ^{152}Eu taken at Liverpool for 3mm compression, except for the 122keV image which was taken using 5mm compression.

Energy (keV)	Average FWHM (mm)	±	Angular resolution (degrees)	±
122	21.7	2.9	10.4	1.4
244	21.7	1.1	10.3	0.5
344	20.4	1.1	9.7	0.5
443	17.0	1.1	8.1	0.5
778	19.5	1.1	9.3	0.5
964	18.6	1.1	8.9	0.5
1112	19.6	1.1	9.3	0.5
1408	16.7	1.1	8.0	0.5
122,244,344,443,778	20.4	1.1	9.7	0.5

Table 5.4: Average FWHM and angular resolution of the images from ^{152}Eu taken at Liverpool for 3mm compression for all peaks except 122keV which has a 5mm compression.

The image resolution alters with energy, as seen in Figure 5.10. This alteration appears to be due to the Compton continuum on which the photopeak sits. The energy gate applied takes all counts which have a combined energy within the gate values, hence the Compton continuum is included when the image is created, these spurious counts will affect the final image resolution and as the peak to total value decreases the effect will increase.

The image for 1408keV is shown in Figure 5.11c.

The image produced from combining 122, 244, 344, 443 and 778keV is shown in Figure 5.12a. These peaks were chosen to provide comparison to the Aldermaston images, peaks above 964keV are not present in this data and the 964keV peak has very

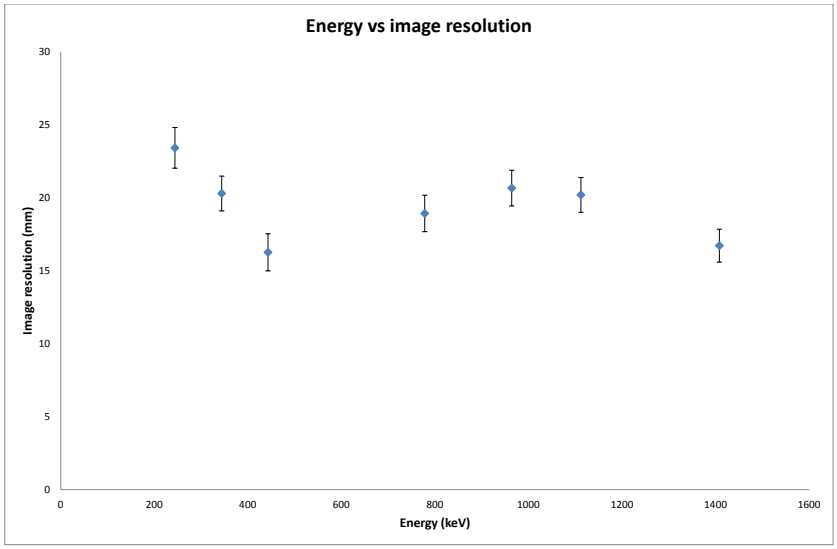

Figure 5.10: Average image resolution plotted against the gamma ray energy, the number of cones used to create the images has been limited to the same number providing a direct comparison.

few counts in the Aldermaston data.

The source is reconstructed to the correct position, (430,430) within the errors involved (placement, scanning table and the error on the image). The position remains constant across all the energies imaged.

5.4.2 ^{133}Ba

A ^{133}Ba source was used to test the Compton camera's ability to image below 100keV, using the 80keV photopeak. In addition measurements for this source could be compared to those taken at Aldermaston in terms of angular resolution. A thin (0.95mm) copper sheet was placed between the source and the detector system to absorb the low energy X-rays produced in the decay of ^{133}Ba, this reduced the probability of an X-ray being detected in coincidence with a gamma ray. The source was positioned central to the scatterer and 12.3cm from the front face of the scatterer.

Looking at the addback spectra, Figure 5.13 it is clear that the 80keV peak expected is present and clearly visible above the Compton continuum created from the higher energy peaks. The image in Figure 5.14a is produced by gating on the 276,302,356 and 383keV photopeaks and will be compared to the Aldermaston data taken with the same energy gates.

The source is reconstructed to the correct position within the associated errors as shown in Table 5.5. The Compton continuum under the energy peaks used here is low

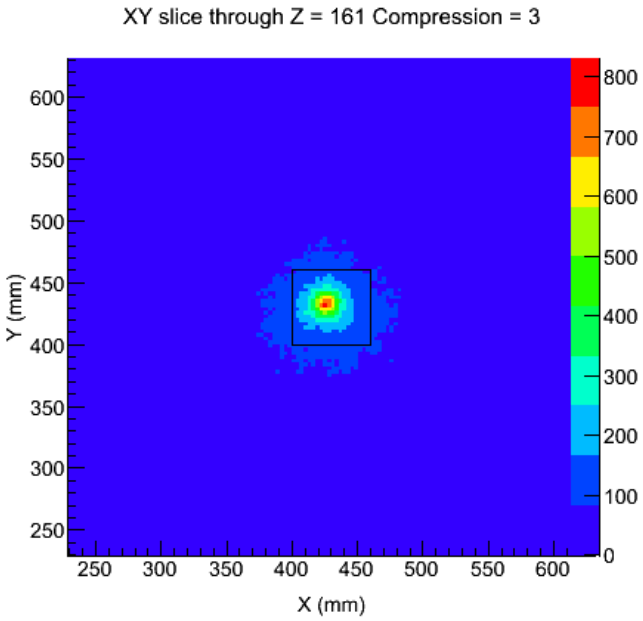

(a)

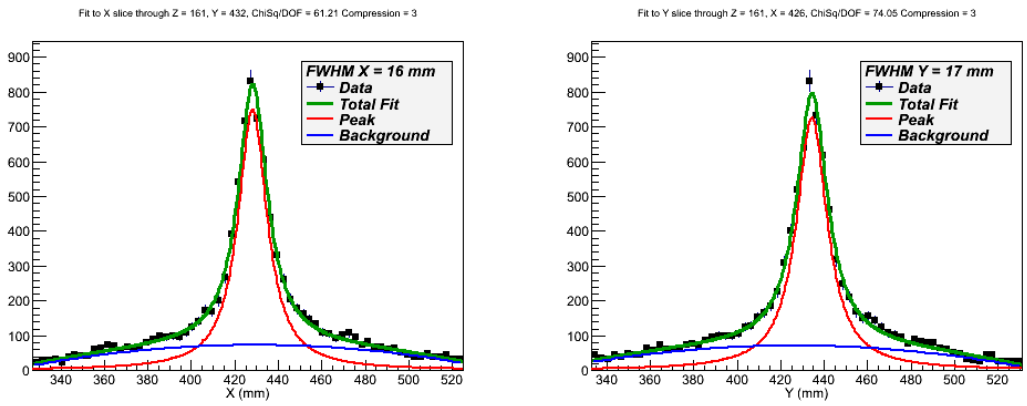

(b) (c)

Figure 5.11: The image produced by gating on the 1408keV γ ray transition is shown in (a). The average FWHM of the image is 16.7mm $\pm$ 1.1mm. (b) and (c) are cross sections through the X and Y axis respectively, showing the Lorentzian fit to the data used to create the image.

allowing a good image resolution to be achieved.

Figure 5.15a shows the image when an energy gate is placed around the 80keV peak seen in the addback spectra, an angle gate of 0 to 130 degrees is also used in this case. The source location cannot be identified without using a very high compression value, 25mm is used in this example to make the image visually identifiable and also to allow the imaging code to fit the image. By applying the energy and angle gates the number of cones which are available for reconstruction are drastically decreased however this removes the influence of the Compton continuum from higher energy peaks washing out the image and also the effects of back scattered events contributing to the image

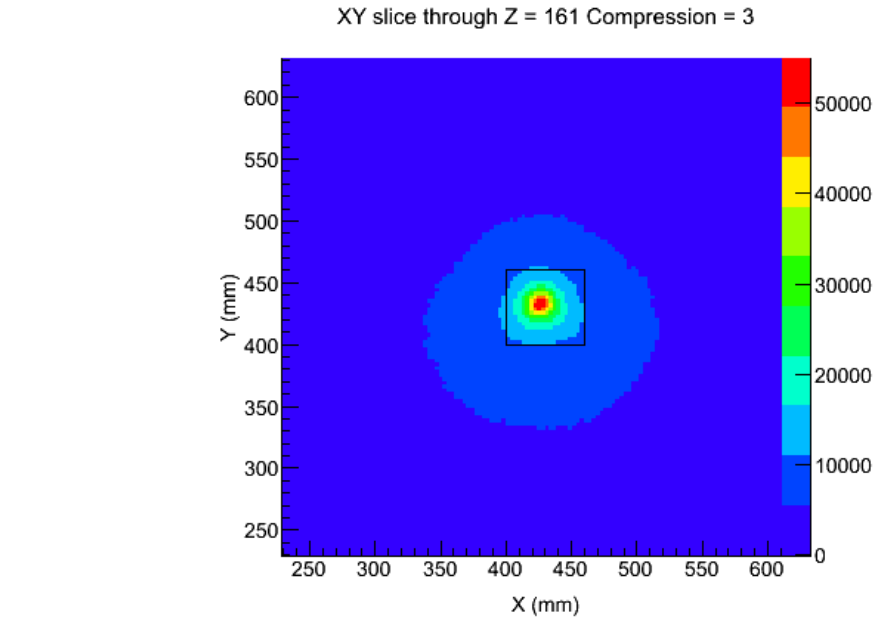

(a)

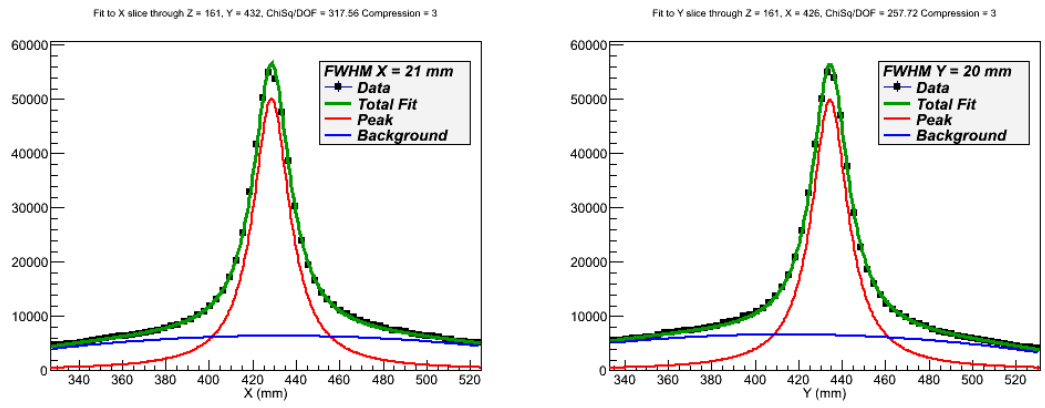

(b) (c)

Figure 5.12: The image produced by gating on 122, 244, 344, 443 and 778keV γ rays from ^{152}Eu is shown in (a) with a 3mm compression. The average FWHM of the image is 20.4mm $\pm$ 1.1mm. (b) and (c) are cross sections through the X and Y axis respectively, showing the Lorentzian fit to the data used to create the image.

but in the wrong area due to their very high angles of scatter.

Imaging at 80keV is especially challenging. The image created is the first seen at this energy level at Liverpool. The very low energy deposit from an 80keV gamma ray will result in a large noise contribution, resulting in a large image resolution. The angle gate applied had to be judged on the amount of data accepted as if a tighter angle gate such as that used for the ^{152}Eu data was applied the number of counts available is to low to produce an image (120 counts in total). By including some of the back scattered events, the position can be seen above the remaining background. The 80keV peak is positioned on a very high Compton continuum, resulting in a large number of

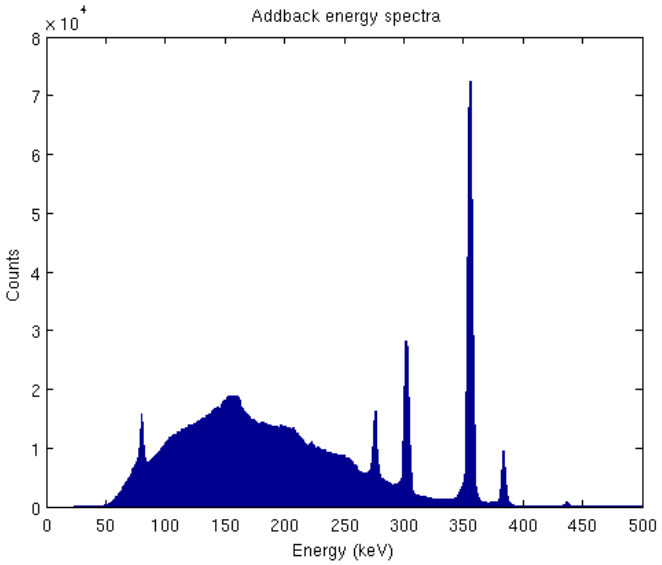

Figure 5.13: Addback energy spectra from a ^{133}Ba source.

Position X (mm)	±	Position Y (mm)	±	FWHM X (mm)	±	FWHM Y (mm)	±
426.2	0.5	434.0	0.5	21.8	0.5	21.8	0.5
Average FWHM (mm)			±	Angular resolution (degrees)			±
21.8			0.4	10.4			0.2

Table 5.5: Position and FWHM of the image from ^{133}Ba taken at Liverpool.

counts which are not fully absorbed within the absorber being used when the image is generated hence the large image resolution. The compression factor has to be set so high to allow the fit to be carried out. This will make the image errors large and also increase the quoted image resolution as two and a half image bins will cover the detector face at this level, the results can be seen in Table 5.6.

The position of the source is reconstructed when energy gating on 80keV and applying the angle gate to within errors of the known position. They also compare favourably to the position found using the combination of 276, 302, 356 and 383keV gamma rays. At 80keV the low statistics results in the use of an abnormally high compression factor to generate an image which can be fitted properly and recognised visually, this large compression factor results in a large uncertainty on the position and also the measurement of the image FWHM.

5.4.3 ^{57}Co

^{57}Co provides two low energy gamma rays, 121 and 136keV, without the presence of any higher energy gamma rays. This allows a low energy image to be produced without the influence of a high Compton continuum. The source used for this purpose

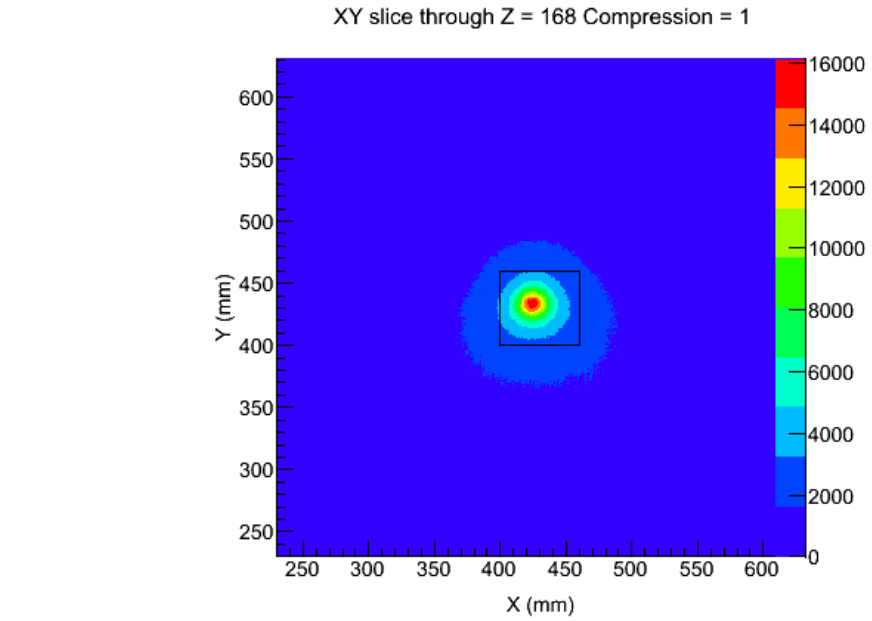

(a)

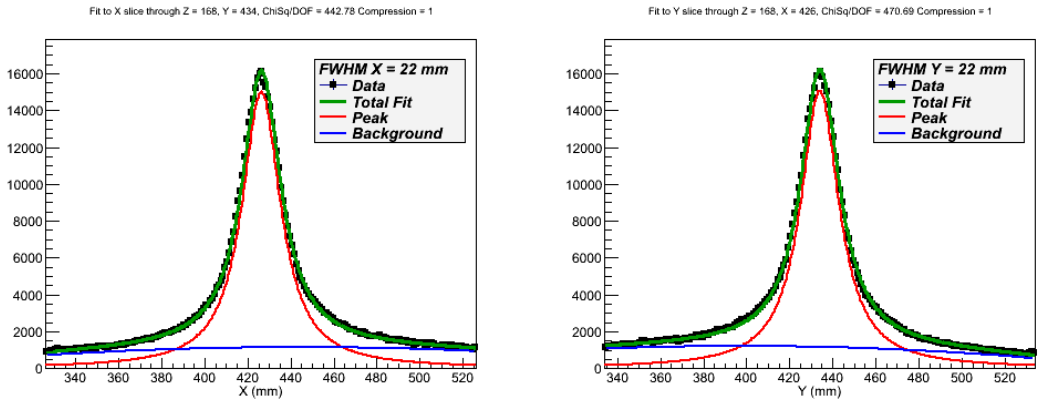

(b) (c)

Figure 5.14: The image produced by gating on 276, 302, 356 and 383keV γ rays from ^{133}Ba is shown in (a) with a 1mm compression. The average FWHM of the image is 21.8mm $\pm$ 0.4mm. (b) and (c) are cross sections through the X and Y axis respectively, showing the Lorentzian fit to the data used to create the image.

at Liverpool is not a true point source, it is a metal screw head with a radius of 2cm, the actual location of the source within this geometry is not known. The addback spectra generated clearly shows both energy peaks and a low Compton continuum though it does contain a number of multiple Compton scattered events below 121keV which do not deposit their full energy within the detector, Figure 5.16. The source was positioned central to the scatterer and at a distance of 9.6cm from the front face of the scatterer.

The initial image produced, Figure 5.17a indicated that the source was not being reconstructed correctly given the size and location of the areas of maximum overlap. To overcome this issue angle gates were placed and altered until an image was visually

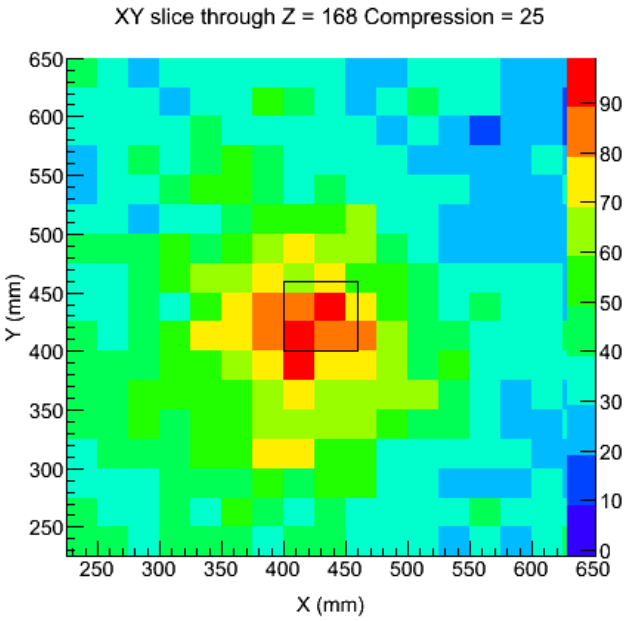

(a)

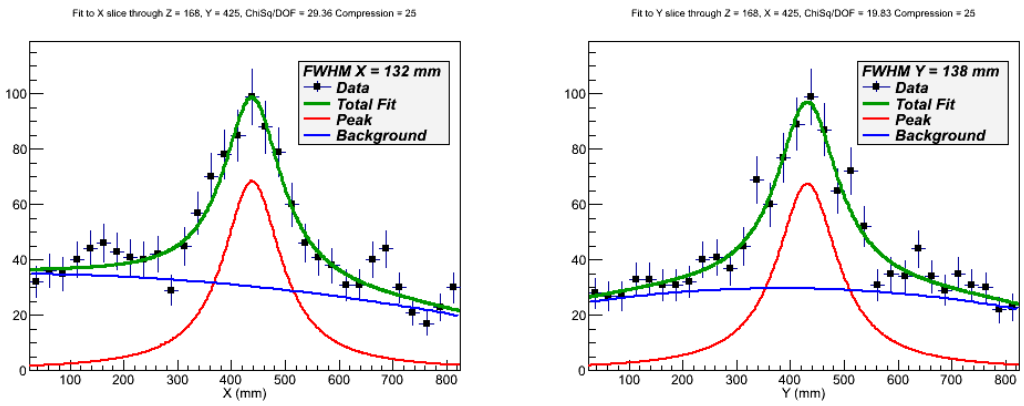

(b) (c)

Figure 5.15: The image produced by gating on the 80keV γ ray from ^{133}Ba is shown in (a) with a 25mm compression. The average FWHM of the image is 135.0mm $\pm$ 21.4mm. (b) and (c) are cross sections through the X and Y axis respectively, showing the Lorentzian fit to the data used to create the image.

identifiable, this reduced the number of cones available for reconstruction so a 3mm compression was used to create the image. An angle gate of 0 to 60 degrees was used as before with the ^{152}Eu source, this tight gate allowed only forward scattered gamma rays to contribute to the image however events that undergo multiple Compton scatters within the energy gate may still contribute to the image, Figure 5.17b. The data reduction from applying the different angle gates can be seen in Table 5.7. Angle gates can also be used to 'clean up' images, giving a better visual result despite the loss of data they introduce.

The quantity of data used to produce the angle gated image is a very small percent-

Position X (mm)	±	Position Y (mm)	±	FWHM X (mm)	±	FWHM Y (mm)	±
438.3	13.85	431.4	13.9	131.8	27.4	138.2	32.93
Average FWHM (mm)			±	Angular resolution (degrees)			±
135.0			21.4	58.7			10.2

Table 5.6: Position and FWHM of the image from ^{133}Ba taken at Liverpool, at 80keV with an angle gate of 0 to 130 degrees.

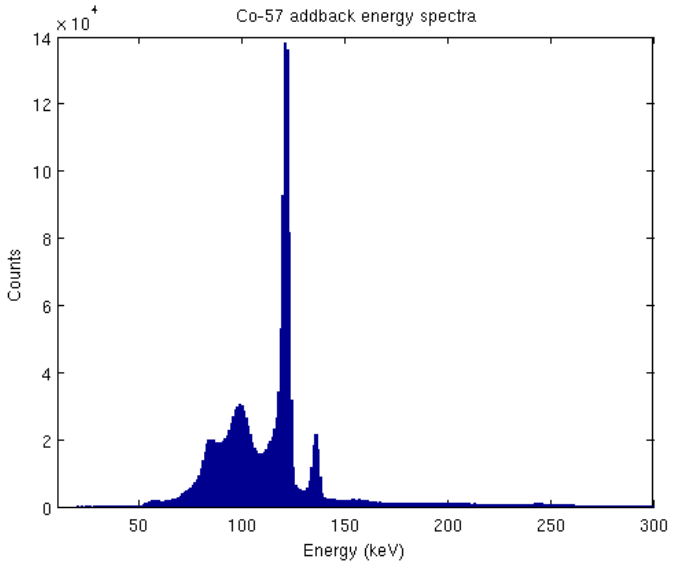

Figure 5.16: Addback energy spectra from a ^{57}Co source.

age of the total data collected that contributes to the 121keV peak. The data would appear to be from back scatters given the very large reduction when an angle gate of 0 to 90 is applied, the additional gates are applied until the image looks sensible, with 60 degrees appearing to provide the best visual image. This angle is around the maximum scatter angle which the gamma ray can Compton scatter into the absorber. The presence of a Compton continuum will also lead to gamma rays which are not fully absorbed contributing to the image.

The angle gated image shows a strange pattern within the background. This may be caused by the absence of some strips in the scatterer alongside the thresholds in the scatterer being set as low as possible. The threshold settings will increase the number of low energy depositions from low angles of scatter that are recorded, these events will have an increased noise contribution causing an increased uncertainty in the cone angle.

Angle gate	Cones available	% of original data available
0 to 180	236475	100.0
0 to 90	70742	29.9
0 to 70	13465	5.7
0 to 60	1938	0.8
90 to 180	165733	70.0

Table 5.7: The effect on the amount of data imaged when an angle gate is applied. The percentage data lost is included.

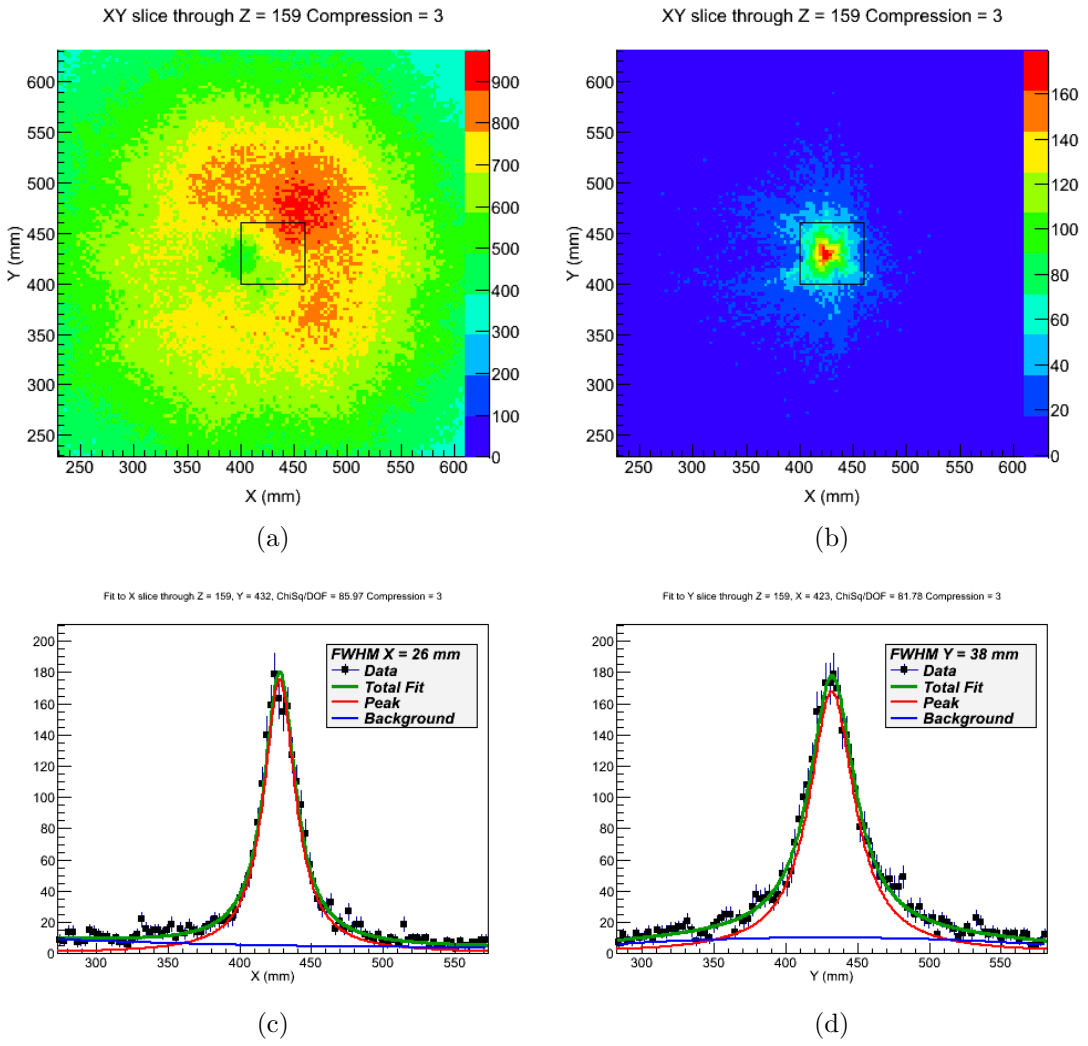

Figure 5.17: The image produced by gating on the 121keV γ ray from ^{57}Co is shown in (a) with a 3mm compression but no angle gate applied. To resolve the source an angle gate of 0 to 60 degrees is applied, this image is shown in (b) with a 3mm compression. The average FWHM of the image is 32.3mm $\pm$ 1.5mm. (c) and (d) are cross sections through the X and Y axis respectively, showing the Lorentzian fit to the data used to create the image (b).

5.5 Distance of source to detector investigation

The ability to find the distance to the source as well as its position in X and Y is required to provide the best possible information on the sources location. The method

Position X (mm)	±	Position Y (mm)	±	FWHM X (mm)	±	FWHM Y (mm)	±
427.9	1.6	432.1	1.6	26.4	1.9	38.2	2.4
Average FWHM (mm)				±			
32.3				1.5			

Table 5.8: Position and FWHM of the image from ^{57}Co taken at Liverpool.

described in Chapter 3 relies upon imaging along a number of slices and finding the minimum image resolution using the FWHM value. In practise this value will provide an underestimate of the position and the values for the FWHM in X and Y will vary due to statistical fluctuations. To try and find a method to correct this underestimate a ^{137}Cs source was placed at four different distances from the scatterer can, 2.5cm to 8.5cm in steps of 2cm (the can is 2.1cm from the front face of the scatterer). The position in X and Y of the source was fixed, with the source mounted on a platform which was moved in Z only, with an error of ± 2mm. The images were then produced across a range of Z slices and the best slice was found from the FWHM value measured in X and Y. Plotting the Z slice against the FWHM value in either X or Y produces a curve, and the minima point can be read off to provide the best Z slice. This method introduces a reading error of ±2mm, example curves can be seen in Figures 5.18b and 5.18c.

The best slice values are then plotted against the distance from the scatterer can and compared to the actual calculated Z slice for this distance. A line of best fit is plotted using the least squares method through the data for FWHM X and FWHM Y seperately producing a straight line for each data series, Figure 5.18a.

This plot indicates that the best Z slice found using the FWHM method follows a linear trend. By finding the gradient m and intercept c of the best Z slice, the best slice found can then be converted into a distance using a simultaneous equation with the measured Z slice as the y value (distance to the detector can is x, in cm) using the equation of a straight line,

$$y = mx + c \tag{5.3}$$

the gradients and intercepts for the lines used here can be found in Table 5.9.

Line	Gradient	Intercept
Actual slice	10.00	98.00
FWHM X best slice	8.00	102.50
FWHM Y best slice	7.95	104.00

Table 5.9: Gradients and intercepts from the fits to the best Z slice versus distance from detector can.

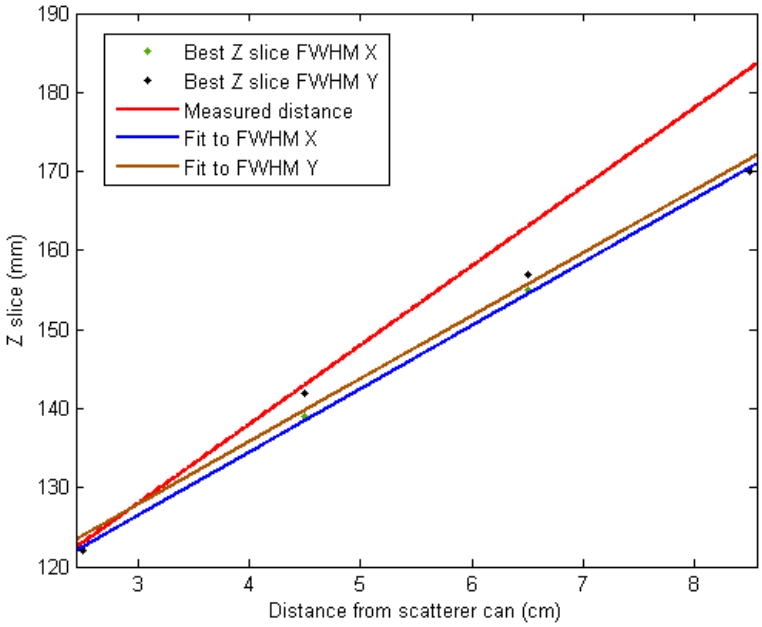

(a)

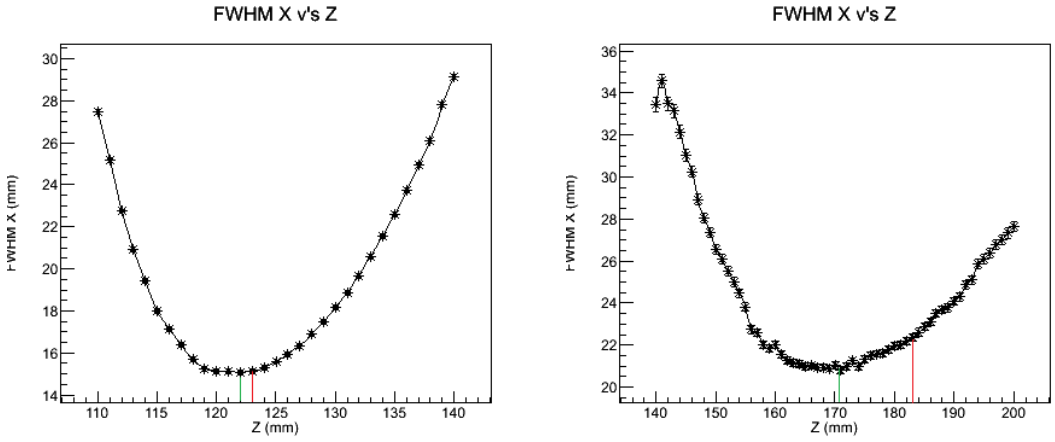

(b) (c)

Figure 5.18: Plot showing fits to the best slice found using the FWHM in X and in Y as previously discussed in Chapter 4.(b) and (c) show two examples of the FWHM in X plotted againt the Z slice imaged. The best slice is taken at the minima of the curve. The actual position is marked in red, where as the best image slice is marked in green.

Using a known distance x the expected best FHWM either in X or Y could be calculated using this method or vice versa. This has only been carried out for a small number of data points and with the detectors at a fixed, very close distance so further investigation is required with larger detector to source distances and different detector geometries to confirm this result.

5.6 ^{22}Na line source

A ^{22}Na line source was imaged using the Compton camera in order to test the imaging code's ability to identify an extended rather than point source. The source is liquid ^{22}Na, contained within a glass cylinder. The cylinder measures 50mm in length and 4mm in diameter, shown in Figure 5.20a and 5.20b, the thickness of the glass is estimated <1mm. By placing the line source parallel to the scatterer, perpendicular to the X (Figure 5.19a) and Y axes (Figure 5.19b, images were produced to check the whether the detector can produce similar images along both axes, Figure 5.20c. The source was positioned 9.1cm from the front face of the scatterer in both cases and perpendicular to the axis being investigated.

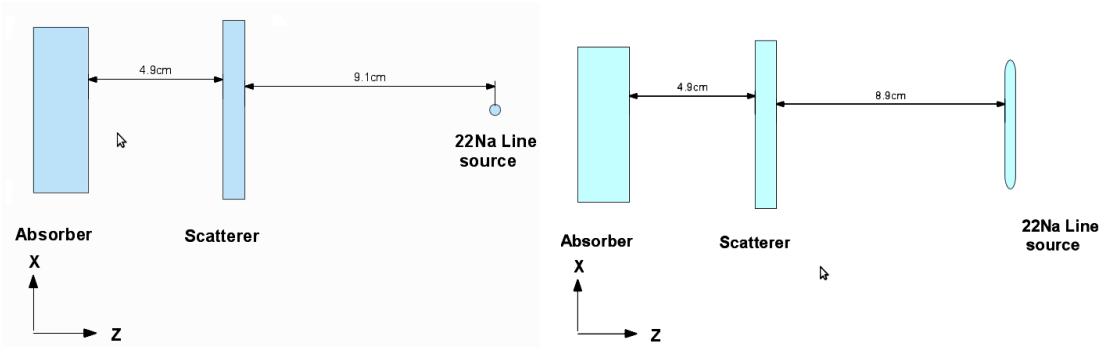

(a) (b)

Figure 5.19: Schematic diagram showing the positions in which the ^{22}Na line source was positioned with relation to the detector crystals along the X and Z axes. (a) shows the source placed perpendicular to the X axes, (b) shows it parallel to X.

In addition the source was then placed perpendicular to the scatterer can, Figure 5.20d, this allowed the FHWM method of finding a best Z slice to be used as a means of checking the length of an extended source placed perpendicular to the detector. The tip of the rod in this orientation is 4cm from the scatterer can and placed centrally.

Images were produced by energy gating on the 511 and 1274keV gamma rays present in the addback spectra, this is shown in Figure 5.21. The images produced for the source placed perpendicular to the Y-axis and perpendicular to the X-axis can be seen in Figures 5.22a 5.23a respectively. A compression factor of 5mm was used to match the statistics available and to provide a good fit to the data.

The information in Table 5.10 shows the FWHM of the images produced in X and Y along with the source position and error estimations on these values. The length of the cylinder is measured within error to the same value when it is placed along either axis indicating that the performance of the detector is not affected by the orientation of the source in comparison to the axis of the detector. The length measured by the Compton camera is 41.6mm $\pm$ 0.7mm taking the average of the two measurements, provides an underestimate for the known source size.

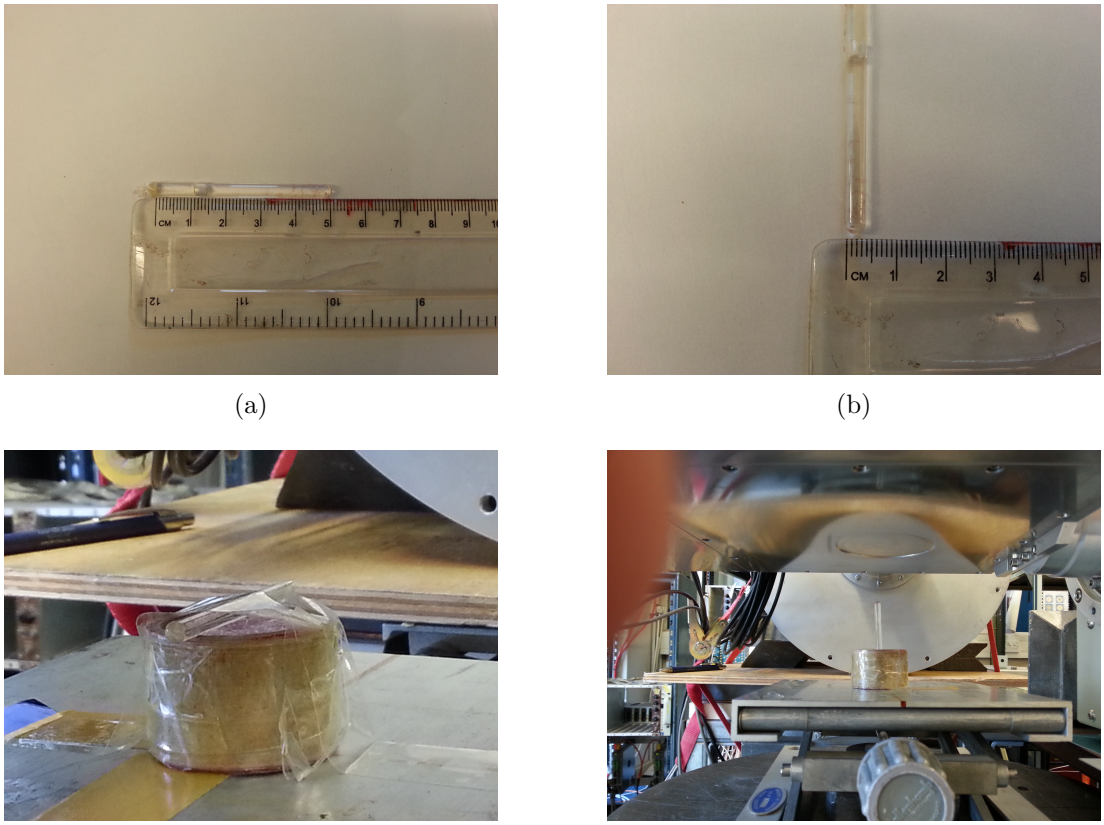

(a) (b)

(c) (d)

Figure 5.20: Pictures of the ^{22}Na source, showing the length (50mm), width (4mm) and the placement in parallel and perpendicular to the detector cans.

The underestimate of the size of the line is due to the fitting method used. The source does not produce a Lorentzian type distribution but more of a flat topped peak when looking along its length. By eye the FWHM of the image is between 47 and 53mm in either diagram depending upon where you set the background level to be. This approximates very well to the actual source size.

5.6.1 Line source perpendicular to detector

Placing the line source perpendicular to the detector cans it was thought the best slice method of finding the distance to a source could be used as a mean of measuring the length of an object. The plots of the best FWHM in X and Y can be seen in Figures 5.24a and 5.24b. The source was placed with a 6.1cm distance between the end of the source and the front face of the scatterer.

Using the distance calibration method the line source should start in Z slice 135 if the FWHM X is used or 136 if FWHM Y is used. The source should stop at 175 (FWHM X) or 176 (FWHM Y). These areas are marked on the diagrams with red lines. The resolution does improve around these area with the minima of the curve within the expected slices, however the minimum FWHM on either curve is 20mm which is

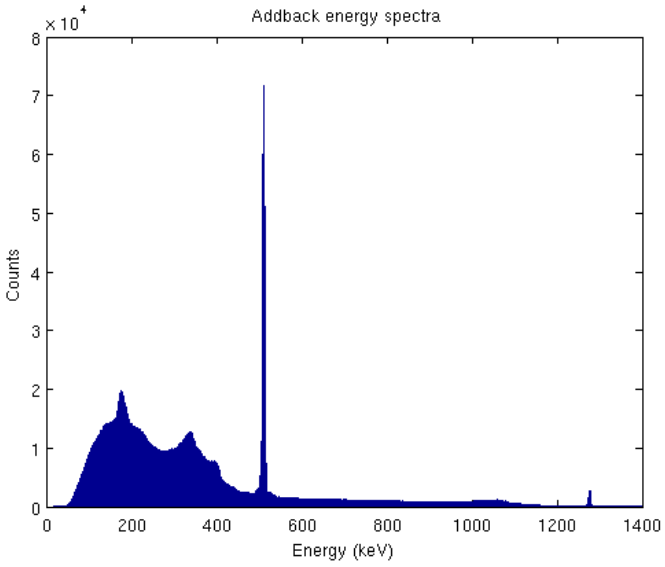

Figure 5.21: Addback energy spectra from a ^{22}Na line source.

Source along axis	Position X (mm)	±	Position Y (mm)	±	FWHM X (mm)	±	FWHM Y (mm)	±
X	429.9	0.5	434.8	0.5	42.3	0.5	20.7	0.5
Y	427.4	0.5	435.0	0.5	22.8	0.5	41.2	0.5

Table 5.10: Position and FWHM of the image from ^{22}Na line source placed along the both axes.

half the width of the line source.

5.7 Scan measurements

The imaging capability of this Compton camera extends to 2π from the centre of the scatterer. As with a standard optical camera the images produced could be subject to distortion the further away from the centreline that the object being imaged is. To investigate whether this effect occurred within our Compton camera system a raster scan was performed across the face of the detector. The raster scan was carried out in 20mm steps with 36 points being used, as shown in Figure 5.25. The scan was performed with two different sources, allowing the use of different energy gamma rays to see if any distortion seen was dependant upon the gamma ray energy incident on the detector system. Both sources were placed at 4.7cm from the front face of the scatterer.

Utilising the scanning table allows the source position to be known accurately (within a 5mm error for placing the source by hand, this error will be constant for each step so the relative error between steps is negligible). By imaging each individual position the reconstructed image position can be compared to the expected values and

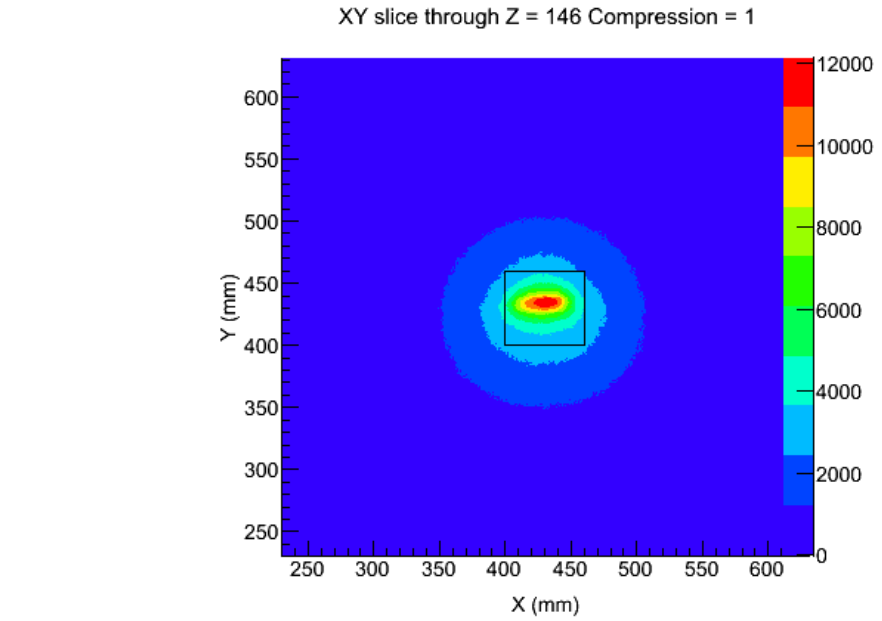

(a)

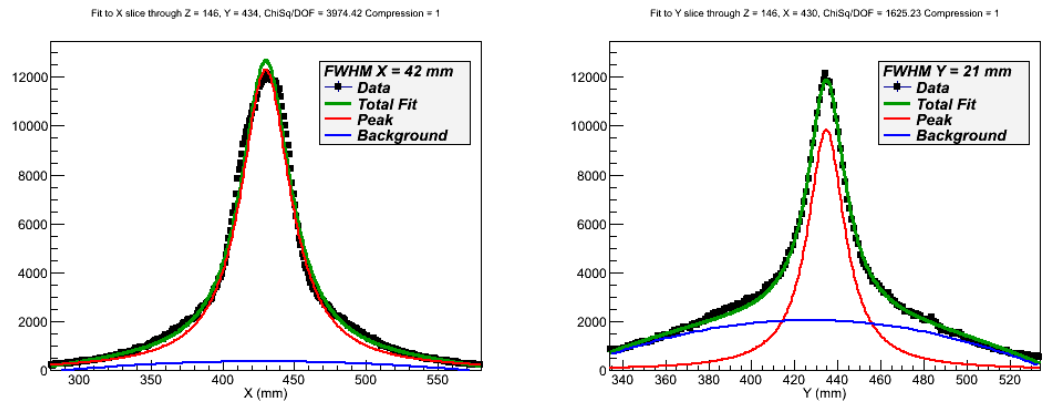

(b) (c)

Figure 5.22: The image produced by gating on 511 and 1274keV is shown in (a) with a 5mm compression. The FWHM in X of the image is 42.0mm ± 0.5mm. (b) and (c) are cross sections through the X and Y axis respectively, showing the Lorentzian fit to the data used to create the image. This image is of a ^{22}Na line source, 50mm long and 4mm wide placed parallel to the detector along the X-axis.

a measure of any distortion can be found. The centreline of the detector system is at 430,430 for the images and quiver plots presented in this section.

5.7.1 ^{137}Cs scan

The first scan carried out used a ^{137}Cs source of 300kBq activity. The source was left in each position for 6000s to provide approximately 10,000 cones in the addback energy spectra when position 1 shown in Figure 5.25 was checked. The count rate measured in Compton mode was 70cps with the source in one corner of the scan.

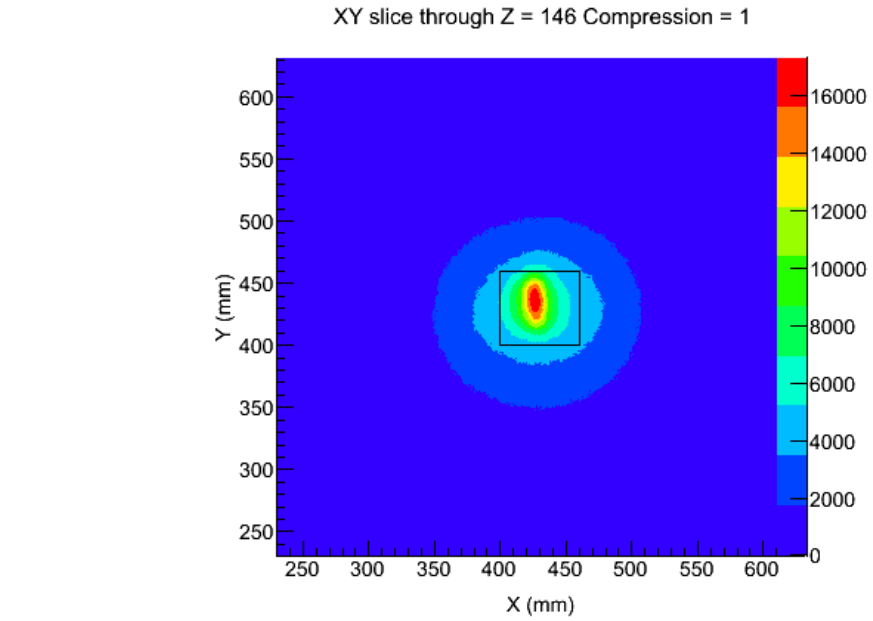

(a)

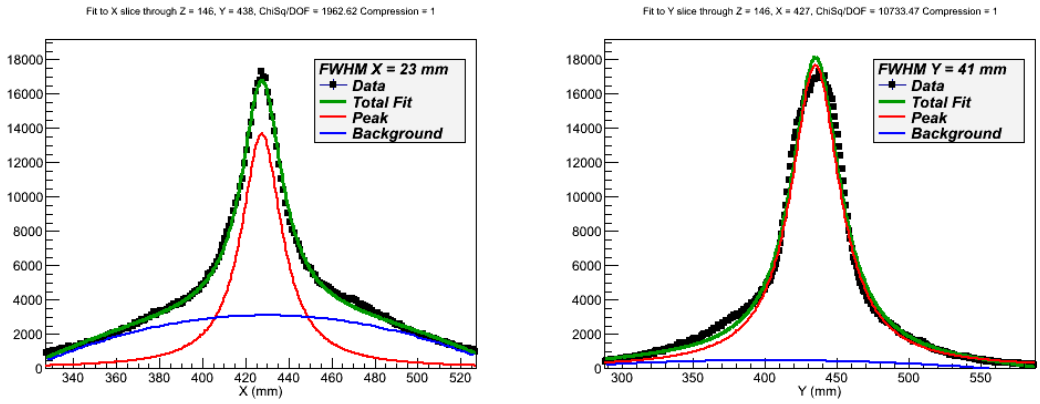

(b) (c)

Figure 5.23: The image produced by gating on 511 and 1274keV is shown in (a) with a 5mm compression. The FWHM in Y of the image is 41.2mm ± 0.5mm. (b) and (c) are cross sections through the X and Y axis respectively, showing the Lorentzian fit to the data used to create the image. This image is of a ^{22}Na line source, 50mm long and 4mm wide placed parallel to the detector along the Y-axis.

The deviation of the reconstructed images position from known positions of the images produced is shown by a quiver plot. This plot indicates the source position (marked as a diamond) and the deviation away from this is point is marked by a vector arrow with magnitude equal to the cross product of the displacement in X and Y. This is shown in Figure 5.26.

The plot indicates that distortion does take place within the Compton camera system, with the reconstructed locations being closer to the detector centreline than expected. This distortion also increases as the source is moved further away from the

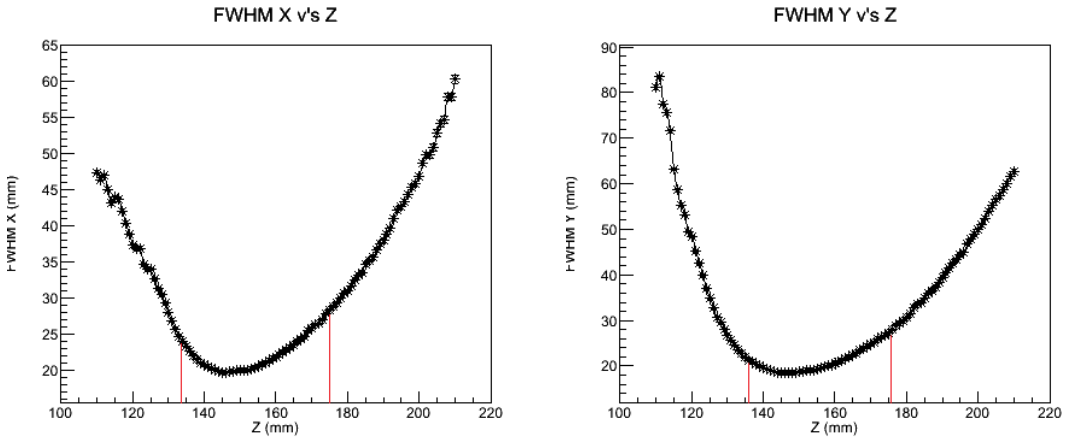

(a) (b)

Figure 5.24: Plots of the FWHM versus Z slice for a ^{22}Na line source arranged perpendicular to the detector cans.

centre. This is similar to a pin cushioning effect seen in optical lenses. The magnitude of the vectors clearly show this trend, with very small magnitudes noticed around the centreline of the detectors. The quiver plot is produced from 2200 cones for each point, this number was chosen as all of the points imaged had this number of cones available for reconstruction.

As the source is moved further away from the centreline there will be a solid angle effect. This reduces the number of gamma rays which will interact with the detector and hence the number of counts seen is reduced. To show this, the number of counts within 2 FWHM of the images produced (using all cones available) for each position is shown in Figure 5.27. This effect is as we would expect. This is also evident if the addback spectra of a central scan position is compared to one of the corner positions, as shown in Figure 5.28.

Plotting the image resolution seen by the Compton camera across the scan points provides an indication of how accurately we can position our source within image space, this is shown in Figure 5.29. The number of cones used for each point has been limited to 2200 to provide a direct comparison. There is a clear indication that as the source moves further away from the centreline the images produced have an increasing FWHM.

This appears to be caused by an asymmetry effect seen in the images, as demonstrated in Figure 5.30a. Here it is clear that images on the edge of the scan tend to spread out towards the centre resulting in an increase in the FWHM.

5.7.2 ^{133}Ba scan

To check if the distortion observed with the ^{137}Cs source was energy dependant a ^{133}Ba source was used. This source was chosen due to to having different gamma ray energies, two of which could be selected, imaged separately and then presented in

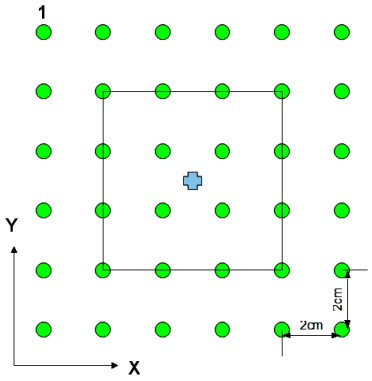

Figure 5.25: Schematic of the 36 positions used for the raster scan. Position 1 is marker, this is the start point and the scanning table moves 2cm in X to the right then steps down 2cm in Y after 6 position and then moves back to the left. Position 1 was used to check the number of counts within the addback spectra that were available, this was used to estimate the time per position. The black square marks the edge of the absorber detector and the cross is the centre of the scatterer and absorber.

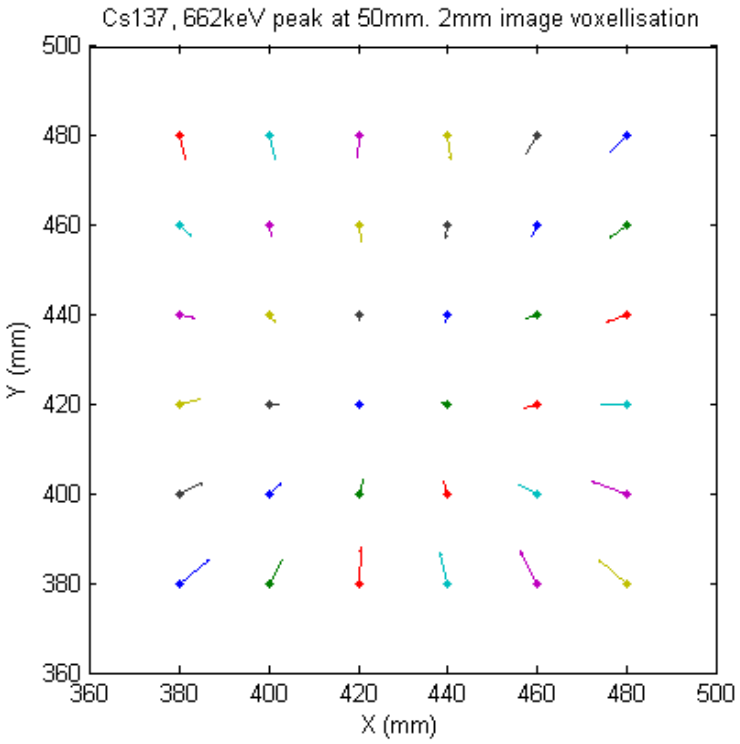

Figure 5.26: Quiver plot showing a 6 by 6 position grid around the face of the scatterer. The detector is centred at 430, 430. Each point has been imaged separately and the deviation from the expected position (marked as a diamond) is shown as a vector arrow, the larger the arrow the greater the deviance. This plot indicates that the images created suffer from greater distortion the further away from the centre they are and is similar to what is seen with an optical camera. Colours are used to differentiate each individual position.

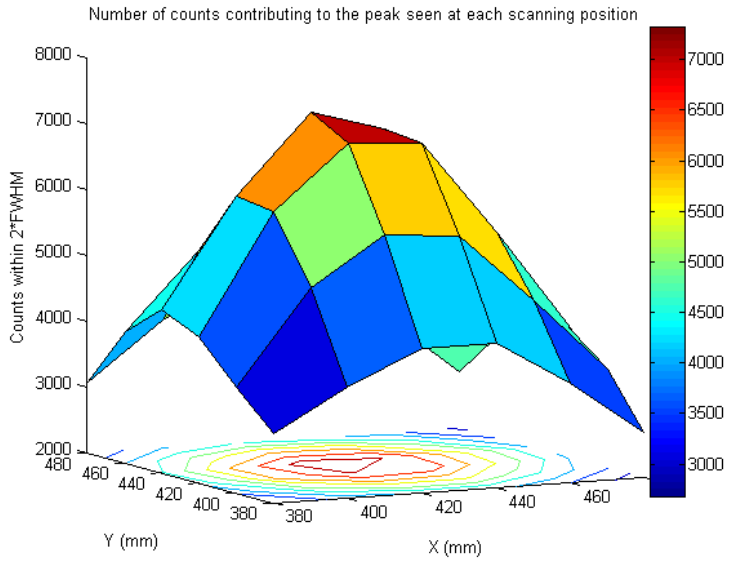

Figure 5.27: Plot showing the number of cones that contribute to making the image for each scan position. This clearly shows a solid angle effect, with fewer cones adding to the image as the source is moved away from the centreline of the detector system (located at 430,430).

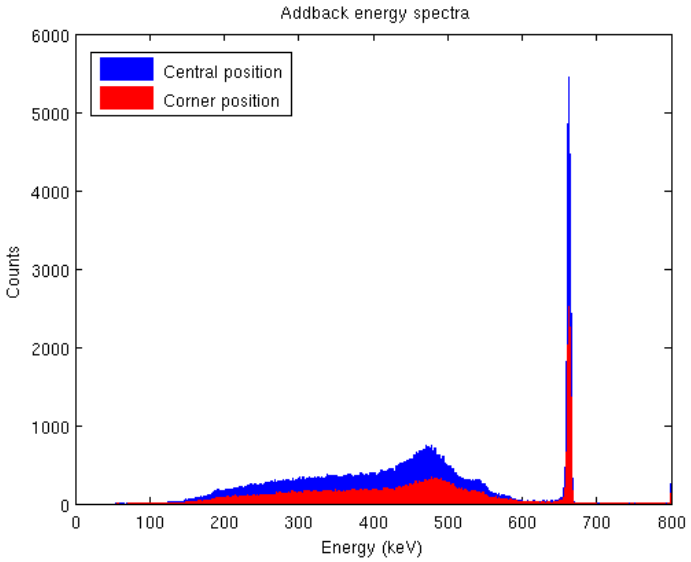

Figure 5.28: Addback energy spectra from the ^{137}Cs scan measurement. Each spectra is generated from a single position to compare the number of events seen at each position. This plot shows a central scan position compared to a corner position, indicating that a solid angle effect reduced the number of events as the source is moved laterally away from the detector centreline.

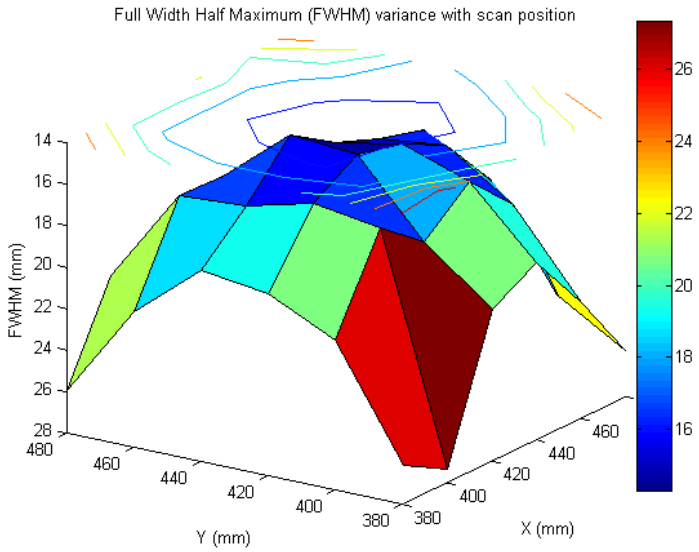

Figure 5.29: Plot showing the image resolution (FWHM) of the images generated for each scan position. This indicates that the FWHM is position related as the smallest FWHM measurements are found near the centerline of the detector (430,430) and get worse as the source is moved further away. This plot is generated from images created using the same number of cones per scan position.

a quiver plot. The source was 110kBq in activity and the 356keV peak was found to contain around 10,000 counts after 10800 seconds. The total count rate from the source in Compton mode was 50cps with the source at a corner position. The energies chosen for comparison are 276 and 356keV, (quiver plots shown in Figures 5.31a and 5.31b) with the number of cones used for reconstruction limited to 2200 providing a direct comparison to the ^{137}Cs scan.

The effect appears to be independent of energy as the trend of further away points being reconstructed closer to the centreline is maintained. The size of the arrows indicates that although the imaging code used 2200 cones to generate each image, not all of these contribute and hence we have slightly different sizes of vectors due to the number of cones in each image. The solid angle effect is also still evident, shown by the addback spectra in Figure 5.32.

5.8 Multiple sources

The ability of the Compton camera to identify different sources of radiation within an object and to be able to separately image them was tested. Two ^{137}Cs sources were placed inside a plastic box, each with a different activity. These sources were placed to either side of an aluminimum square, ontop of which either a ^{60}Co or a ^{133}Ba was positioned. These sources were chosen to test the Compton cameras ability to separate sources above a Compton background caused by higher energy peaks (^{133}Ba) and also

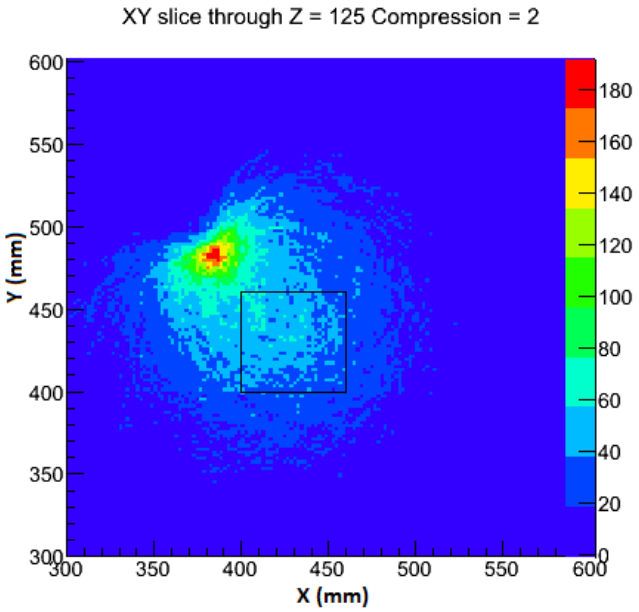

(a)

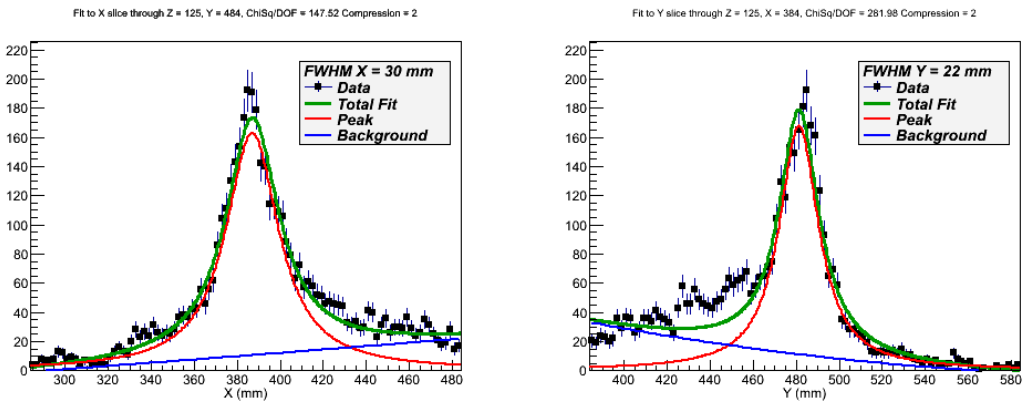

(b) (c)

Figure 5.30: The image produced for the ^{137}Cs scan at position one in Figure 5.25. The image (a) clearly shows an asymmetry with the reconstructed image spreading towards the centre of the detector. (b) and (c) are cross sections through the X and Y axis respectively, showing the Lorentzian fit to the data used to create the image.

to be able to identify different sources across the operating energy range (^{60}Co). The sources were also arranged at different heights within the box, enabling the Compton cameras ability to separate sources by their distance to be tested. The layout and pictures of the setup can be found in Figure 5.33.

The ^{137}Cs sources used had different activities, the lefthand source was 300kBq while the righthand source was 200kBq.

The images presented for the different sources will be on the best z-slice found by gating on the sources gamma ray energies, found by using the method detailed previously. The best slice will provide an estimate of the position and the relative

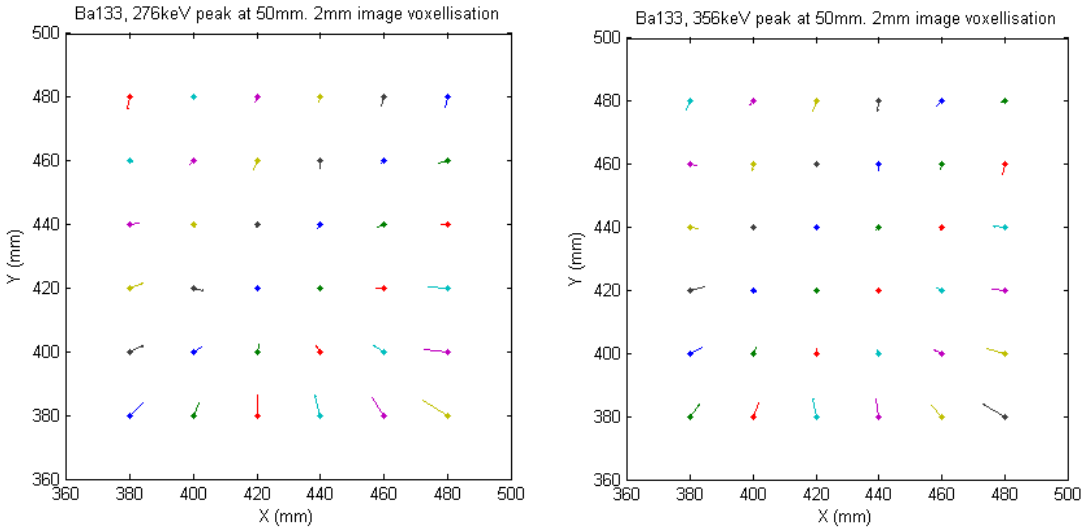

(a) (b)

Figure 5.31: Quiver plots for the ^{133}Ba scan. This scan was carried out to check the energy dependence of the distortion seen in the ^{137}Cs scan. The arrows tend to point in the same directions, indicating that the effect is energy independent and is due to the Compton camera system itself. The same pin cushioning effect as seen with ^{137}Cs is seen.

separation in Z for the different sources.

5.8.1 ^{137}Cs and ^{60}Co

To test the cameras ability to identify a very low activity source in the presence of more active sources a ^{60}Co source was used. This source was 70kBq in activity and provides two gamma rays above the Compton continuum of ^{137}Cs at 1173 and 1332keV.

Looking at the addback energy spectra, Figure 5.34a both peaks from ^{60}Co are clearly visible. Applying energy gates for all three photopeaks present in the addback spectra produces the image seen in Figure 5.34b which indicates only the presence of two sources. By gating on the energies from each source individually the sources can be separated. The image in Figure 5.35a shows the ^{60}Co source, this is energy gated on 1173 and 1332keV when compared to the ungated image this source is in a position between the two obvious sources identified previously.

By applying and energy gate to the 662keV photopeak, the ^{137}Cs sources can be imaged. This is seen in Figure 5.36a and clearly shows two individual, well separated source. This image also shows that the lefthand peak in the cut along the X axis is larger in size than the one to the right. This is an indication that the source activity on the left is more than that on the right.

The separations between each source relative to another is shown in Table 5.11. This compares favourably to the 36.00mm separation between the two ^{137}Cs sources with

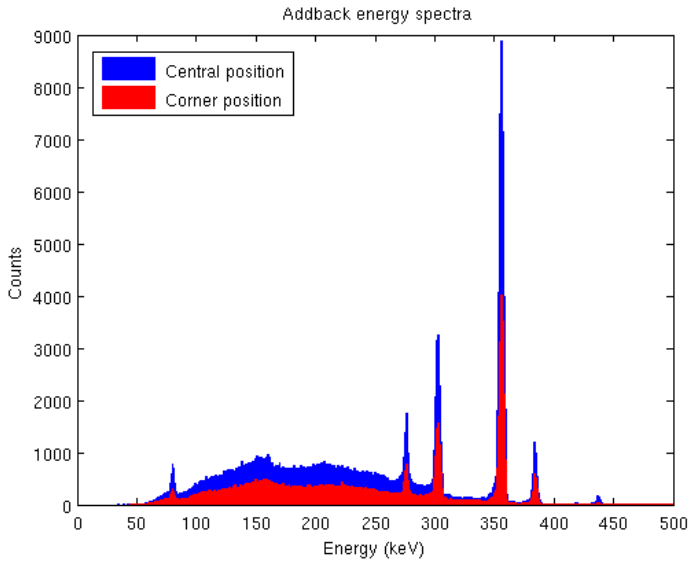

Figure 5.32: Addback energy spectra from the ^{133}Ba scan measurement. Each spectra is generated from a single position to compare the number of events seen at each position. This plot shows a central scan position compared to a corner position, indicating that a solid angle effect reduced the number of events as the source is moved laterally away from the detector centreline.

Source 1	Source 2	Separation in X (mm)	±	Actual value (mm)
^{137}Cs left	^{137}Cs right	33.82	0.72	36.00
^{60}Co	^{137}Cs left	16.60	0.72	18.00
^{60}Co	^{137}Cs right	17.22	0.72	18.00

Table 5.11: This table shows the relative separation in X between the three different sources, two ^{137}Cs and one ^{60}Co as measured by the Compton camera.

the ^{60}Co source placed centrally between them. The image distortion seen previously will play a part in the seperation measured from the reconstruction. As the box has been mistakenly placed slightly higher than expected, there will be a estimated ±2mm error in the relative position for each source. The relative separation in z also compares favourably as seen in Table 5.12.

^{137}Cs Best Z slice	^{60}Co Best Z slice	Separation (mm)	±	Actual value (mm)
187	156	31	7	24

Table 5.12: This table shows the relative separation in Z between the three different sources, two ^{137}Cs and one ^{60}Co as measured by the Compton camera.

5.8.2 ^{137}Cs and ^{133}Ba

Replacing the ^{60}Co source with a ^{133}Ba source the ability to identify a source above the Compton continuum of another source is tested. The energy peaks for ^{133}Ba all occur below those seen for ^{137}Cs at 662keV. The addback energy spectra in Figure 5.37a clearly shows the ^{133}Ba photopeaks along with the 662keV peaks from ^{137}Cs with the barium peaks being above the Compton continuum of the caesium. By applying energy gates across all the available photopeaks, Figure 5.37b, the different sources appear to be merging into one extended source, similar to the ^{22}Na source used previously. This is due to the ^{133}Ba and ^{137}Cs sources having similar activities, with the ^{133}Ba source having an activity of 270kBq.

The images produced by energy gating on each source can be found in Figure 5.38.

Source 1	Source 2	Separation in X (mm)	±	Actual value (mm)
^{137}Cs left	^{137}Cs right	32.79	0.71	36.00
^{133}Ba	^{137}Cs left	15.40	0.71	18.00
^{133}Ba	^{137}Cs right	17.39	0.71	18.00

Table 5.13: This table shows the relative separation in X between the three different sources, two ^{137}Cs and one ^{133}Ba as measured by the Compton camera.

By applying energy gates to the peaks associated with each source as previously done the sources can be separated. The separations between each source relative to another is shown in Table 5.13. This compares favourably to the 36.00mm separation between the two ^{137}Cs sources with the ^{133}Ba source placed centrally between them. The distance in Z is also reproduced within error margins, shown in Table 5.14.

^{137}Cs Best Z slice	^{133}Ba Best Z slice	Separation (mm)	±	Actual value (mm)
185	162	23	7	24

Table 5.14: This table shows the relative separation in Z between the three different sources, two ^{137}Cs and one ^{133}Ba as measured by the Compton camera.

The source seperation is again an underestimate, this indicates that the image disparity is a factor with these measurements as the boxes were not quite central when measured in Y. The shift that the disparity would apply accounts for the differences seen, within the error margins of the images.

5.9 Summary

The results of this chapter are summarised in the following tables, one showing the Compton cameras ability to locate a source to the expected position, Table 5.15, the other showing the quality of the image produced, Table 5.16.

Source	γ ray Energy (keV)	Expected X (mm)	Expected Y (mm)	Measured X (mm)	$\pm$	Measured Y (mm)	$\pm$	Compression
^{57}Co	121	430	430	427.9	1.6	432.1	1.6	3
^{152}Eu	122	430	430	427.7	2.6	433.8	2.7	5
^{152}Eu	244	430	430	428.8	1.5	434.1	1.5	3
^{152}Eu	344	430	430	428.5	1.5	434.3	1.5	3
^{152}Eu	443	430	430	428.5	1.5	434.5	1.5	3
^{152}Eu	778	430	430	428.5	1.5	434.8	1.5	3
^{152}Eu	964	430	430	428.8	1.5	434.7	1.5	3
^{152}Eu	1112	430	430	428.5	1.5	434.1	1.5	3
^{152}Eu	1408	430	430	428.2	1.5	434.3	1.5	3
^{152}Eu	122 - 964	430	430	428.6	1.5	434.3	1.5	3
^{133}Ba	276 - 383	430	430	426.2	0.5	434.0	0.5	1

Table 5.15: Summary table showing the measured position of the source compared to the expected position for the Liverpool data. The expected positions have an error of $\pm$ 5mm.

The Compton camera has shown its ability to images from 80keV to 1408keV, covering the energies of interest. Imaging at low energy has been shown to be difficult due to the presence of events which add into the addback spectra but are not usable for imaging, whether they are back scattered events or part of the Compton continuum of a higher energy gamma ray.

Extended sources have been investigated, with the images produced being visibly different to those seen for a point source at a comparable distance. The FWHM measurement of an extended source will provide an indication of its size however this is not an accurate means of measuring the source given that the FWHM measured with the back projection code used here appears to provide an over estimate. The back projection method used lends itself to location point sources as it is looking for a single pixel in which we have the maximum number of overlapping cones, when this area of overlap becomes more diffuse due to the source being extended the imaging code used here becomes less reliable. To solve this issue an iterative approach could be applied however this has not been carried out for this piece of work.

The ability of the Compton camera to identify different radionuclides present in one object using the addback energy spectra was tested and shown to work, including the ability to clearly separate the sources positions in X along with the ability to identify differences in distance from the detector as well. The extended source measurement indicate that this would also work along the Y-axis.

Source	γ ray Energy (keV)	Average FWHM (mm)	$\pm$	Angular resolution (degrees)	$\pm$	Compression
^{57}Co	121	32.3	1.5			3
^{152}Eu	122	21.7	2.9	10.4	1.4	5
^{152}Eu	244	21.7	1.1	10.3	0.5	3
^{152}Eu	344	20.4	1.1	9.7	0.5	3
^{152}Eu	443	17.0	1.1	8.1	0.5	3
^{152}Eu	778	19.5	1.1	9.3	0.5	3
^{152}Eu	964	18.6	1.1	8.9	0.5	3
^{152}Eu	1112	19.6	1.1	9.3	0.5	3
^{152}Eu	1408	16.7	1.1	8.0	0.5	3
^{152}Eu	122 - 964	20.4	1.1	9.72	0.5	3
^{133}Ba	276 - 383	21.8	0.4	10.4	0.1	1

Table 5.16: Summary table showing the average FWHM and angular resolution for the Liverpool data.

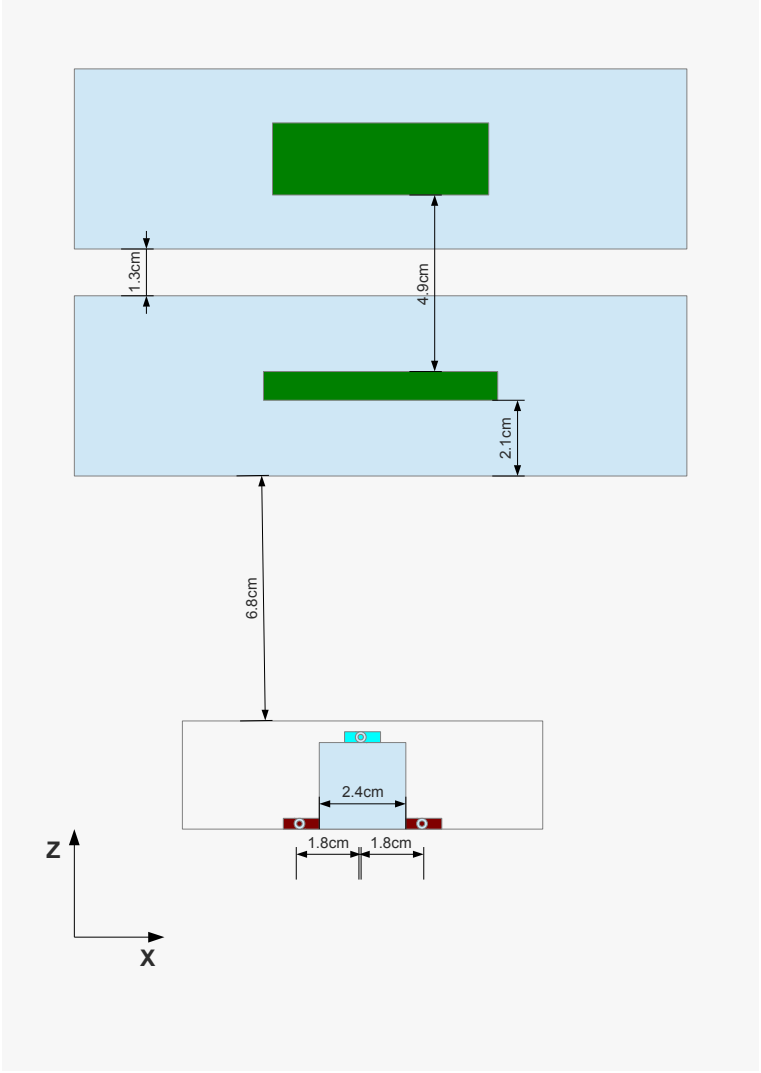

(a)

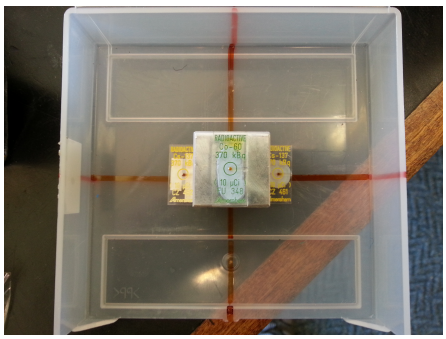

(b)

(c)

Figure 5.33: Schematic diagram of the box layout used, (a). The box contains two ^{137}Cs point sources contained within glass slides, marked in red and another point source contained within a glass slide, either ^{60}Co or ^{133}Ba marked in cyan. The pictures in (b) and (c) show the actual layout utilising a plastic box with a thin copper sheet used to absorb low energy X-rays when the ^{133}Ba source is used.

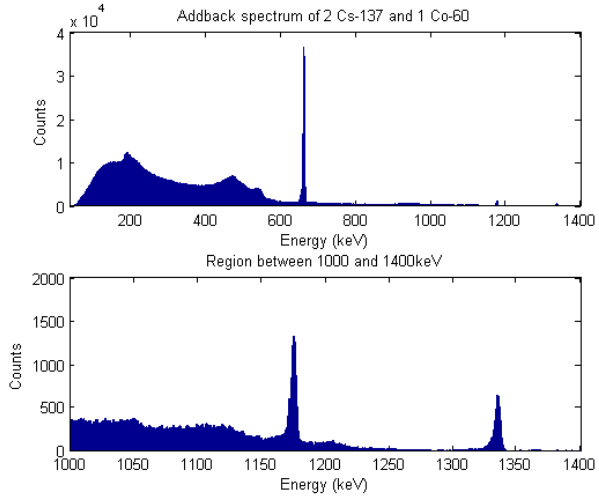

(a)

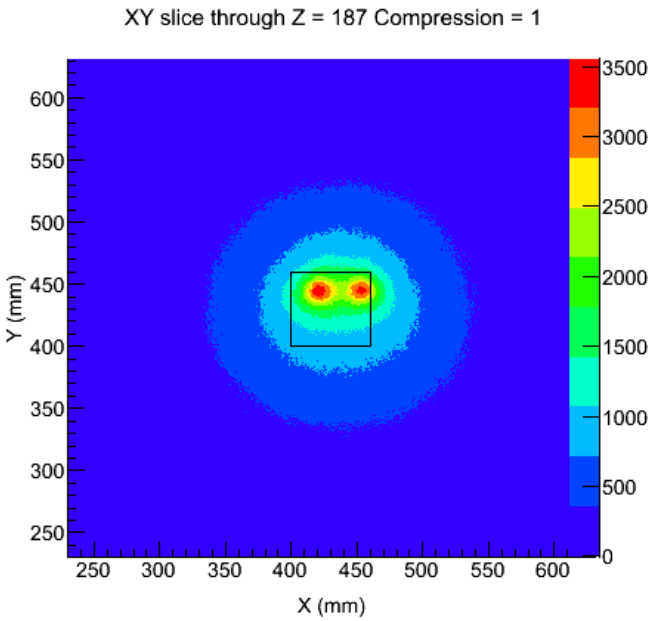

(b)

Figure 5.34: (a) shows the addback energy spectra from three sources, one ^{60}Co and two ^{137}Cs. The sources were placed in a box. The addback spectra clearly indicates the presence of both radio isotopes. The close up section is shown to indicate the two photopeaks (1173 and 1332keV) from the ^{60}Co source more clearly. (b) shows the image produced when energy gates are applied to all three photopeaks evident in the addback spectra.

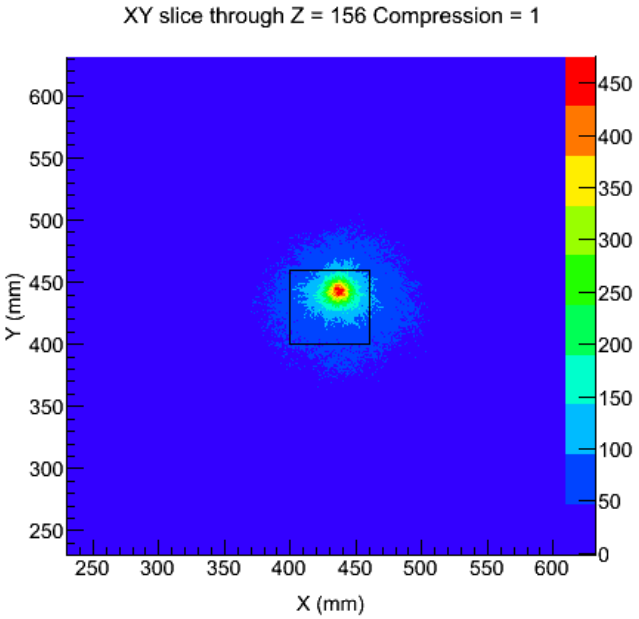

(a)

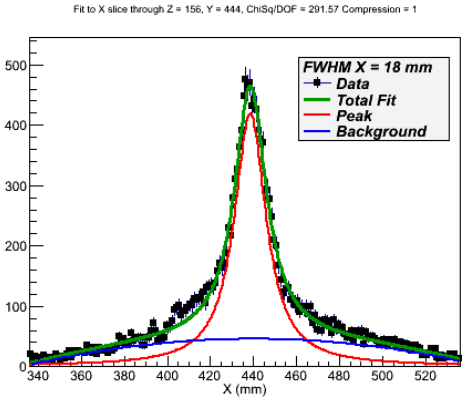

(b)

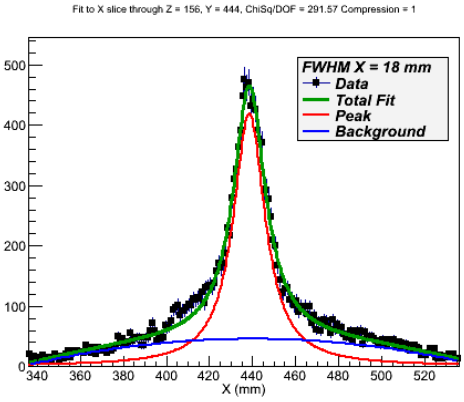

(c)

Figure 5.35: The image produced by gating on 1173 and 1332keV, this image gives the location of the ^{60}Co source. (b) and (c) are cross sections through the X and Y axis respectively, showing the Lorentzian fit to the data used to create the image.

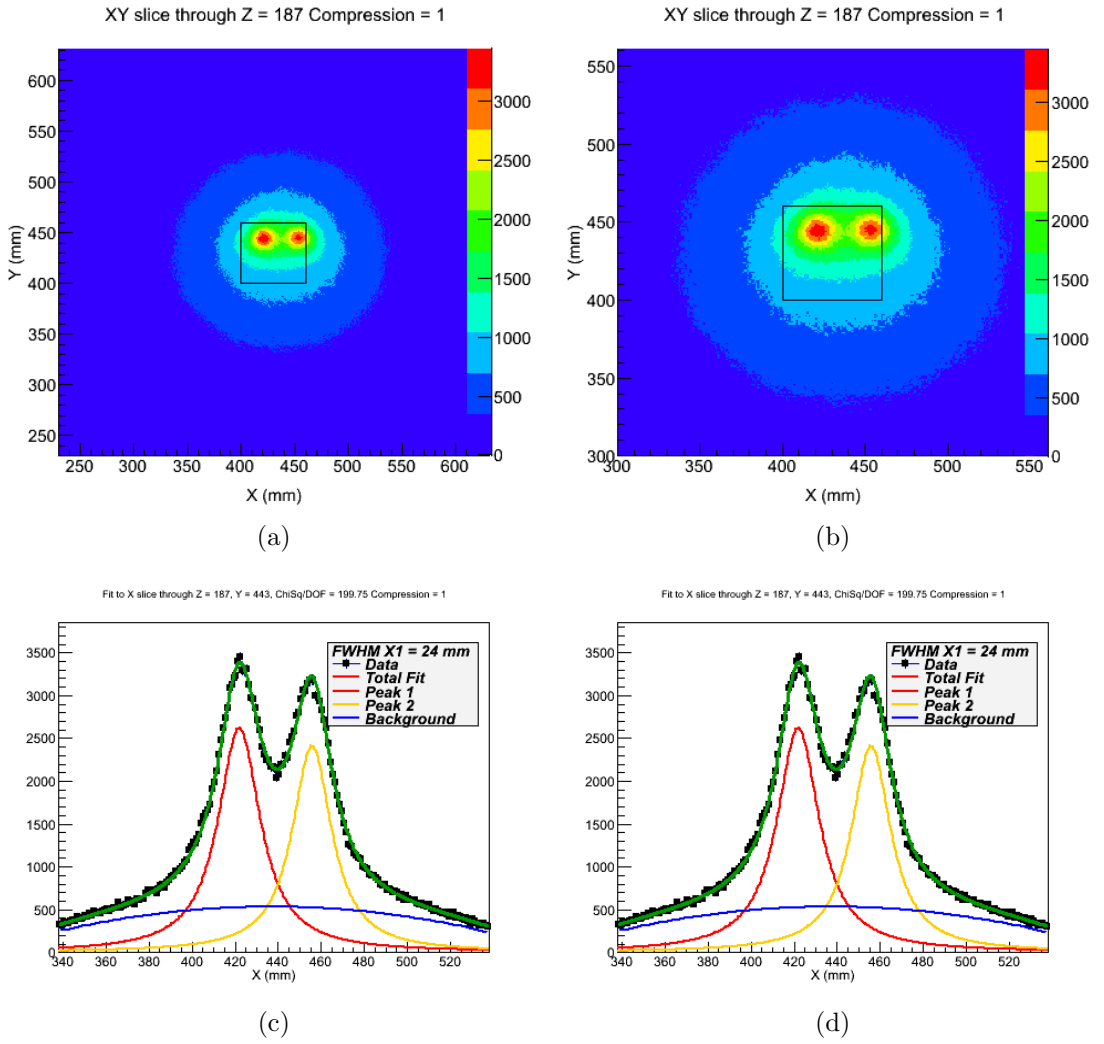

Figure 5.36: The image produced by gating on 662keV (a), this image gives the locations of the two ^{137}Cs sources with a zoomed view shown in (b). The sources are well defined and separated, with the size of the peaks seen in (c) giving an indication that the left hand source is more active than that on the right due to the increased number of counts. (c) and (d) are cross sections through the X and Y axis respectively, showing the Lorentzian fit to the data used to create the image.

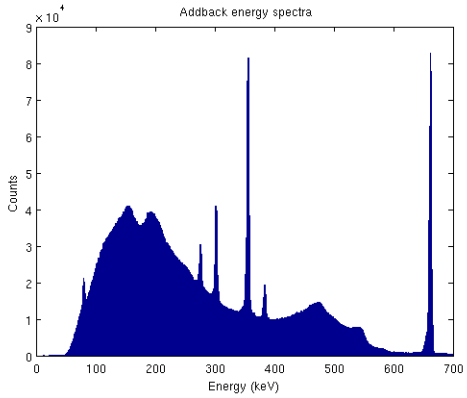

(a)

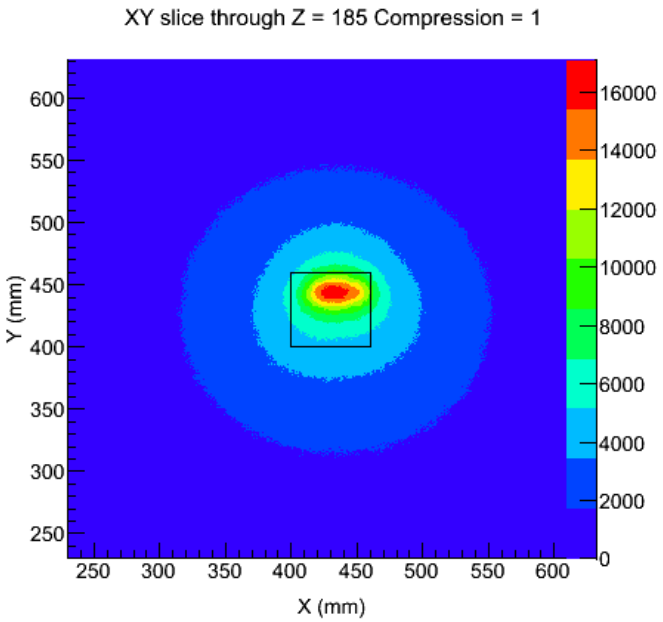

(b)

Figure 5.37: (a) shows the addback energy spectra from three sources, one ^{133}Ba and two ^{137}Cs. The sources were placed in a box. The addback spectra clearly indicates the presence of both radio isotopes. (b) shows the image produced when energy gates are applied to all the photopeaks evident in the addback spectra.

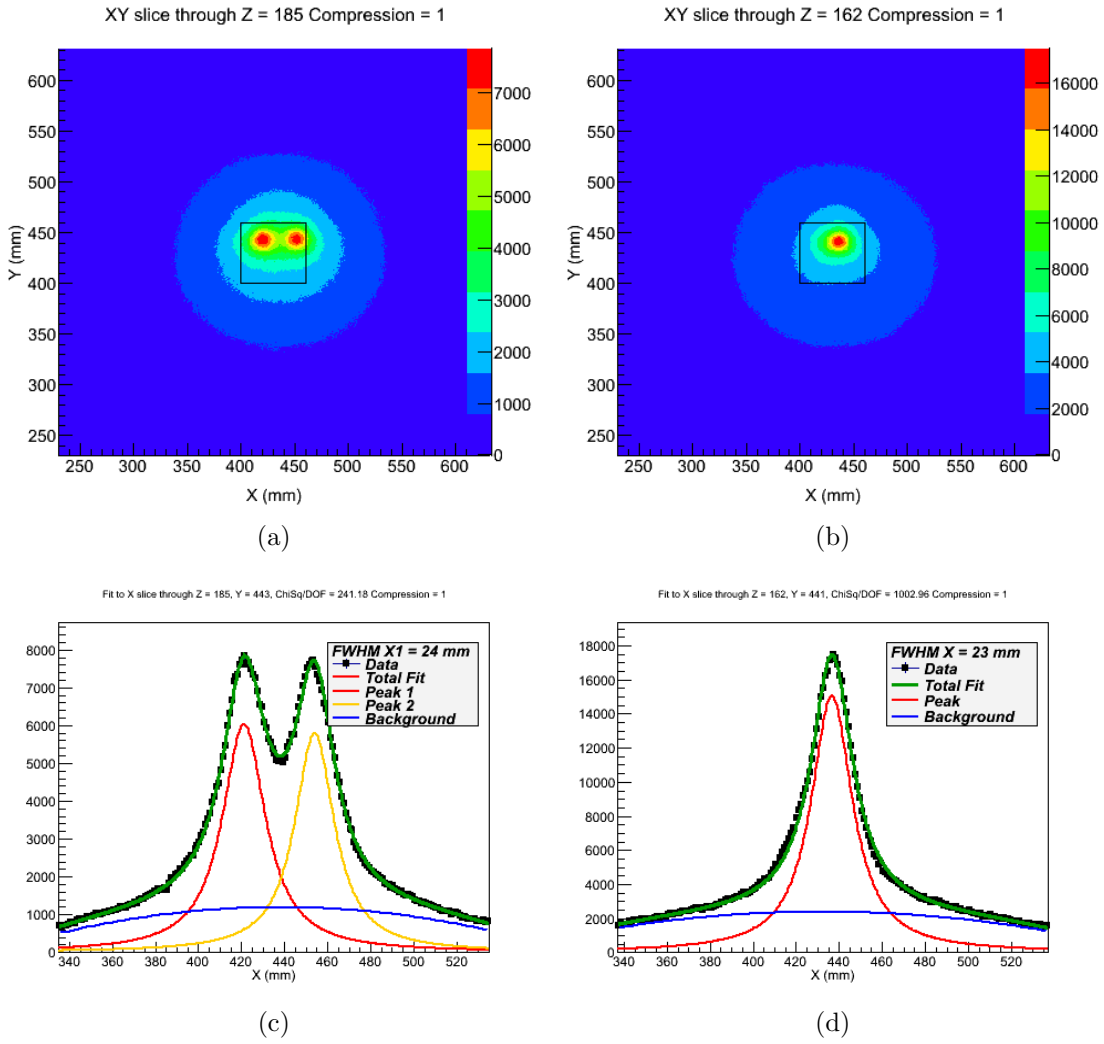

Figure 5.38: The image produced by gating on ^{137}Cs (a) and (c), or on ^{133}Ba (b) and (d). These images show that the sources are well defined and seperated. The size of the peaks seen in (c) giving an indication that the left hand ^{137}Cs source is more active than that on the right due to the increased number of counts. (c) and (d) are cross sections through the X and Y axis respectively, showing the Lorentzian fit to the data used to create the image.

Chapter 6

Experimental results from Aldermaston

Initial testing of the Compton camera was carried out at AWE Aldermaston before the investigations carried out in the previous chapter. Tests were carried out to determine if the detectors would work in Compton camera mode using the new digital DAQ, the energy range of the Compton camera across which images could be produced and also whether images could be produced from this data. The results from these initial tests will be presented in this chapter. The tests also enabled the AWE personnel to become accustomed to using research grade detectors alongside the new digital electronics. AWE Aldermaston have access to laboratory samples containing SNM material, in particular ^{235}U and ^{239}Pu which were made available for the tests, along with more commonly available sources. Emphasis was placed on the lower energy gamma-ray sources. Access to the sources and laboratory used at Aldermaston was restricted. Data could only be collected during the working hours of the laboratory, no overnight data collection was possible limiting the time available to make measurements and setup the system.

Due to time constraints the energy thresholds were set to an arbitrary level within the V1724, using a single channel from each detector. The value chosen allowed the 32.2keV X-ray from ^{137}Cs to be visible in the absorber and the value used for the scatterer was just above the noise at 9keV. The value put into the system is not an energy, but an arbitrary number so this resulted in the threshold energies being different across all channels and with some being set to a level below the noise. Additional settings within the V1724 controls were not fully understood at the time so were set incorrectly, resulting in very high count rates being measured, 2000+ counts per second (cps) in Compton mode as opposed to around 70cps with sources at similar distances and activities when the detectors were used at Liverpool. In singles mode the rates exceeded 20000cps at Aldermaston resulting in the DAQ system crashing due to the high through put of data.

6.1 Detector setup

The detectors were mounted on a purpose built frame designed to enable the detectors to be repositioned easily while holding the detectors parallel to one another, Figure 6.1. Detector separation was set to 5.1cm crystal-to-crystal, Figure 6.2. This distance was chosen to provide a good solid angle coverage between the scatterer and absorber, while maintaining enough of a gap that any vibrations caused by the Cryo-Pulse 5 unit were minimised. As the detectors are moved further apart the image resolution will improve due to the placement of the cone axis having less errors, however the data collection rate will decrease due to the smaller solid angle coverage between the two detectors. The absorber detector is sensitive to microphonic noise so the vibrations caused by the Cryo-Pulse unit may have increased the noise levels seen in the detector. For the work at Aldermaston the 10x gain GO Box was used, this GO Box was manufactured by AWE using the circuit diagrams provided by Liverpool University and was the only version available for these tests.

The time coincidence window was set to 75ns for the work at Aldermaston. This was a figure that was assumed would allow the system to collect good quality data as the trigger window was set to such a small value. The information later gained at Liverpool regarding the time resolution between the detectors shows that the data collected here is only a small fraction of the actual data, with the events occurring out-with the trigger window being lost.

6.2 Measurements taken at Aldermaston

Three point sources were provided for measurement, alongside two discs containing SNM materials. The sources were mounted on a lab stand within a large plastic holder. This arrangement was positioned by eye, within ± 30mm in x,y and z. The exact activities of the sources provided varied between the databases and information sheets available so no calculation of efficiency was possible however the energy range of the Compton camera could be tested.

6.2.1 Calibration

Calibration of the Si(Li) detector at Aldermaston was carried out using a ^{152}Eu source, using the 45.8keV X-ray and the 121.8keV gamma ray. A simple two point linear calibration was carried out as no peaks higher in energy than 122keV were visible running the detector in singles mode. The lack of any higher energy peaks is due to the probability of gamma rays higher in energy undergoing photoelectric absorption being very low while the Compton scattering from the higher energy peaks is much more likely resulting in only a Compton continuum being observed above 122keV. The HPGe detector was calibrated using the same source, performing a quadratic calibration

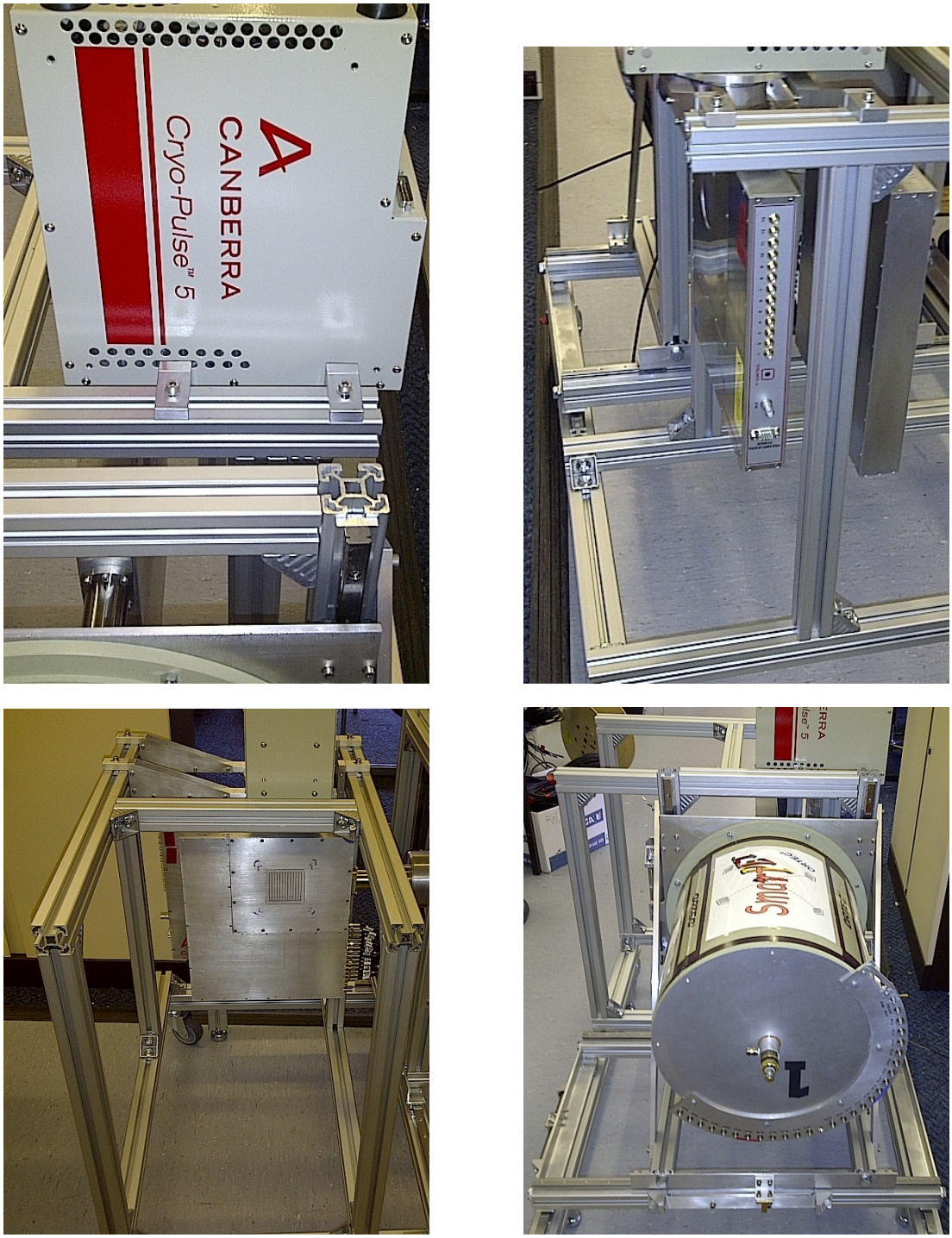

Figure 6.1: Pictures of the frame designed to mount the Compton camera system for work at Aldermaston. The frame is made from aluminium cross section and mounted on wheels to enable the detectors to be moved easily. The mounting positions are designed to hold the detectors parallel to one another with the detectors aligned co-linearly.

using the 121.8, 244.7, 344.3, 778.9 and 964.1keV peaks.

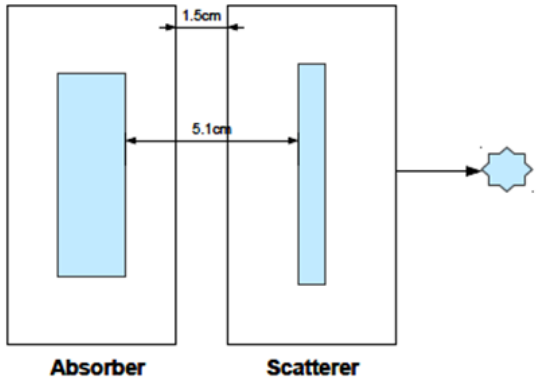

Figure 6.2: Schematic diagram of the detector setup at Aldermaston, showing the detector separation (1.5cm can to can) and the placement of the source at a distance D from the housing can of the scatterer.

6.2.2 Point source measurements

Point sources were used to test the energy range of the Compton camera. The addback spectra and also the images produced will be presented for three different sources. The details for each data run are listed in Table 6.1, this includes the radioisotope, source configuration, data collection time, distance from the scatterer housing can and also if the source was positioned with an offset or in line with the centre of the detectors.

Radioisotope	Source configuration	Collection time (hours)	Distance to scatterer crystal (cm)	Central/Offset (cm)
^{57}Co	Point	4.8	8.1	Central
^{152}Eu	Point	4.4	7.9	Central
^{152}Eu Cu shielded	Point	4.2	8.3	Central
^{133}Ba	Point	5	8.6	Offset +1 in Y
^{235}U	2.5cm diameter disc	5.0	7.1	Central
^{239}Pu	4.5cm diameter disc	4.8	11.1	-1 offset in Y

Table 6.1: This table shows the details of all the data runs collected at Aldermaston with the detector in Compton mode.

^{57}Co

To test the systems ability to image at low gamma ray energies a ^{57}Co point source was used. This source provides two low energy gamma rays at 122 and 136keV without the presence of higher energy gamma rays to cause additional Compton background.

The addback spectra clearly shows the gamma ray peaks at 122 and 136keV. This can be seen in Figure 6.3. This is very different from the spectra seen in Figure 5.16, this is due to the settings on the V1724 (energy thresholds and coincidence time) being different between the two runs.

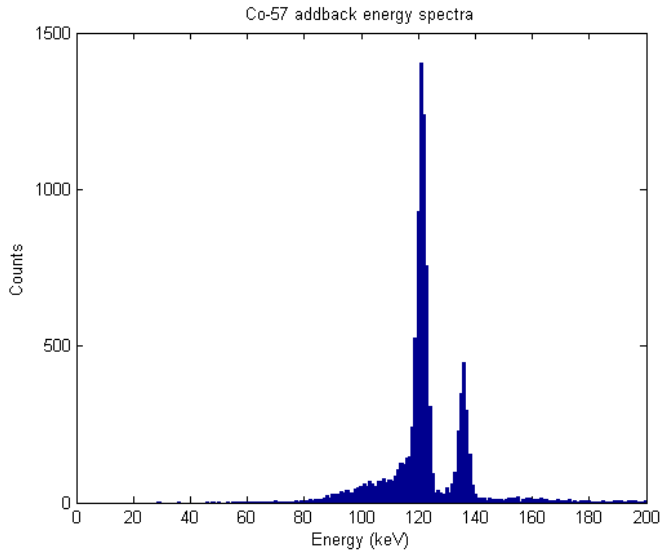

Figure 6.3: Addback energy spectra for a ^{57}Co source. The energy spectra clearly shows the two gamma ray peaks associated with the decay of ^{57}Co, 121 and 136keV.

An image was generated using the 122keV gamma ray, this is shown in Figure 6.4a. This image is shown using a 3mm compression, to allow for the low statistics seen in the image. The results can be seen in Table 6.2, these have a placement error of ± 30mm in all three dimensions.Expected position (430,430).

Position X (mm)	±	Position Y (mm)	±	FWHM X (mm)	±	FWHM Y (mm)	±
443.1	1.6	411.7	1.5	31.8	3.9	27.1	2.3
Average FWHM (mm)			±	Angular resolution (degrees)			±
29.4			1.7	23.1			1.4

Table 6.2: Position and FWHM of the image from ^{57}Co taken at Aldermaston for 3mm compression.

A 122keV gamma ray Compton scattering will deposit a small amount of energy, between 0 and 20keV, within the scatterer. Therefore any contribution from noise will be significant, and will make the image resolution poorer as a result. In addition the probability of back scattered events will increase due to the symmetric behaviour seen in the Klien-Nishina distribution. Taking these factors into consideration the image resolution is acceptable for a low energy point source. As this is a point source an average image FWHM is presented, this is taken by averaging the values calculated from the fit in X and Y.

The image that is reconstructed shows a deviation from the expected position of (430,430). This deviation is 13mm in X and 19mm in Y. This displacement is within the placement error stated at the start of the chapter so are within the expected limits.

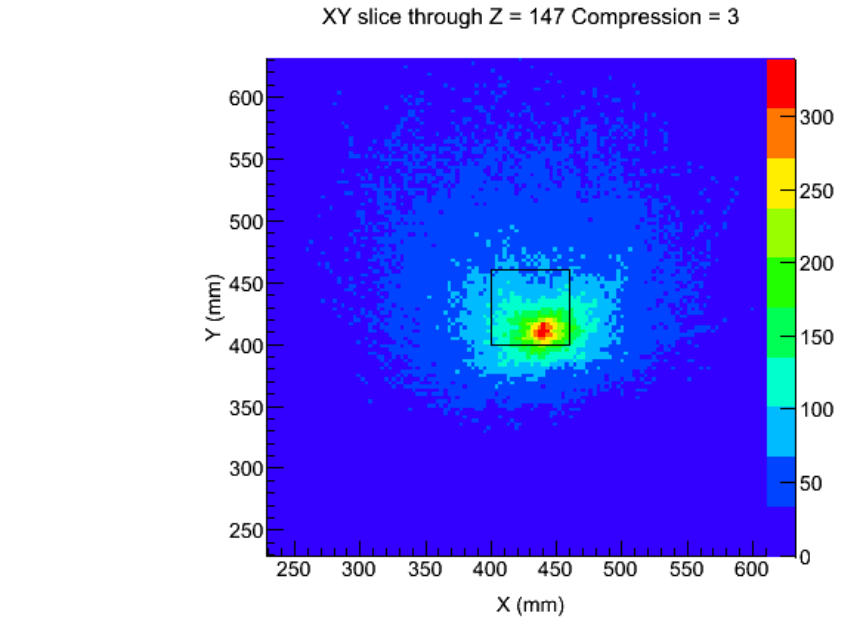

(a)

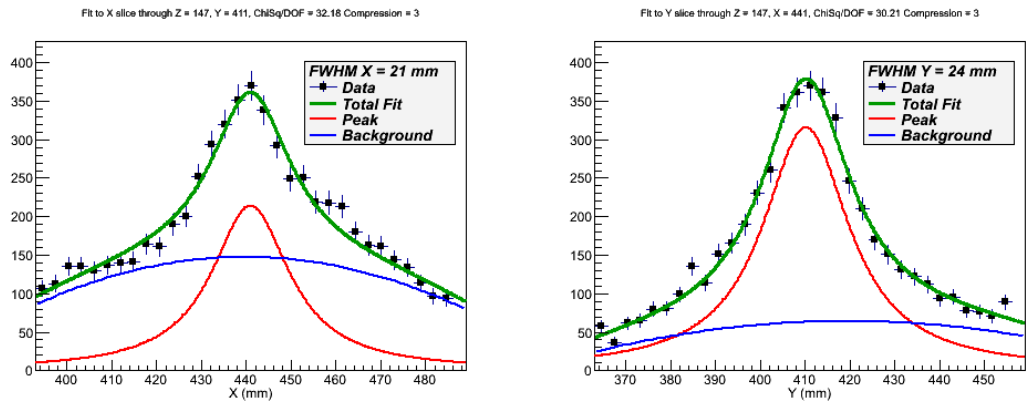

(b) (c)

Figure 6.4: The image produced by energy gating on the 122keV photopeak from ^{57}Co is shown in (a) using a 3mm compression. The average FWHM of the image is 29.4mm $\pm$ 1.7mm. (b) and (c) are cross sections through the X and Y axis respectively, showing the Lorentzian fit to the data used to create the image.

^{152}Eu

A ^{152}Eu was used to test the energy range of the Compton camera. This source was chosen to due to the emission of a number of different gamma rays across an energy range of 122 to1408keV. The addback spectra from this measurement can be seen in Figure 6.5a. This source allows the energy range of the Compton camera to be tested and also its ability to image gamma rays which are present on top of a Compton background caused by the presence of higher energy gamma rays.

The addback spectra shown in Figure 6.5a clearly shows peaks as expected at 122,

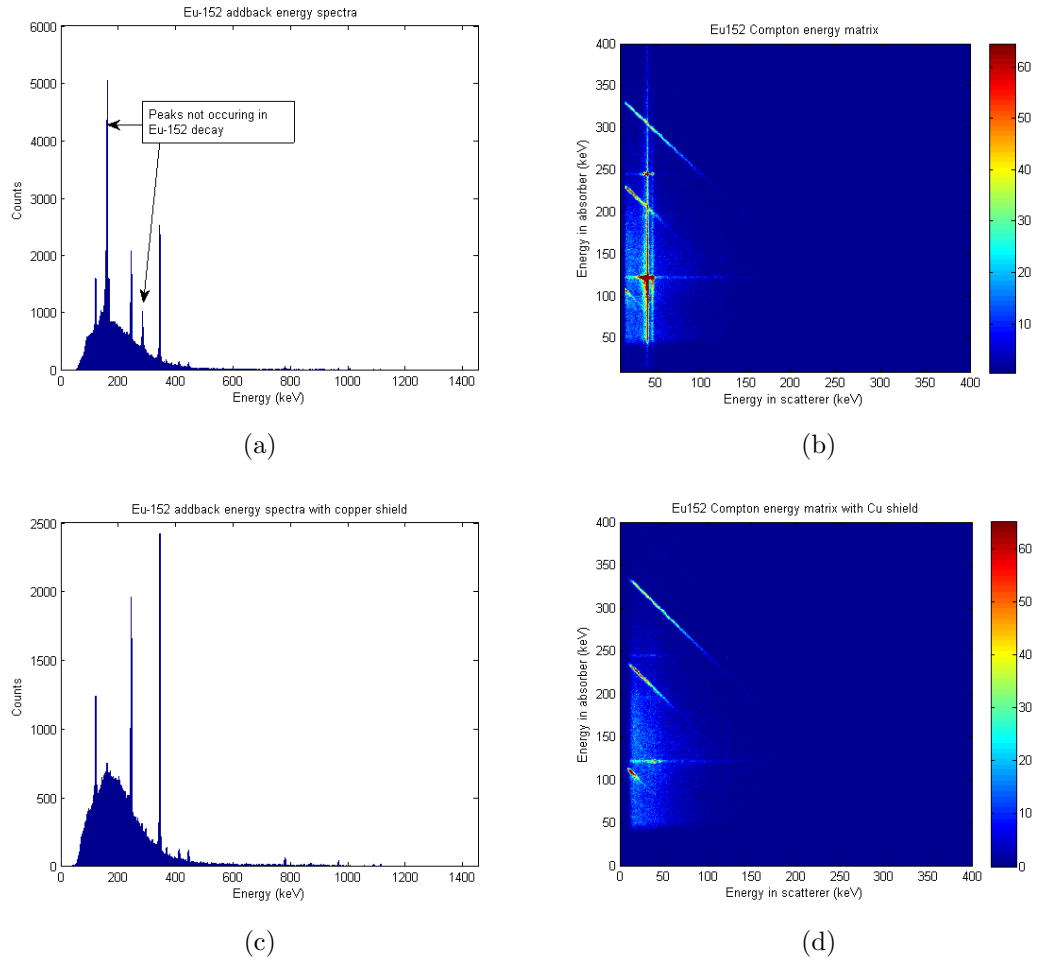

Figure 6.5: Addback energy spectra and addback matrices for the two ^{152}Eu runs taken at Aldermaston. (a) and (b) relate to a run where X-ray and gamma ray coincidences are clearly visible with additional photopeaks seen at 162 and 284keV, a vertical line is clearly visible in the addback matrix at 40keV. The sum of 122 and 244 gamma rays with the 40keV X-ray cause the additional photopeaks. By comparison (c) and (d) show the ^{152} spectra as expected following the use of a 0.95cm thick copper sheet to absorb the X-rays coming from the source. The brighter colours in the matrix indicate more counts.

244, 344, 443 and 778keV however additional peaks are seen at 162 and 284keV. ^{152}Eu provides X-rays of 40keV, these low energy X-rays can also interact in either detector and if a gamma ray interacts within the trigger window the data will be recorded as a Compton event. The X-rays are also released in coincidence with the gamma rays. The effect of this can be seen more clearly if an addback energy matrix is produced, plotting the energy of the scatterer on the X-axis and absorber on the Y-axis. Within this matrix a vertical or horizontal line indicates that either detector is registering a fixed value no matter what energy is deposited within the other detector while a diagonal line will indicate a build up of Compton scattered events. In Figure 6.5b a clear vertical line is present at 40keV indicating that the 40keV X-ray is being absorbed

within the scatterer.

A second run was performed with the same source. This time the source was placed 8.3cm from the scatterer can with a 0.95mm thick copper sheet between the source and the detector. The copper sheet was used to absorb the majority of the X-rays being emitted by the source, allowing only gamma ray coincidences to be measured. The addback spectra of this run can be seen in Figure 6.5c.

The ^{152}Eu peaks are clearly visible up to the 964keV peak. The addback matrix also shows that the majority of the 40keV X-rays are being stopped as the vertical line is reduced significantly as shown in Figure 6.5d.

Spectroscopic information can also be gained from the addback spectra, indicating the number of counts and the energy resolution, this can be found in Table 6.3.

Energy (keV)	Net counts	±	Energy resolution (keV)	±
122	2661	126	3.32	0.33
244	5598	134	3.31	0.33
344	9123	119	3.38	0.34
443	317	37	3.30	0.33
778	240	31	4.00	0.40
964	137	24	3.90	0.39

Table 6.3: This table shows the spectroscopic information gained from the ^{152}Eu addback spectrum taken at Aldermaston.

To evaluate the systems performance as a function of energy, a number of images were produced by energy gating on the 122, 244, 344, 443, 778 and 964keV peaks and the individual images can be seen in Appendix B.1. The information for each peak is presented in 6.4. To allow a direct comparison of all the images the compression was set to 3mm for all the images due to the limited statistics in the 443, 778 and 964keV peaks.

In addition to the individual energy gated images an image was generated by applying gates across the 122, 244, 344, 443 and 778keV. This image is presented in Figure 6.6a. To provide a consistent result this image is presented with a 3mm compression.

The reconstructed positions seen here are again not at the expected (430,430). This is due to the placement errors. The positions also vary with gamma ray energy by up to 6mm in Y and also 2mm in X. This is unexpected as the gamma rays imaged are from the same source. The cause of this is not known however it is not seen in the results taken at Liverpool so does not appear to be physical in nature. It is assumed to be due to the statistics involved in this experiment. The positions reconstructed are within error limits in X but the Y values are not.

By selecting the same five photopeaks the statistics available are increased allowing an image to be produced for a lower compression. The effect of this can be seen be

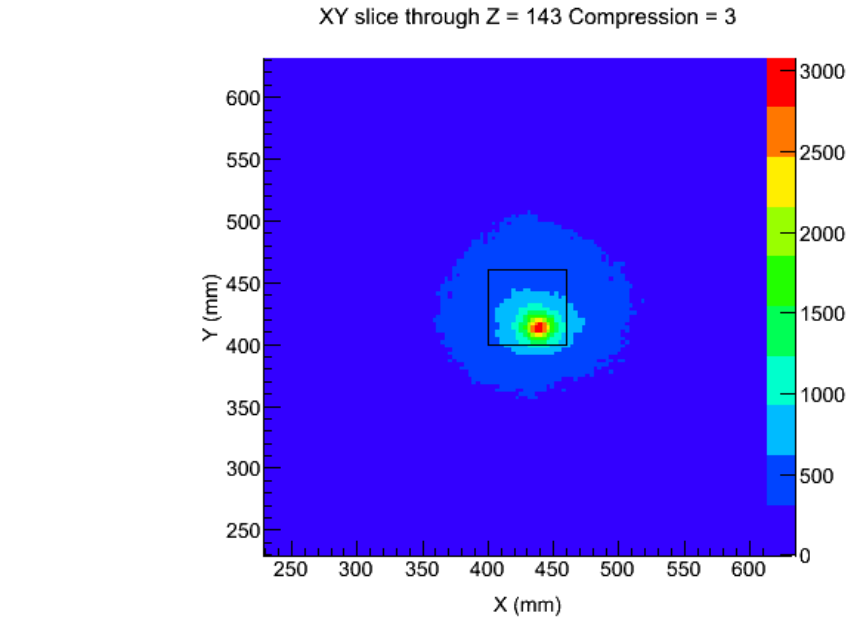

(a)

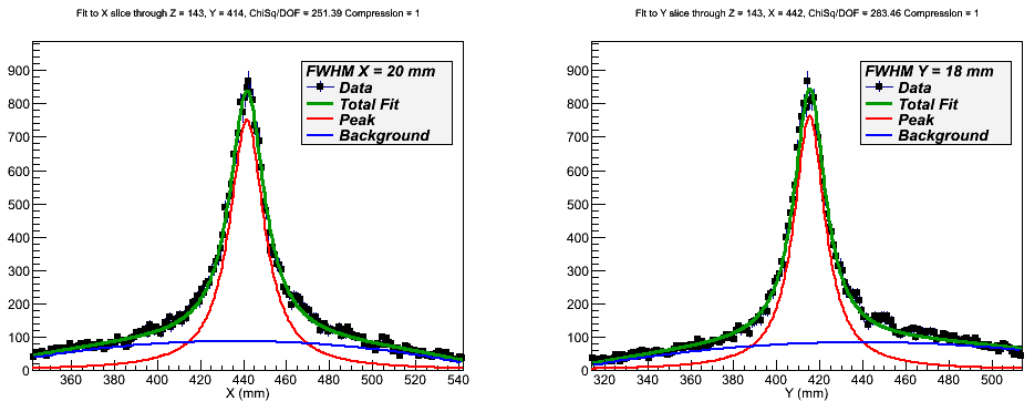

(b) (c)

Figure 6.6: The image produced by energy gating on 122, 244, 344, 443 and 778keV γ rays from ^{152}Eu simultaneously is shown in (a). The average FWHM of the image is 19.2mm $\pm$ 1.1mm. (b) and (c) are cross sections through the X and Y axis respectively, showing the Lorentzian fit to the data used to create the image.

comparing the images in Appendix B.1 with Figure 6.6a. 1mm compression for this source, for comparison the data is presented in Table 6.6.

The image resolution improves as the energy of the gamma ray increases, with an increase shown again at 778 and 964keV. The improvement is expected as the higher energy gamma rays will deposit more energy in both detectors, thus liberating more electron hole pairs and providing a more accurate measurement of the energies deposited. The energy deposition is fractional in nature. The forward focusing of Compton scattered gamma rays also increases as the energy increases, and any Doppler broadening effect within the detectors is reduced as the energy increases. The combination of a

Energy (keV)	Position X (mm)	±	Position Y (mm)	±	FWHM X (mm)	±	FWHM Y (mm)	±
122	441.6	1.6	418.9	1.6	35.5	2.2	26.1	2.8
244	441.5	1.5	415.9	1.5	20.6	1.7	20.2	1.6
344	441.4	1.5	415.5	1.5	18.0	1.7	17.3	1.6
443	440.5	1.6	415.4	1.6	12.9	2.0	12.6	2.2
778	442.2	1.7	413.6	1.6	21.2	2.2	12.7	2.2
964	442.2	1.6	412.5	1.7	14.6	2.2	19.5	3.3
122,244,344,443,778	441.5	1.5	415.7	1.5	20.0	1.61	18.4	1.5

Table 6.4: Position and FWHM of the image from ^{152}Eu taken at Aldermaston.

Energy (keV)	Average FWHM (mm)	±	Angular resolution (degrees)	±
122	30.8	1.8	25.5	1.5
244	20.4	1.2	17.0	1.0
344	17.6	1.1	14.8	1.0
443	12.8	1.5	10.7	1.3
778	17.0	1.6	14.2	1.3
964	17.1	2.0	14.3	1.7
122,244,344,443,778	19.2	1.1	16.1	0.9

Table 6.5: Average FWHM and angular resolution of the images from ^{152}Eu taken at Aldermaston for 3mm compression.

larger number of charge carriers, reduced back scattering events adding to the background of the image and the reduction of Doppler broadening effects should result in a better image. The number of cones used to create the images for 778 and 964keV is small compared to the others resulting in the increase of the image resolution seen.

The effect of using the lower compression value for the combined energies can also be seen in Table 6.6 when compared to the values for the same combined energies in Table 6.5. The image resolution is improved and the associated error is also decreased while the source is reconstructed to the same position within errors for both.

^{133}Ba

^{133}Ba was the next source selected due to its 81keV gamma ray emission, along with higher energy gamma rays. The addback spectra generated from this data is seen in Figure 6.7, this clearly shows that no peak is visible at 81keV. The expected peaks from Ba-133 are 53, 80, 276, 302, 356, 383keV however only the 276, 302, 356 and 383keV peaks are visible. There are also anomalous peaks seen at 111, 334, 415 and 437keV in the spectra (labeled A,B,C and D). These peaks appear to be the product of X-ray/gamma ray coincidences as seen previously with the ^{152}Eu source. A is from a 30keV X-ray being detected in the scatterer along with an 81keV gamma ray being

Position X (mm)	±	Position Y (mm)	±	FWHM X (mm)	±	FWHM Y (mm)	±
441.5	0.5	415.3	0.5	19.6	0.8	17.7	0.6
Average FWHM (mm)			±	Angular resolution (degrees)			±
18.6			0.5	15.6			0.4

Table 6.6: Position and FWHM of the image from ^{152}Eu taken at Aldermaston for 1mm compression. The 122, 244, 344, 443 and 778keV photopeaks were combined to get this result.

seen in the absorber. Similarly B is 30keV + 302keV and C is 30keV + 386. D is caused by an 81keV gamma ray in the scatterer with an 356 keV gamma ray in the absorber.

The decision was taken not to use the copper sheet previously used. This allowed the ability of the detector system to image in the presence of unexpected X-ray/gamma-ray coincidences to be tested.

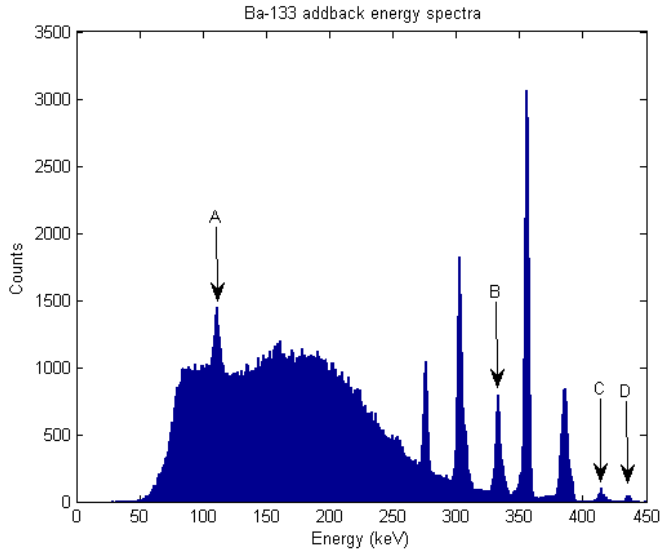

Figure 6.7: Addback energy spectra for a ^{133}Ba source. The energy spectra clearly shows four anomalous peaks marked A (111keV), B (334keV), C (415keV) and D (437keV). The area below 250keV contains a large number of Compton events which have not deposited the gamma rays full energy within both detectors. The anomalous peaks are from X-ray/gamma ray coincidences apart from D. This appears to be due to a 81keV gamma ray being detected by the scatterer at the same time as a 356keV gamma ray is detected in the absorber.

The addback spectra does not show a photopeak at 81keV. The arbitrary setting of thresholds appears to have caused the peak to be lost amongst the Compton continuum from the higher energy peaks present. The minimum energy at which the Compton camera can be shown to work using the Aldermaston setup is therefore 122keV as seen

with the ^{57}Co source.

The image produced by combining the four energy peaks identified as ^{133}Ba is shown in Figure 6.8a. By combining the energies available from the source we maximise the statistics for imaging.

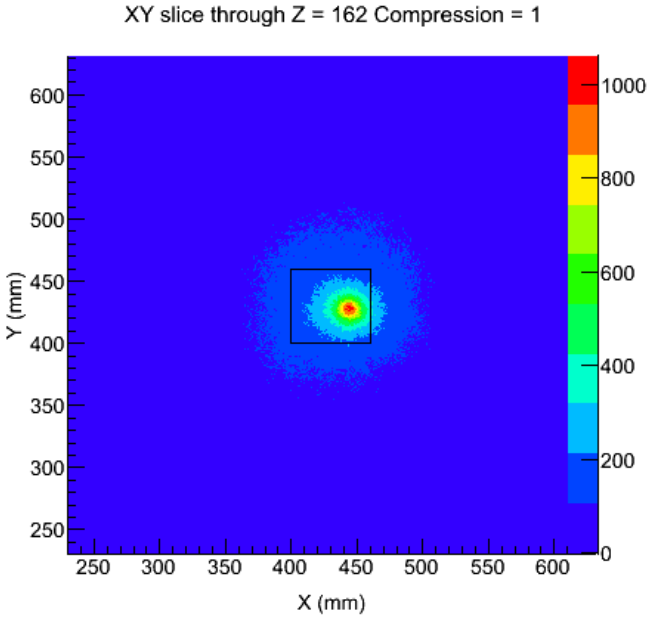

(a)

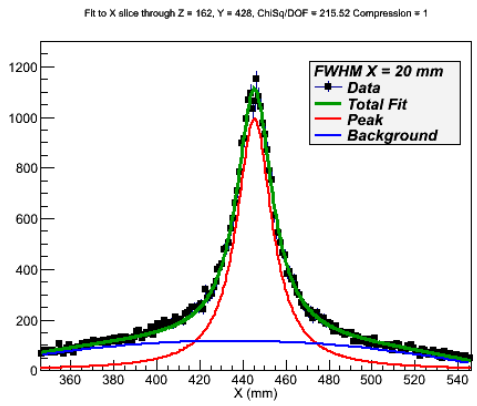

(b)

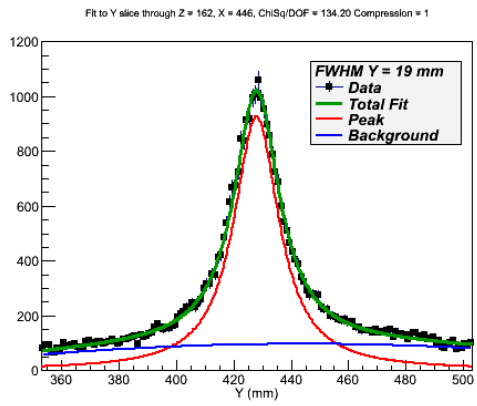

(c)

Figure 6.8: The image produced by energy gating on 276, 302, 356 and 383keV γ rays from ^{133}Ba simultaneously is shown in (a). The FWHM of the image is 19.4mm $\pm$ 0.5mm. (b) and (c) are cross sections through the X and Y axis respectively, showing the Lorentzian fit to the data used to create the image.

The images produced from the ^{133}Ba source show that even with X-ray coincidences present in the addback spectra images can be produced from known photopeaks. The position at which the source was located is within the placement error, the offset in Y is impossible to discern in isolation due to distance being within the placement error. The image produced here is better than that seen for ^{152}Eu as the inclusion of the

Position X (mm)	±	Position Y (mm)	±	FWHM X (mm)	±	FWHM Y (mm)	±
445.4	0.5	427.9	0.5	19.5	0.8	19.2	0.6
Average FWHM (mm)			±	Angular resolution (degrees)			±
19.4			0.5	12.7			0.4

Table 6.7: Position and FWHM of the image from ^{133}Ba taken at Aldermaston.

122keV peak in the combined image for ^{152}Eu will introduce a broadening to the final image.

6.2.3 Distributed sources

Access to SNM materials is difficult as only certain facilities within the UK are allowed to store them. AWE Aldermaston is one such facility so the chance to utilise actual SNM was made available. These sources are not point sources, they are mounted in disks. The images presented will be taken using a combination of the photopeaks identified as coming from the appropriate radioisotope and at a Z slice which is equivalent to the distance measured to the source.

^{235}U

^{235}U is a component that might be used in nuclear weapons manufacture and can also be found within fuel cells used for nuclear power making it very important to be able to identify the presence of this material. Highly enriched uranium is desirable for use in nuclear weapons due to its fissile nature. It emits a number of gamma rays, the most prominent ones are found at 143, 163, 185 and 205keV. These four gamma rays are clearly visible within our addback spectra, Figure 6.9

Energy gating on the four photopeaks available produces the image seen in Figure 6.10a, produced with 3mm compression. The image clearly shows a difference between this source and the point sources previously seen, with an image resolution which is much larger. The compression level chosen produces a good image visually, by combining the image bins we reduce the error seen on each individual point fitted while maintaining a bin size small enough to investigate the shape of the object. The exact position of the source within the disk is unknown, the source is sealed to prevent contamination so there will be a different radius of actual nuclide when compared to the measurement taken of the disks diameter.

For a distributed source the FWHM of the image should provide a guide to the size of the source. Here the average FWHM is 30.9mm ± 1.2mm which is larger than the disk diameter of 25mm. Taking into account the errors the source size is still overestimated by +4mm. This is likely to be caused by the fitting program expecting a Lorentzian shaped peak which comes to a point rather than a distributed source, an

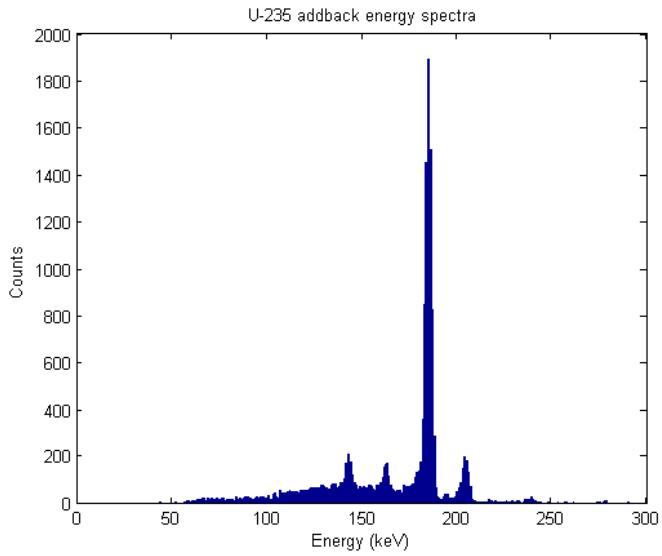

Figure 6.9: Addback energy spectra for a U-235 source. Four photopeaks are clearly visible, 143, 163, 185 and 205keV. These energies match up to four of the most likely gamma rays to be emitted by ^{235}U.

Position X (mm)	±	Position Y (mm)	±	FWHM X (mm)	±	FWHM Y (mm)	±
440.8	1.5	408.2	1.5	32.3	1.8	29.4	1.7
Average FWHM (mm)				±			
30.9				1.2			

Table 6.8: Position and FWHM of the image from ^{235}U taken at Aldermaston for 3mm compression.

estimate by eye is more likely to produce a good fit. The background fit is also suspect on the Y cut, due to the background levels being much higher on the right hand side of the plot.

The position of the source is reconstructed to be +10mm in X and -12mm in Y away from the centre line of the detectors where it was placed. This is likely to be caused by the placement error previously discussed.

^{239}Pu

^{239}Pu is another component that might be used in nuclear weapons manufacture, it can also be found in high levels within breeder type reactors where it is a by-product of the nuclear reaction used to generate power, an example of its generation can be seen in Figure 6.11.

The decay of ^{239}Pu involves the emission of a large number of different energy gamma rays, most of which have very small branching ratios which can make it difficult

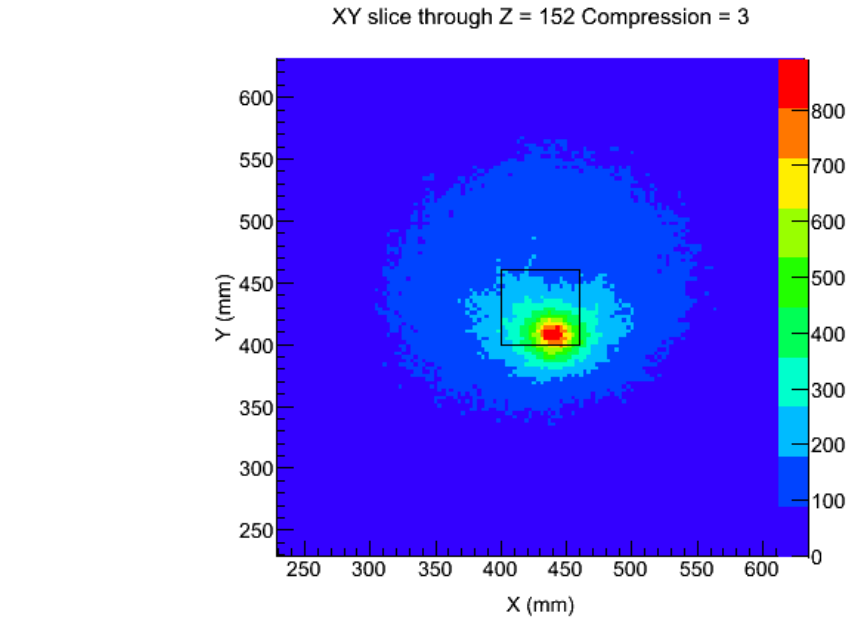

(a)

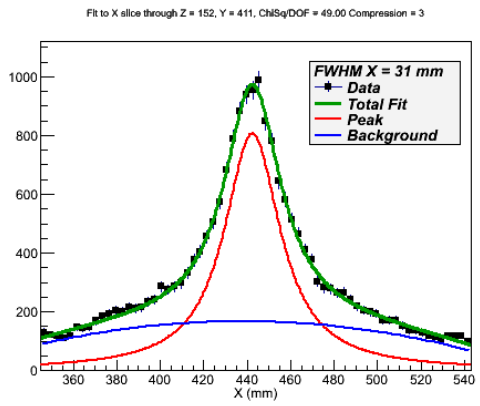

(b)

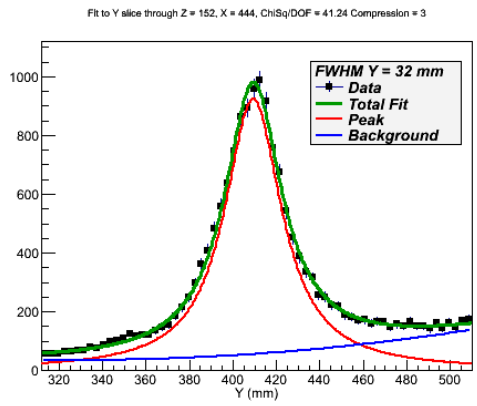

(c)

Figure 6.10: The image produced by energy gating on the 143, 163, 185 and 205keV photopeaks from ^{235}U is shown in (a). The average FWHM of the image is 30.9mm ± 1.2mm. (b) and (c) are cross sections through the X and Y axis respectively, showing the Lorentzian fit to the data used to create the image.

to detect. If the material is old enough to have reached secular equilibrium there will also be a number of different radionuclides present formed by the decay of ^{239}Pu, these can cause issues in identifying the ^{239}Pu, this is clearly shown by the addback spectra taken from our sample, Figure 6.12.

The additional peaks will not be investigated, they could be directly from decay products of ^{239}Pu but they could also be due to the summation of X-rays and/or gamma rays from ^{239}Pu itself and any decay products. In particular the decay of ^{239}Pu produces ^{241}Am which has a number of gamma rays and X-rays from 60keV down which will introduce summation peaks.

$$^{238}_{92}\mathrm{U} + ^{1}_{0}\mathrm{n} \longrightarrow ^{239}_{92}\mathrm{U} \xrightarrow[23{,}5\ \mathrm{min}]{\beta^-} ^{239}_{93}\mathrm{Np} \xrightarrow[2{,}3565\ \mathrm{d}]{\beta^-} ^{239}_{94}\mathrm{Pu}$$

Figure 6.11: Reaction by which ^{239}Pu is formed in a reactor.

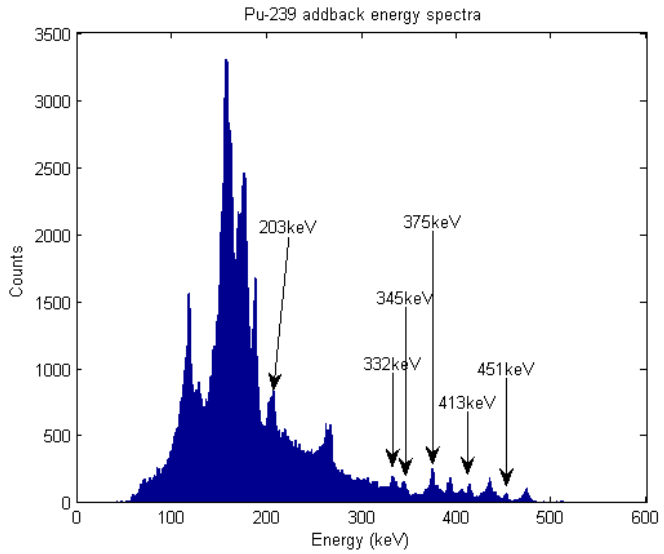

Figure 6.12: Addback energy spectra for a ^{239}Pu source. The addback spectra shows the difficulty in measuring the ^{239}Pu sample provided due to contaminants. The contaminants present obscure the very low branching ratio gamma ray peaks. Six peaks, 203, 332, 345, 375, 413 and 451keV can however be identified as coming from ^{239}Pu. The additional peaks seen are from contaminants as well as summations of lower energy gamma rays or X-rays so will not be investigated.

There are six peaks, 203, 332, 345, 375, 413 and 451keV which are directly attributable to the decay of ^{239}Pu and the image produced by gating on all of these energies can be seen in Figure 6.13a . This image was produced with a compression factor of 3 taking into account the statistics available and also the size of the source. The source is contained with the 4.5cm diameter disk, its exact location within this is unknown.

Position X (mm)	±	Position Y (mm)	±	FWHM X (mm)	±	FWHM Y (mm)	±
442.3	1.6	399.5	1.6	33.3	2.0	39.8	2.3
Average FWHM (mm)				±			
36.5				1.5			

Table 6.9: Position and FWHM of the image from ^{239}Pu taken at Aldermaston for 3mm compression.

The average FWHM of the image is 36.5mm ± 1.5mm compared to the disk diameter of 45mm. The exact encapsulation of the source is not known, however the image

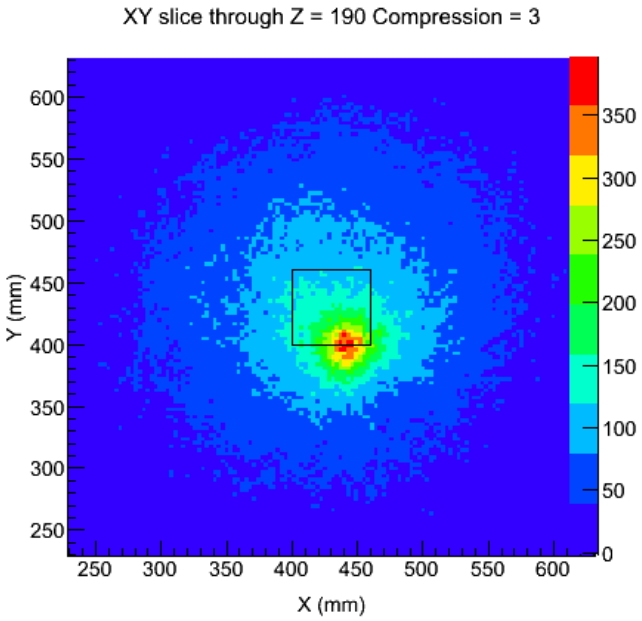

(a)

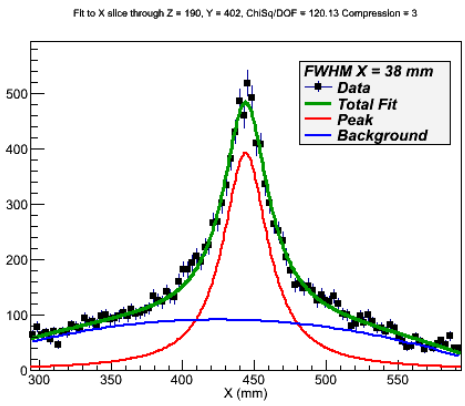

(b)

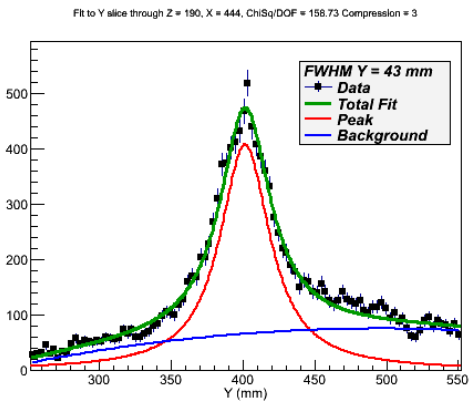

(c)

Figure 6.13: The image produced by energy gating on the 203, 332, 345, 375, 413 and 451keV photopeaks from ^{239}Pu is shown in (a). The FWHM of the image is 36.5mm ± 1.5mm. (b) and (c) are cross sections through the X and Y axis respectively, showing the Lorentzian fit to the data used to create the image.

produced gives a size within the diameter of the disc housing the material. Ideally a smaller compression would be used to image a data set collected over a longer time period.

6.3 Summary

The results of this chapter are summarised in the following tables, one showing the Compton cameras ability to locate a source to the expected position, Table 6.10, the other showing the quality of the image produced, Table 6.11.

Source	γ ray Energy (keV)	Expected X (mm)	Expected Y (mm)	Measured X (mm)	$\pm$	Measured Y (mm)	$\pm$	Compression
^{57}Co	122	430	430	443.1	1.6	411.7	1.5	3
^{152}Eu	122	430	430	441.6	1.6	418.9	1.6	3
^{152}Eu	244	430	430	441.5	1.5	415.6	1.5	3
^{152}Eu	344	430	430	441.4	1.5	415.5	1.5	3
^{152}Eu	443	430	430	440.5	1.6	415.4	1.6	3
^{152}Eu	778	430	430	442.2	1.6	413.6	1.6	3
^{152}Eu	964	430	430	442.2	1.6	412.5	1.7	3
^{152}Eu	122 - 964	430	430	441.5	1.5	415.7	1.5	3
^{152}Eu	122 - 964	430	430	441.6	0.5	415.3	0.5	1
^{133}Ba	276 - 383	430	440	445.4	0.5	427.9	0.5	1
^{235}U	143 - 205	430	430	440.8	1.5	408.2	1.5	3
^{239}Pu	203 - 451	430	420	442.3	1.6	399.5	1.6	3

Table 6.10: Summary table showing the measured position of the source compared to the expected position. The expected positions have an error of $\pm$ 30mm.

Despite unoptimised settings, working restrictions and the short time available the work at Aldermaston produced images across an energy range of 122 to 964keV. The image resolution reduced as the gamma-ray energy increased unless the statistics collected were poor. The images produced at 122keV had large FWHM measurements, this was expected due to the energy deposited in the scatterer being just above the noise levels of the detector. No angle gating was required for these images, unlike the work presented from Liverpool, this is due to the use of low energy thresholds used in the scatterer for the work carried out at Aldermaston. The percentage error caused by the noise included is larger at lower energies producing a larger error in the cone angle. The possibility of back scattered events is also increased at lower energies, these will contribute to the background seen in the images produced, which is more noticeable in the images produced for lower energy gamma-rays.

The placement error involved in the measurements at Aldermaston is large, this may be covering other issues causing the system to reconstruct the source position incorrectly which would include reconstruction code errors, any lense effects such as pin cushioning which may be present and the detectors not being properly aligned. To look at these effects further the detectors must be aligned properly, ideally using a source scanned across the front face of the scatterer. This should then be followed by a raster scan measurement where a source is moved across a grid of known points, the images for each point can then be reconstructed to find any errors in the positions found.

The work at Aldermaston passed useful information to the AWE staff in gaining experience in dealing with experimental detector systems and associated electronics.

Source	γ ray Energy (keV)	Average FWHM (mm)	$\pm$	Angular resolution (degrees)	$\pm$	Compression
^{57}Co	121	29.4	1.6	23.1	1.4	3
^{152}Eu	122	30.8	1.8	25.5	1.5	3
^{152}Eu	244	20.4	1.2	17.0	1.0	3
^{152}Eu	344	17.6	1.1	14.8	1.0	3
^{152}Eu	443	12.8	1.5	10.7	1.3	3
^{152}Eu	778	17.0	1.6	14.2	1.3	3
^{152}Eu	964	17.1	2.0	14.3	1.7	3
^{152}Eu	122 - 964	19.2	1.1	16.1	0.9	3
^{152}Eu	122 - 964	18.6	0.5	15.6	0.4	1
^{133}Ba	276 - 383	19.4	0.5	12.7	0.4	1
^{235}U	143 - 205	30.8	1.2			3
^{239}Pu	203 - 451	36.5	1.5			3

Table 6.11: Summary table showing the average FWHM and angular resolution for the Aldermaston data.

Access to SNM which would otherwise be unavailable was advantageous to the work as the systems ability of imaging isotopes with contaminants present could be tested. The use of the system within a different laboratory space and within a highly secure environment was also invaluable experience for the University of Liverpool for any further projects which may take place on this type of site. The images produced show that even with a non-optimal system setup good results could still be obtained.

Chapter 7

GAMOS Simulation

Simulations are an important tool when designing detector systems and also in predicting their performance over a range of parameters. By utilising simulations the risk of building a detector only to find it does not meet the specific requirements can be mitigated before the expense of manufacturing the device. Simulations can also be used to test how a detector is likely to perform. By validating simulations against experimental work with the same detector system various parameters can be tested and provide results which should closely match the experimental setup. This is especially important when dealing with very high activity sources which may pose a risk to the operators health and also removes the need to have a source of specific energy for testing.

A variety of different simulation packages are available, the majority can be split into two different methods. The methods used are either Monte Carlo [47] or point kernel. In Monte Carlo simulations a random number seed is used to represent a particle, this particle is then stepped through a geometry and the probability of interaction is checked at each point. It requires an area to score particles in, this represents the detector and will provide only an output relating to the interactions within the detectors.

The second method is a point kernel simulation. This solves radiation transport codes across points in a user defined mesh. The information at each point is retained so a specific detector area is not defined. Point kernel codes are generally used to provide solutions for the flow of radiation through an area rather than the detector response which Monte Carlo codes provide. Due to the large number of computations required and the necessity to store every point this type of radiation transport simulation is very computer intensive.

A large number of different simulation Monte Carlo techniques are available, here the main emphasis will be placed on the GAMOS [48] toolkit for Geant 4 application [49]. MCNP [50] is a standard Monte Carlo particle transportation code for neutrons and photons. The inclusion of a validated Compton camera function in GAMOS and the need to use coincident events which cannot easily be replicated in MCNP meant that GAMOS was chosen to carry out the simulations.

Simulations of a Compton camera must take account of the geometry, energy resolution of the detectors, incident gamma ray energy, detector separation, coincidence timing between the detectors and the materials of the detectors involved [51]. The physics applied to the model must also be correct for the application, ensuring that the energy range is covered for the gamma rays and that the appropriate interactions are included. The photon interactions that need to be included are Doppler broadening, Compton scattering, pair production and photoelectric absorption.

7.1 GAMOS

GAMOS is a toolkit for Geant4. By providing a more user friendly interface the requirement for the user to be able to program in C++ is removed. Initially GAMOS was designed to be used for medical applications and now includes a Compton camera class in which the Compton events are output into Root files and text files. For the simulation presented here GAMOS 3.0.0 was used, using the low energy physics list in Geant4. The version of Geant4 used by this GAMOS version is 9.4 using patch 01. The output is formated into root files and libraries to provide access to the addback spectra and also binary data which can be used to create images.

7.2 Compton camera simulation

The circular detector was put into GAMOS by creating a boxed shape to represent the circle. This shape was required to create pixels of the correct size to represent the strips and to be used as detector regions while maintaining a volume equivalent to that of the circle. The absorber was created using inbuilt functions allowing a volume to be filled completely with a number of smaller daughter volumes, 5x5x20mm pixels were created to represent this detector.

An image of the shape created to represent the scatterer can be seen in Figure 7.1a. To provide a validation the shape then had to be altered to match the detector used experimentally, removing two strips from one side and one from the other. A diagramatic representation of this can be seen in Figure 7.1b.

7.3 Validation

There are a number of different methods to validate simulated data against experimental data, some examples of methods used can be found in [52, 53]. Due to the dead time used for the experimental data being an estimate the simulation used will be validated against the final image resolution rather than the Compton efficiency. The factors influencing the image resolution are the detectors energy resolution, position resolution and the geometry of the setup [53]. If the images appear to be similar in

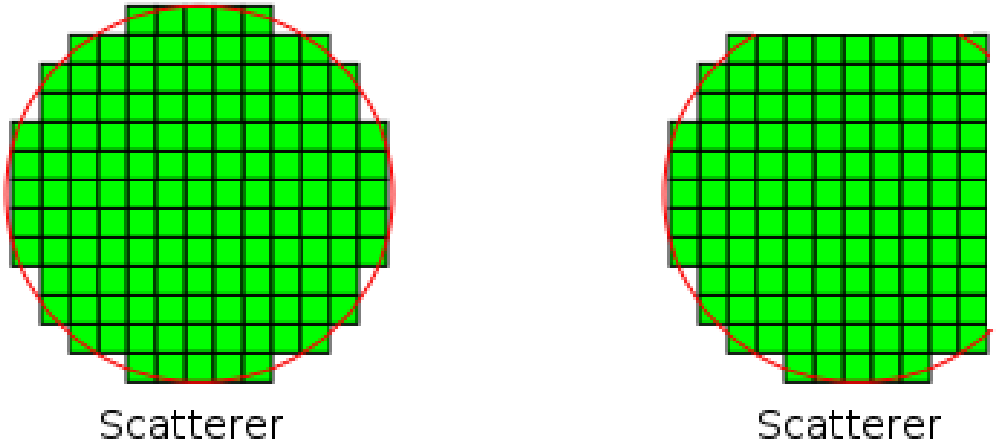

(a) (b)

Figure 7.1: Schematic diagram of the full circular scatterer (a) showing the circle as the red line and pixel set as green boxes. (b) shows the schematic diagram of the scatterer when it was simulated to match the experimental detector.

resolution these factors should be correctly set within the simulation.

The simulation will use a ^{137}Cs source positioned at 4.6cm from the scatterer crystal, with an activity of 300kBq the image produced is shown in Figure 7.2a. The image produced experimentally from a source at the same distance from the detector can be seen in Figure 7.2b. The images were produced using the same number of cones to provide a direct comparison.

The image resolutions seen at 662keV are very similar. The results are displayed in Table 7.1.

	Simulated				Experimental			
Energy (keV)	FWHM X (mm)	±	FWHM Y (mm)	±	FWHM X (mm)	±	FWHM Y (mm)	±
662	13.4	0.7	13.0	0.7	14.2	0.7	13.2	0.8

Table 7.1: Simulated and experimental FWHM measurements for comparison.

7.3.1 Efficiency

The efficiency of a detector system will be influenced by the materials around the detector crystals, additional materials in any holding structures, the dead time of the system including the detector reset time, low energy threshold settings and the energy of the incident gamma-ray [53].

To produce a simulated efficiency plot, a gamma ray source was positioned 11.6cm away from the scatterer crystal in GAMOS. This matches the geometry of the ^{152}Eu measurement taken to show the experimental efficiency plot shown in Figure 5.7. The

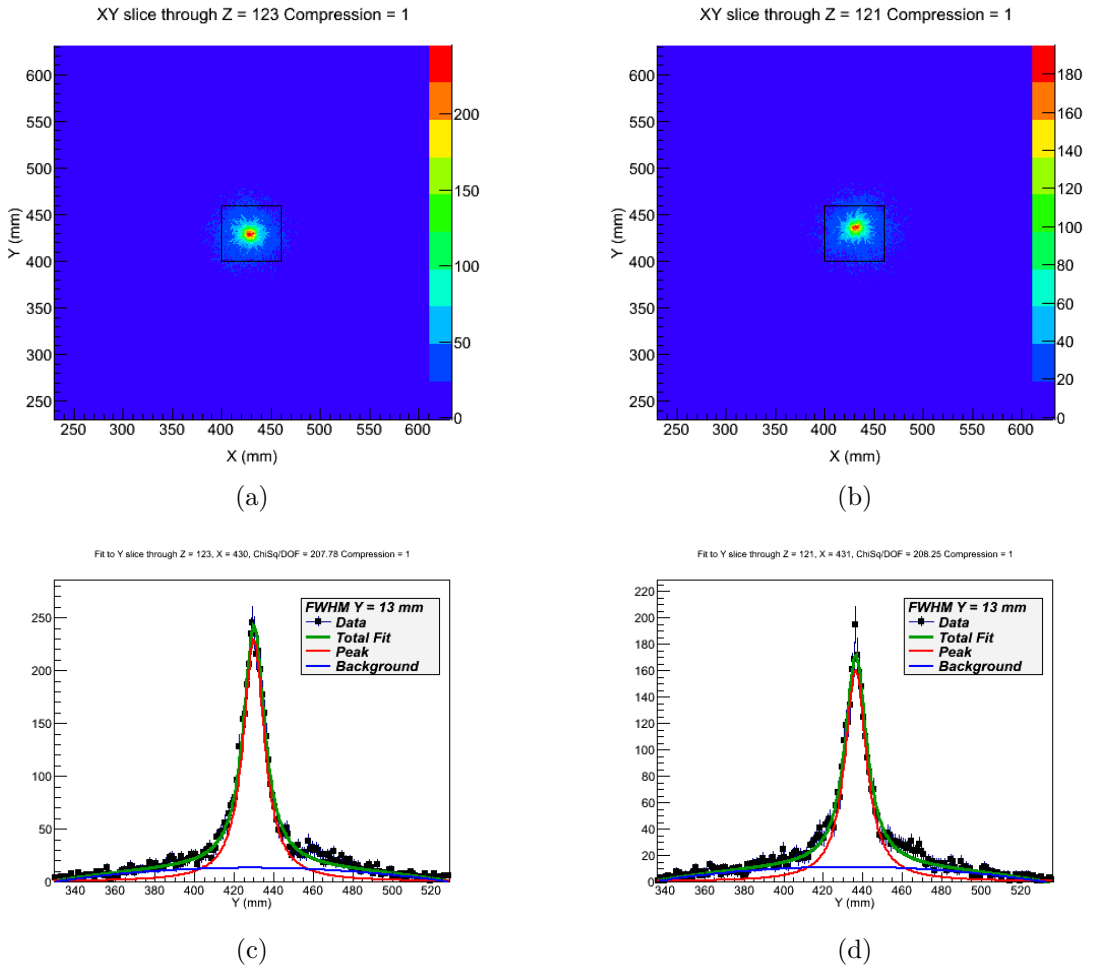

Figure 7.2: Simulated ((a) and (c)) and experimental ((b) and (d)) images produced with a ^{137}Cs source at a distance of 4.6cm from the scatterer crystal. All the images have a 1mm compression.

amount of surrounding material, energy thresholds and the dead time of the detectors can be altered to allow the simulated efficiency to match that found experimentally. Each energy from ^{152}Eu was run individually and the results are combined to produce an absolute Compton efficiency plot which can be compared to the one found experimentally. The simulated points are found to be significantly higher than those of the experimental data, by a factor of three as shown in Figure 7.3. The shape of the curve seen is as expected and follows that found experimentally indicating that there is a systematic error in the experimental data causing the discrepancy between the simulated and experimental data. The GAMOS data has negligible errors (square root of the number of counts measured in each peak, due to the low numbers run this will be a small value) while the experimental result has an estimated 10% error as shown on the experimental points.

By applying a coincidence time delay of 7μs to the detectors allows the simulation to be made to match the experimental data, as seen in Figure 7.4.

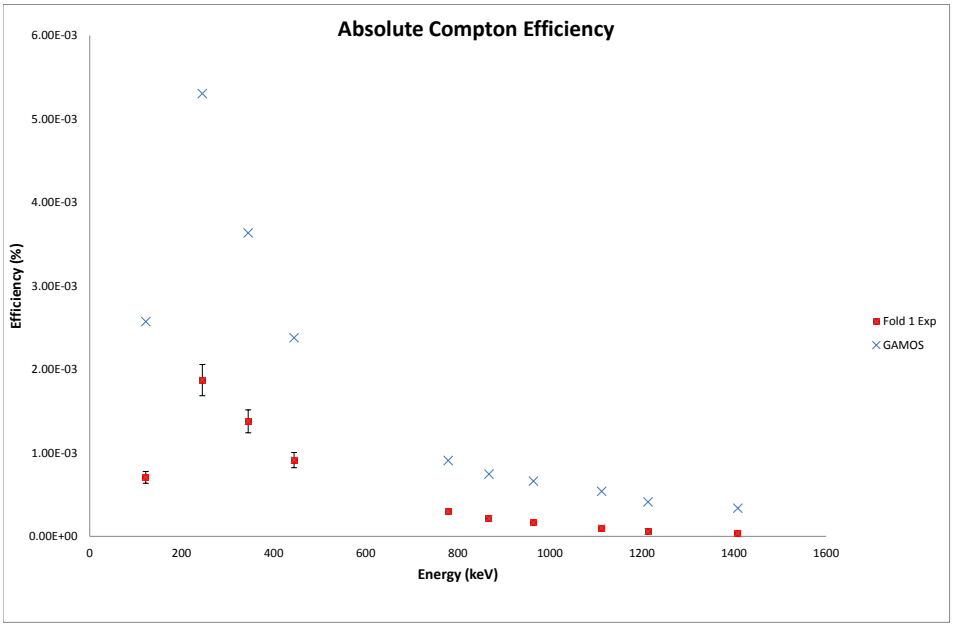

Figure 7.3: Plot of the absolute Compton efficiency found using the GAMOS simulation compared to the experimental plot. This plot indicates a systematic error in the experimental data resulting in a loss of data.

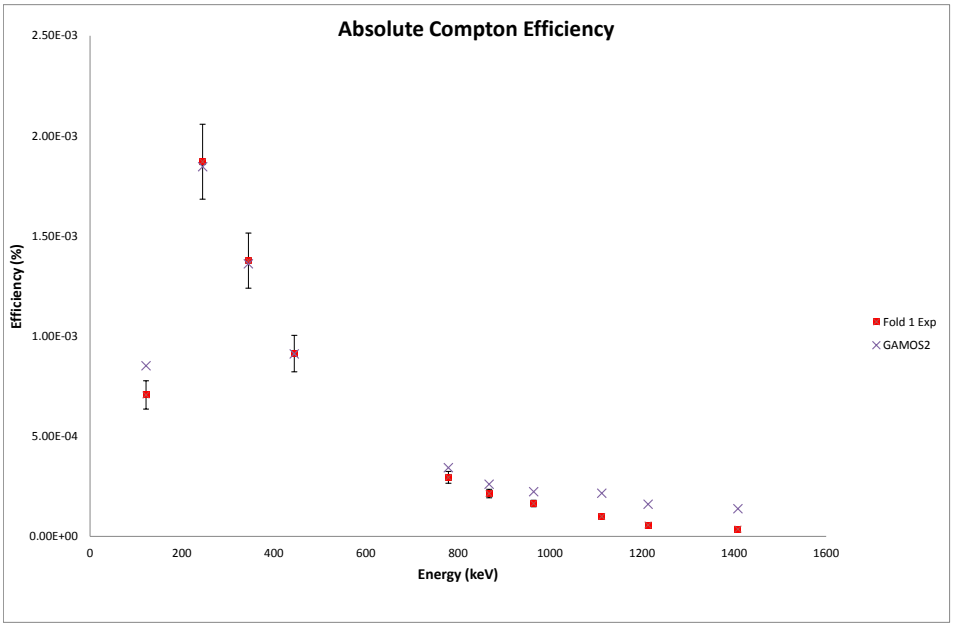

Figure 7.4: Plot of the absolute Compton efficiency found using the GAMOS simulation compared to the experimental plot after adding an additional non physical time factor.

This way of matching the data sets is not physical and just provides a method of removing data points from the simulation until it matches the experimental data. The difference between the data sets at low energies following this matching process is due to the harsh energy threshold being set by GAMOS, the experimental data has threshold of 15 and 30keV as set in GAMOS however there is a $\pm$ 10keV error on the experimental data. At higher energies the possibility of the charge cloud being created by an interaction drifting across a strip boundary and thus the event being recorded as a fold 2 event is increased experimentally. This leads to the simulated data being higher than that seen from experimental. These issues have previously been seen [53] so were expected and taken into consideration when applying the coincidence time delay to the simulated data.

The experimental data collected had a coincidence window of 250ns, this removed $\sim$12% of the data at 511keV. This value will vary with gamma ray energy. In addition to this the dead time of the system is not fully understood with the new digital electronics, and incorrect settings may of contributed to the data loss causing additional dead time or event pile up. In the system pile up events, events which occur while the detector system is processing another event, are deleted. Dead time will be introduced from the system writing out traces and also the shaping time used on the moving window deconvolution filter which is used to provide the energies deposited in the

detectors. To investigate this fully it is recommended that a comparison between an analogue electronics setup and the new digital system be carried out, this should provide information on the dead time and any other possible data loss in the system.

7.4 Simulating the effect of smaller pixels

The main reason for building the simulation of the Compton camera was to test the effects of using smaller pixel sizes, which can be achieved experimentally using pulse shape analysis. To achieve this in the simulation the pixel size can be altered in x and y to simulate the effects of applying image charge analysis to the experimental data. The method used to build the detector cannot be used to measure the effects of the depth of interaction at this moment in time.

7.4.1 Image charge analysis

Image charge analysis will provide an interaction position with respect to a strip boundary in both x and y by analysing the strips neighbouring one that contains an interaction. To simulate this effect being applied the detector is divided into smaller pixels, of 2.5x2.5mm and then 1x1mm. This is done for the absorber detector which shows image charges which are large enough to use experimentally. The scatterer shows almost no usable image charges, only producing them when a very large energy deposit is made, which would not be the case for a Compton camera system. The effects of using smaller pixels in the scatterer will be modeled to show the improvement that could be made if the noise levels on the silicon detector were low enough to see image charges or if a smaller pitch strip was used on the detector. In addition the use of smaller pixels on both detectors together will also be shown using the 1x1mm voxel size. The images presented here are limited to 409 cones, this was done to match the full set of results across the detectors and show only the effect of making the voxels smaller. A compression factor of 3 was used to give a good fit and visual image with the statistics available.

As the voxel size is decreased there is an increased probability of multiple scatters being detected by GAMOS within what was a single voxel previously, this leads to a reduction of the number of cones available to image.

7.4.2 Application to the absorber

The images produced by using smaller voxels on the absorber can be seen in Figure 7.5 and the associated image resolutions can be seen in Table 7.2. The voxel size of the scatterer is retained (5x5mm in x and y).

The results show a small improvement on the image resolution as expected. The use of a smaller voxel size in the absorber detector will show a small improvement to

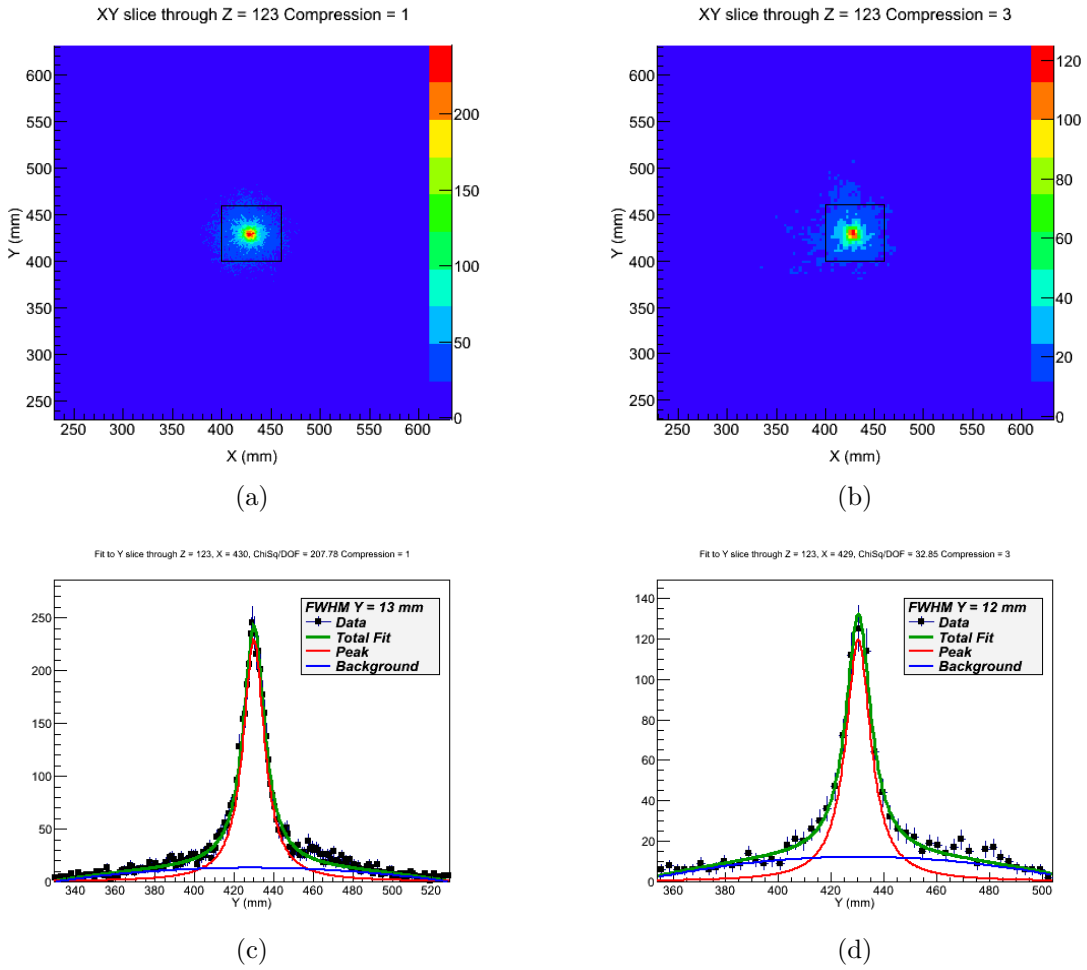

Figure 7.5: Simulated effect of applying a smaller pixel size to the absorber. (a) and (c) relate to using a voxel size of 5x5mm in both detectors, while (b) and (d) relate to a voxel size of 1x1mm in the absorber (and 5x5mm in the scatterer). This simulated data is for a 662keV gamma ray source.

the image resolution, thus if image charge analysis was applied a similar improvement should be seen experimentally.

Application to the scatterer

The images produced by using smaller voxels in the scatterer can be seen in Figure 7.6 and the associated image resolutions can be seen in Table 7.3. The absorber detector has a voxel size fixed to 5x5mm in x and y.

The results show a larger improvement to the image resolution when applying smaller voxel sizes to the to the scatterer alone, compared to those seen for applying the same smaller voxels sizes on the absorber alone. This result shows that using smaller voxels is more effective if applied to the scatterer if it is only to be applied to one detector. Image charge analysis could be used in the future to experimentally produce this effect, if the noise levels can be reduced. Another way of doing this would

Voxel size (mm)	FWHM X (mm)	±	FWHM Y (mm)	±	Average FWHM (mm)	±
5	13.4	1.9	13.5	1.9	13.5	1.3
2.5	12.3	1.8	12.3	1.9	12.3	1.3
1	12.6	1.8	11.9	1.8	12.2	1.3

Table 7.2: Simulated effects of using different voxel sizes in the absorber while keeping the scatterer voxels at 5x5mm.

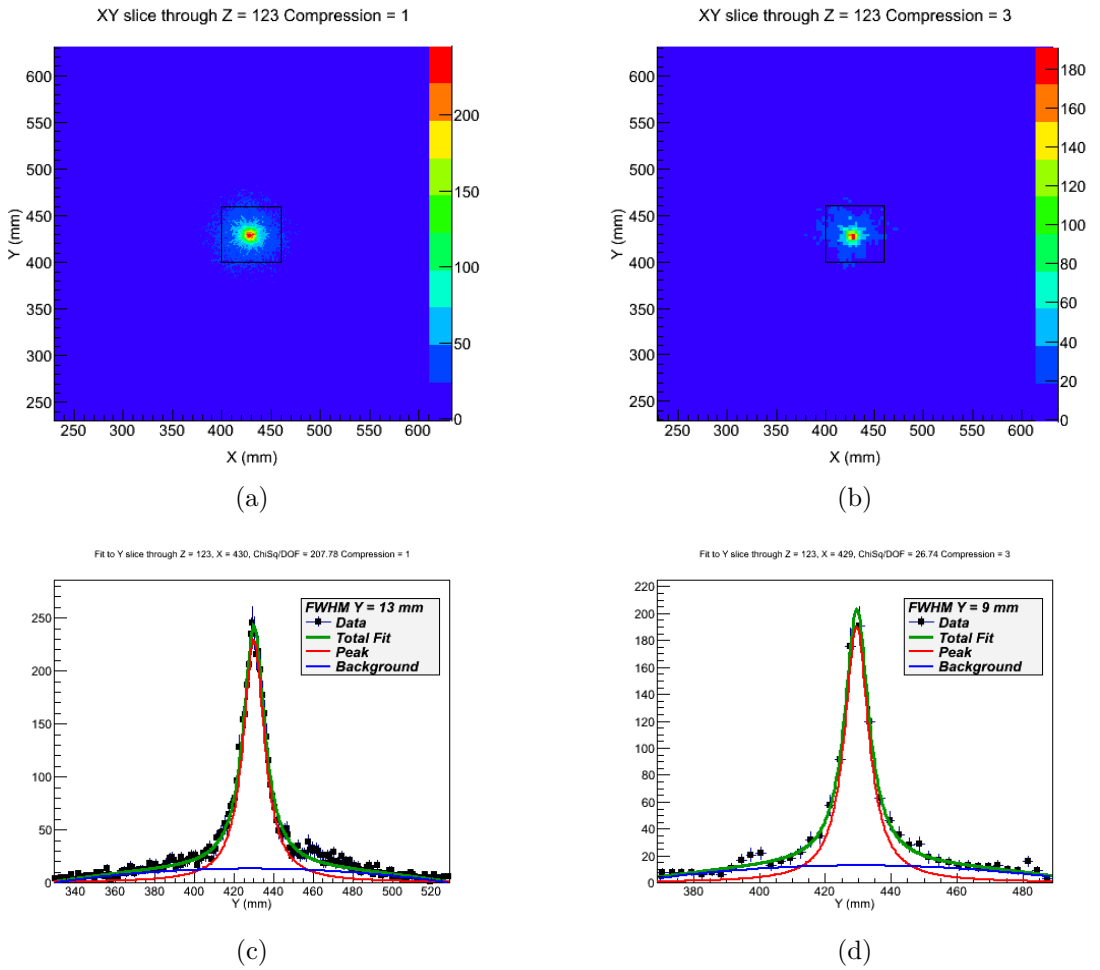

Figure 7.6: Simulated effect of applying image charge analysis to the scatterer. (a) and (c) relate to using a voxel size of 5x5mm for both detectors, while (b) and (d) relate to a voxel size of 1x1mm in the scatterer (absorber voxels are 5x5mm). This simulated data is for a 662keV gamma ray source.

be to replace the scatterer detector with one that has a smaller strip pitch.

Application to both detectors

The images produced by using smaller voxels in the scatterer and also the absorber, using the same voxel size for both can be seen in Figure 7.7 and the associated image resolutions can be seen in Table 7.4.

Voxel size (mm)	FWHM X (mm)	±	FWHM Y (mm)	±	Average FWHM (mm)	±
5	13.4	1.9	13.5	1.9	13.5	1.3
2.5	10.6	1.7	9.1	1.7	9.9	1.2
1	9.9	1.6	8.8	1.7	9.4	1.2

Table 7.3: Simulated effects of using different voxel sizes for the scatterer, while keeping the absorber voxel size at 5x5mm.

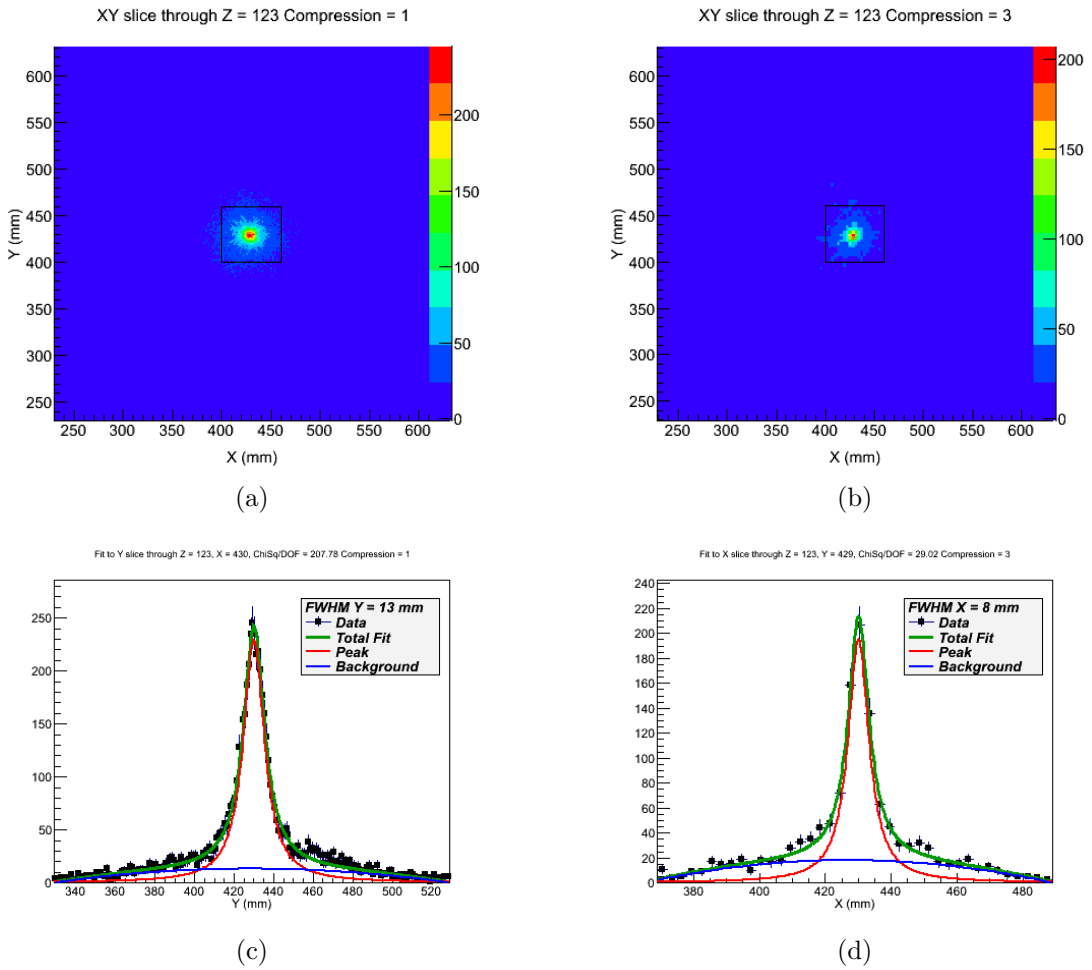

Figure 7.7: Simulated effect of using different voxel sizes for the scatterer and the absorber, keeping the voxel sizes the same in each detector. (a) and (c) relate to using a voxel size of 5x5mm while (b) and (d) relate to a voxel size of 1x1mm. This simulated data is for a 662keV gamma ray source.

By using smaller voxel sizes for both detectors the image resolution improves by almost 5mm. The quantity of simulated data that could be used decreased as the voxel sizes were decreased, due to GAMOS identifying events which scattered twice within a single voxel as different interactions in the smaller areas, this is shown in Table 7.5. Similar results are seen decreasing the voxel size for each detector individually. The application of image charge analysis is therefore advantageous for both detectors

Voxel size (mm)	FWHM X (mm)	±	FWHM Y (mm)	±	Average FWHM (mm)	±
5	13.4	1.9	13.5	1.9	13.5	1.3
2.5	8.8	1.7	9.5	1.7	9.2	1.2
1	7.7	1.6	9.6	1.6	8.7	1.2

Table 7.4: Simulated effects of using different voxel sizes on the scatterer and absorber at the same time, using the same voxel size in each detector.

though events which interact more than once within a voxel would ideally be removed before imaging as these will contribute an error from the uncertainty in the interaction position used.

Voxel size (mm)	Counts available	% of starting value
5	2765	100
2.5	709	25
1	409	15

Table 7.5: The percentage number of counts available to image when different sized voxels are used for both detectors at the same time.

This indicates that there is a limit to how small the voxels can be made to retain enough fold1,1,1,1 interactions to produce an image. Multiple interactions will also introduce an uncertainty to the images produced so methods of removing these from the data should be investigated in the future, one possible method is using wavelet analysis [54].

7.5 Best slice simulation

To investigate whether the best Z slice method was working correctly in the experimental data the same setup was simulated within GAMOS. A 662keV source was positioned 2.5cm from the scatterer can (4.6cm from the scatterer crystal) in the simulation and the FWHM in X and Y are plotted against the Z slice to find the best slice for each, this can be seen in Figure 7.8.

These figures show a discrepancy as seen previously for the experimental results, with the source being reconstructed as being closer to the detector than it should be by 2mm using the FWHM in X and 3mm using the FWHM in Y. This is larger than the discrepancy seen for the experimental data in Chapter 5 though this is liable to be due to the model being built from squares and slightly different in shape to the experimental detector. The discrepancy does always show the source being closer to the scatterer than expected, this appears to be a systematic effect that could be caused by the assumption that all interactions take place at the centre point of a voxel within the detector. This places an error on the Z value of 4mm in the scatterer and 10mm in

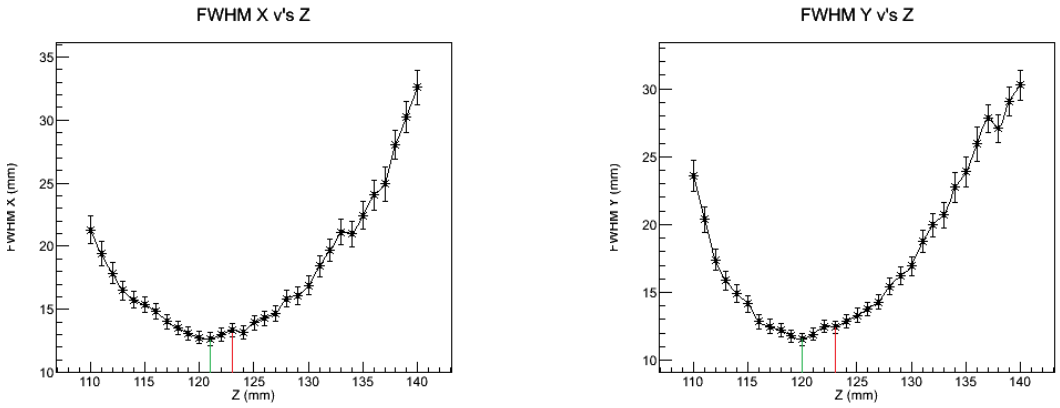

(a) (b)

Figure 7.8: Plot showing the best Z slice for a 662keV source placed 2.5cm from the scatterer can (Z slice 123 in reality). The plots show the best FWHM in X (a) and Y (b) against the best Z slice value. The expected value is marked by a red line, the reconstructed value is marked in green.

the absorber. The effect is more pronounced as the source moves further away, as seen for the experimental data.

7.6 Summary

The simulations carried out in GAMOS allowed a validation to be achieved using the final image resolution at 662keV. The efficiency comparison between the simulated and experimental data shows a large discrepancy with the simulation being larger by a factor of three. Adding in a time factor causes the data sets to match more closely, which indicates that a dead time or pile up issue within the electronics is causing the discrepancy.

The electronics used for the experimental work is not yet fully understood. The trigger algorithms are still in the testing stages, with a timing system that is not understood and the settings on the V1724 have not yet been fully optimised. In particular the MWD shaping time setting is fairly long and the trigger validation window which holds the trigger open for a set length of time has not been optimised for the detector system.

The simulations have also shown that the discrepancy seen in the experimental data where sources are reconstructed to a position closer to the detectors can be repeated in a simulation. This indicates that the assumption that interactions occur in the centre of a voxel will induce an error within the final image by reconstructing the source closer to the detector.

Chapter 8

Conclusion and discussion

For this work a prototype Compton camera was developed in partnership with AWE. This was meant as a proof of concept device, to offer the highest possible energy resolution hence the use of semiconductor detectors and the ability to image across an energy range of 60keV to 1408keV.

Experimental results presented from both Aldermaston and Liverpool have shown the capabilities of a Compton camera system built from two semiconductor double sided strip detectors to produce images across an energy range of 80 to 1408keV. The use of a fully digital trigger system has been implemented alongside the new CAEN V1724 digitisers to allow pulse shapes for each interaction to be stored. This represents the first use of the fully digital system with a two detector Compton camera system.

GAMOS simulations have also shown that the voxel size plays a part in the final image resolution. By applying pulse shape analysis techniques to the experimental data and thereby reducing the size of the voxels the image resolutions will be improved. This application would initially be limited to the absorber detector due to the image charges produced by the silicon scatterer being lost in the noise levels seen. Depth of interaction pulse shape analysis could not be implemented experimentally due to the time constraints. It also could not be simulated due to the GAMOS implementation used to simulate the detectors, it is expected that this could be applied to both detectors and further reduce the image resolution.

By performing work at Aldermaston AWE staff gained experience in the use of research grade detectors and also the new digital electronic acquisition system. AWE also provided access to SNM material, providing the opportunity to image this with the Compton camera system. This is the first time Liverpool has been able to image SNM materials, allowing experience to be gained in particular the measurement with ^{239}Pu highlighted the presence of contaminants from decay products resulting in the addback spectra being difficult to analyse. This experience will provide knowledge for future projects which deal with this kind of material.

Direct comparisons to the existing technologies, in particular the CARTOGAM and

RadScan 800 are difficult due to the lack of independently published results for these systems to confirm the angular resolution and energy range performance quoted by the manufacturers. Ideally side by side comparisons should be carried out using these systems using similar source as used for the Compton camera developed at Liverpool. Images were produced at Liverpool indicating that the system has a 2 pi field of view, the images are effect the further they are away from the centreline of the detector however a method of correcting for the image disparity should be possible with some additional research and comparing the results to optical images. The ability to seperate two different radio nuclides was clearly shown, as was the ability to image diffuse rather than point sources.

8.0.1 Comparison of Aldermaston and Liverpool results

The data taken at both locations cannot be compared directly due to the difference in the setup, with the detector separation being slightly different and also the settings within the electronics being altered following the measurements at Aldermaston. The images taken at Aldermaston do however show that even with an unoptimised setup images can be produced though the low energy range will be limited unless the energy thresholds and baseline offset parameters are set carefully.

The detector seperation will affect the final image resolution, as the detectors are moved apart the final image produced will have an improved FWHM if the same setup is used. Due to the coincidence time window and threshold triggers for each setup being different this effect is not seen in the experimental data.

By using the angular resolution we can compare the results, bearing in mind the detector separation is different. A greater detector separation would normally result in a better image resolution as the vector between the two interaction positions is placed with less error as the detectors are moved apart. Therefore we would expect that the Aldermaston images would have a better resolution than those taken at Liverpool. The ^{152}Eu and ^{133}Ba sources are the only ones which can be compared as these are both point source measurements for both locations.

The angular resolution found between 244 and 964keV for the Aldermaston and Liverpool ^{152}Eu data will be compared, Figure 8.1. The angular resolution removes the source to detector distance dependence however the detectors were further apart at Aldermaston by 2mm compared to the Liverpool setup. The detectors moving further apart should provide a better image resolution. Resolutions presented will be using a 3mm compression in all cases.

This comparison shows the same trends, where the image resolution initially decreases only to increase again as the photopeak energy used increases. This shows that the levels of Compton continuum background seen under the photopeak of interest will play a part in degrading the image.

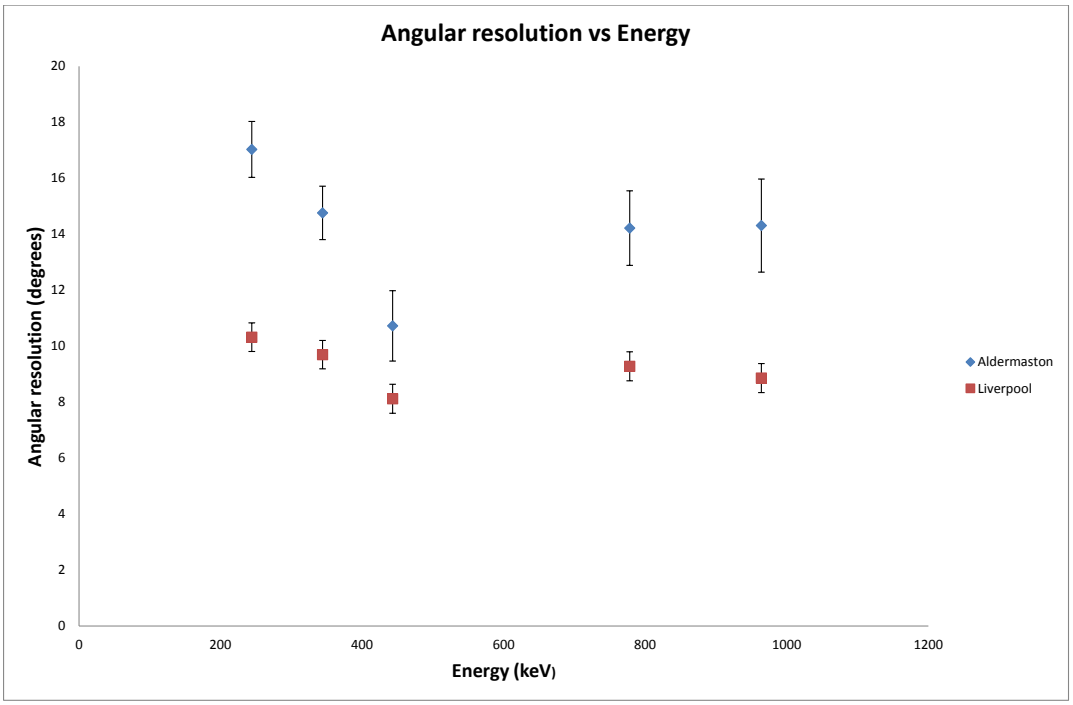

Figure 8.1: A comparison of the angular image resolution found at Aldermaston and Liverpool. This shows that the images produced at Liverpool have a smaller angular image resolution than those taken at Aldermaston.

The image resolutions measured at Aldermaston were expected to be lower in value than those taken at Liverpool, this is not the case. The number of cones used to create the images is significantly lower for the Aldermaston data, this is due to the collection time being restricted and also the poor setup of the system during the measurements. This is indicated by the large error bars in Figure 8.1.

Looking at the summation energy measurements taken, again with a compression factor of 3 we get the results shown in Table 8.1. These results show that the Aldermaston values are consistently higher than those measured at Liverpool indicating that the poor setup had a detrimental effect on the systems image resolution for both a ^{152}Eu and ^{133}Ba point source.

	Aldermaston		Liverpool	
Source	Angular resolution (degrees)	±	Angular resolution (degrees)	±
^{152}Eu	16.1	0.9	9.7	0.5
^{133}Ba	12.7	0.4	10.4	0.2

Table 8.1: Comparison of the angular image resolution measured using peaks from ^{152}Eu and ^{133}Ba at Aldermaston and Liverpool

Comparing the low energy sources we also see a marked difference in the addback spectra. For ^{133}Ba at Aldermaston there is no 80keV peak, yet it is clearly visible in the Liverpool results. Also the addback spectra seen from a ^{57}Co source is distinctly different at lower energies, showing structure at Liverpool which is missing for the Aldermaston spectra. These differences will be due to the threshold settings used, with the arbitrary setting carried out at Aldermaston the lower energies could be below the scatterer threshold, resulting in the loss of this information. Another reason could be the threshold settings at Aldermaston caused a large number of false counts to be recorded due to noise within the detectors, especially the absorber. The large numbers of false readings will have increased the dead time within the system and therefore real events would of been lost.

8.0.2 Energy range

Images have been produced for gamma rays across the energy range of 80 to 1408keV, This range covers the majority of the nuclides of interest to the IAEA and also the UK agencies. ^{241}Am would also be of interest but its main gamma ray emission is at 60keV, below the limit measured with the current Compton camera system. This is due to the noise levels seen within the scatterer being around 9keV with the digital system, a Compton scatter from a 60keV gamma ray would deposit between 2 and 12keV to produce an angle which would allow the scattered gamma ray to interact in the absorber. This means that the noise levels will prevent images being produced for ^{241}Am. Reducing the noise levels could mean that imaging ^{241}Am would be possible.

The image produced for 80keV from a ^{133}Ba source showed that imaging low energy gamma rays with this technique is difficult. The Compton background present from higher energy peaks results in a low peak to total ratio for the photopeak of interest, so placing an energy gate on the peak will introduce a large number of events which are not truly fully absorbed fold 1,1,1,1 interactions. The resulting image must therefore also use an angle gate, though angles must be chosen carefully so the image can be produced. Angle gating reduces the number of cones significantly at lower energies and some of the extraneous events need to be included to provide enough background for the image to be visible, hence the use here of a 0 to 130 degree angle gate.

8.0.3 Efficiency

The efficiency measurements carried out at Liverpool and the GAMOS simulations highlighted some issues. By comparing the two it is shown that an effect similar to dead time is occurring with the experimental data and events are being lost within the electronics. The use of a brand new trigger mask which has time characteristics that are yet to be fully explored alongside brand new digital electronics which are also not fully understood seem to be the cause of this. A fairly long shaping time is also used on the V1724's, 6.5μs, this could also be causing data to be lost due to pile up events as the cards will reject any events which occur within the time it takes to shape each pulse.

An investigation must be undertaken into the data loss as the systems current lower than expected efficiency will cause problems if shielded material was to be imaged and also at stand off distances. The time taken to take a measurement which can provide both the identiity and position of the source is key, a low efficiency will result in the detector taking longer to produce the desired results. This is especially true for stand off distances >1m which is closer to the real world application.

Timing issues

The factor of data loss seen when the experimental results where compared to the GAMOS simulations was 3 times. This is a large quantity of data which if recovered would increase the efficiency of the detector system and allow shorter counting times to be used to gain the same statistics. The issue appears to be in the timing of the system, within either the trigger mask or the shaping time of the moving window deconvolution energy measurement causing event pile up.

A digital system in theory has no dead time, however pile up can occur if the MWD shaping time is set to long, resulting in events piling up while the pulses are processed. This effect will cause events to be discarded as all pile up events are not recorded within the data stream. The reading out of traces for each channel will also include a dead time, this was estimated in Chapter 5 though this estimate was not done for all of the

channels.

The timing involved in the trigger mask applied to the data has not been tested. The settings were initially set to values which allowed the system to work in Compton mode, the only setting that was adjusted after the work started was the coincidence time window. The other settings which control how long the trigger pulse is kept open and the timing of the trigger logic itself require further investigation before they are fully understood.

To investigate the cause of the timing issues it is recommended that each cause should be isolated and tested individually. This can be achieved by

1. altering the shaping time to a lower value and keeping all other settings the same, this should give an indication of the pile up caused with different shaping times.

2. comparing the amount of data collected using an analogue trigger system with the V1724's compared to the amount of data collected using the fully digital system. This should highlight any timing issues with the digital trigger mask and if there are any the settings can be altered to minimise the difference between the analogue and digital triggers.

3. compare a fully analogue system with the fully digital system. This will build in all the timing factors involved in the digital system and should provide a good measure of the total dead time caused by all of the components.

Once the dead time is fully understood the actual efficiency of the system can then be measured and used to provide a minimum detectable level for different gamma ray energies. This value provides the minimum activity of a known gamma ray which can be detected by the system to a 95% certainty.

8.0.4 Image reconstruction

Good images have been produced over a wide energy range, from 80 to 1408keV. The addback spectra of the data shows good spectroscopic separation of the incident gamma rays. The images produced were reconstructed within positioning errors to the expected position. The Aldermaston data sets contain more placement error due to the methods used for source position when compared to the Liverpool data sets.

A pin cushioning effect is shown when the source is positioned away from the centre of the scatterer. This effect is not yet fully understood but has been shown to be energy independent with the use of different sources. Image compression was utilised to overcome the statistical limitations seen within the data collected. The use of compression will limit the final image resolution measured due to the image bin size being a factor in the measurements made.

The peak to total ratio for the peak selected will dictate the available number of cones for reconstruction and the broadening of the image that is introduced by the events within the energy gate that are not fully absorbed fold 1,1,1,1. If the energy of the incident gamma ray is low, 80 to 200keV, the energy deposited by a Compton scatter within the scatterer will have a large noise contribution. The noise levels seen in the scatterer are around 9keV, so a typical deposit of 20keV in this detector from a low energy gamma ray will have $\sim 50\%$ contribution from noise broadening the image. Compare this to the 100keV deposits or more expected from higher energy gamma rays where the noise contribution will be greatly reduced as a percentage of the total deposit.

The image reconstruction code used within this work is a simple back projection method. This code provides a quick method to produce images but an iterative approach will produce images with better resolution due to the methods used. An iterative code is being written at the University of Liverpool and will be applied to this data once it is ready for use, this should give a better quality image however it will require more time to produce the images.

8.0.5 Discussion

To deploy a Compton camera system in the field the unit would need to be compact and easy to use. This would require the detectors to be mounted within one unit and the associated electronics to be as compact as possible. Cryogenically cooled detectors can be combined into one single cryostat to make the system more compact but would require the use of liquid nitrogen or mechanical cooling which would add additional complications. The use of semiconductor materials which do not require cooling such as CZT removes the cooling requirement though currently the energy resolution of these materials does not match that of HPGe so images would produced would have a poorer image resolution.

Two detectors are also limited as there is still a large Compton continuum seen in low energy peaks if higher energy gamma rays are present. This could be overcome by providing a veto screen around the Compton camera, using additional high efficiency detectors such as BGO or NaI scintillators. By using this Compton expression system the continuum can be reduced by removing events from the addback spectra which are coincident with the suppression detectors, thus only recording data which interacts within the two main detectors. Additional detectors can also be stacked behind the absorber, this offers the possibility of covering a wider range of energies with one detector system, combining different semiconductor materials and/or thickness's to optimise the device across a wide range of energies. By using a stack of detectors the addback spectra should also be cleaned up and more events should be fully absorbed within the greater thickness of material used.

Using only fold 1,1,1,1 events reduces the statistics available. By looking at higher fold events it may be possible to increase the statistics though the larger uncertainty over which interaction occurs first will introduce an error into the image. Investigations need to be carried out on the feasibility of using higher fold events as there is a difficulty in locating the first interaction point within the detectors.

Appendix A

Experimental images taken in Liverpool

A.1 ^{152}Eu Images

Experimental images from a ^{152}Eu source measured at Liverpool. Energy gates have been applied to each individual photopeak and the images produced are shown here. The images presented all have a compression of 3mm to provide comparison to those taken at Aldermaston.

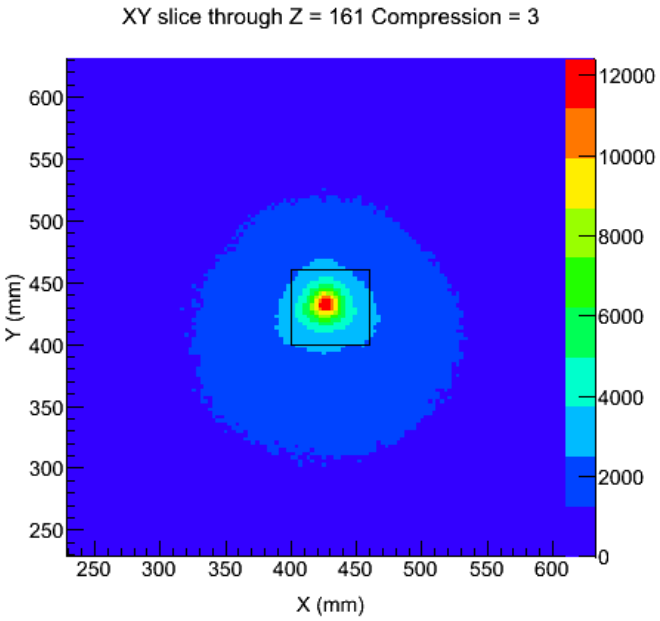

(a)

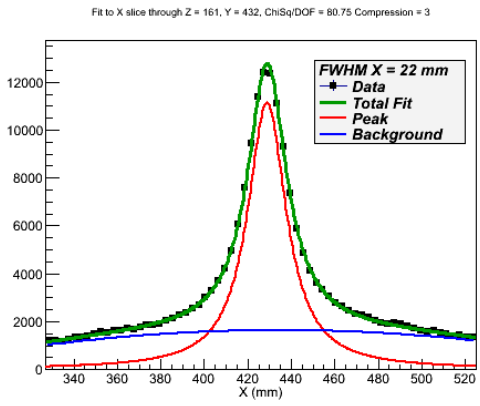

(b)

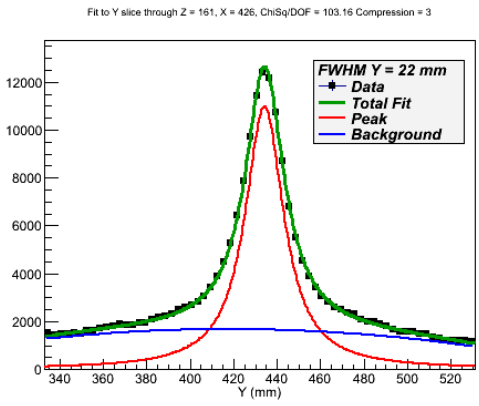

(c)

Figure A.1: The image produced by gating on the 244keV γ ray transition is shown in (a). The average FWHM of the image is 21.7mm $\pm$ 1.1mm. (b) and (c) are cross sections through the X and Y axis respectively, showing the Lorentzian fit to the data used to create the image.

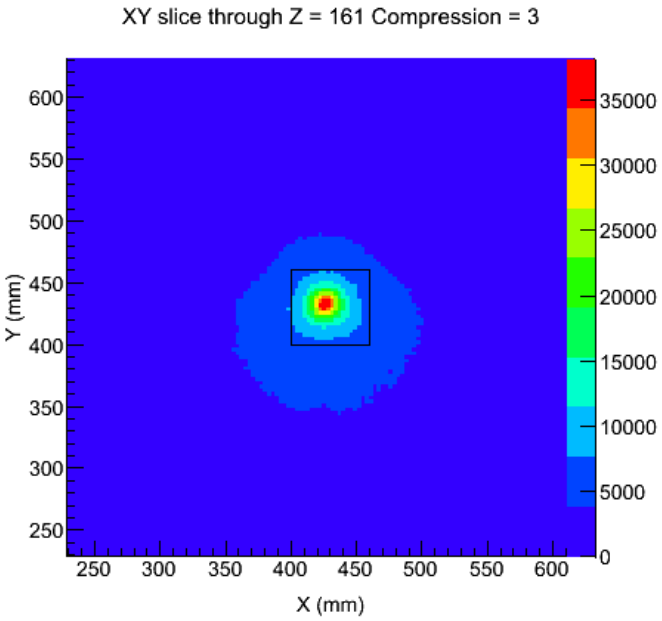

(a)

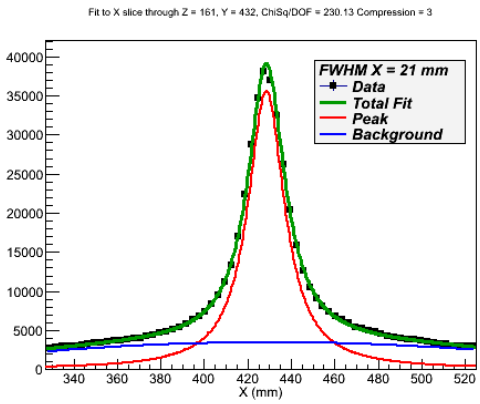

(b)

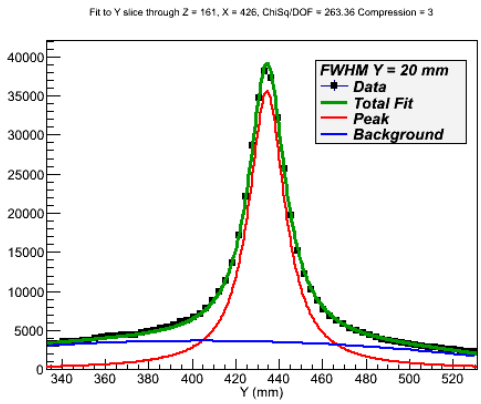

(c)

Figure A.2: The image produced by gating on the 344keV γ ray transition is shown in (a). The average FWHM of the image is 20.4mm $\pm$ 1.1mm. (b) and (c) are cross sections through the X and Y axis respectively, showing the Lorentzian fit to the data used to create the image.

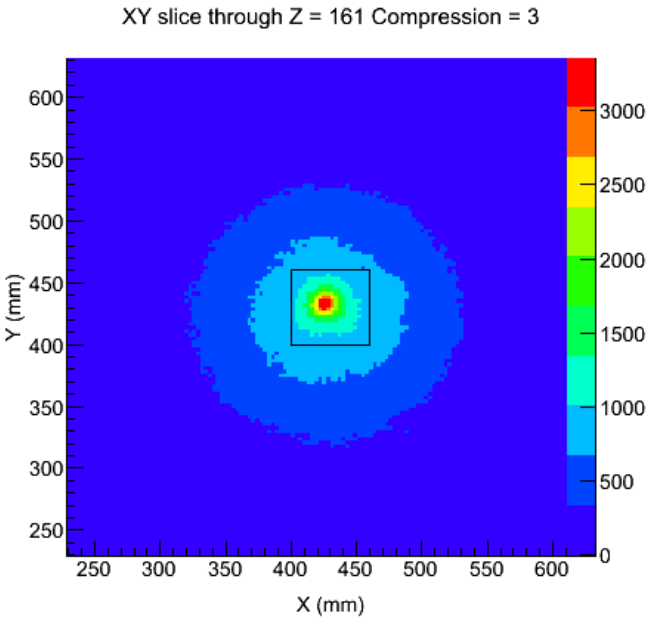

(a)

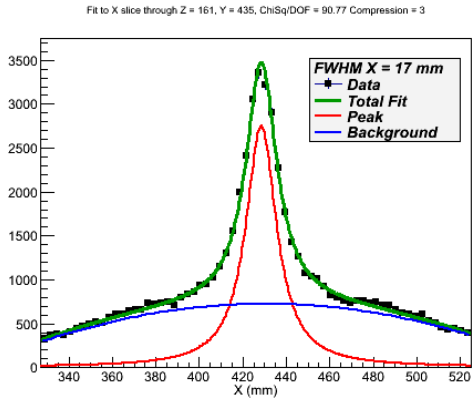

(b)

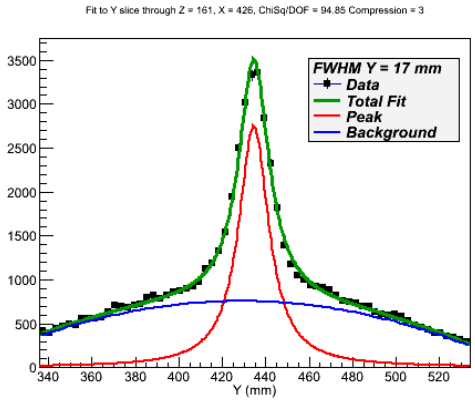

(c)

Figure A.3: The image produced by gating on the 443keV γ ray transition is shown in (a). The average FWHM of the image is 17.0mm $\pm$ 1.1mm. (b) and (c) are cross sections through the X and Y axis respectively, showing the Lorentzian fit to the data used to create the image.

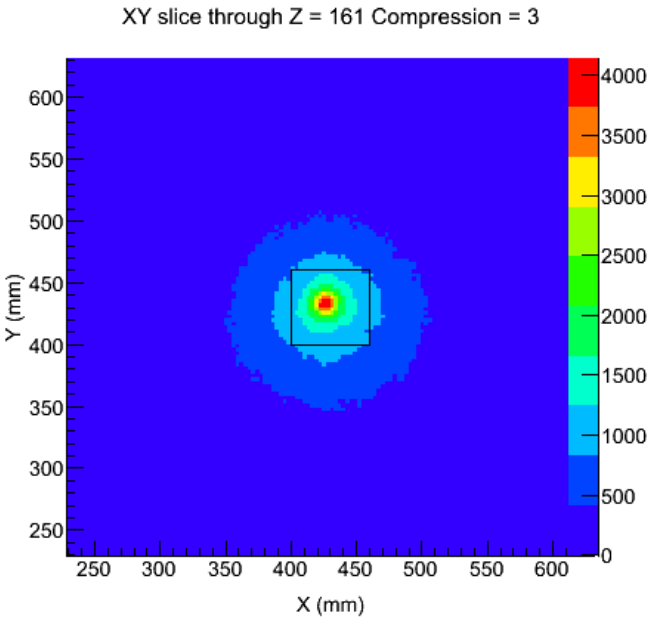

(a)

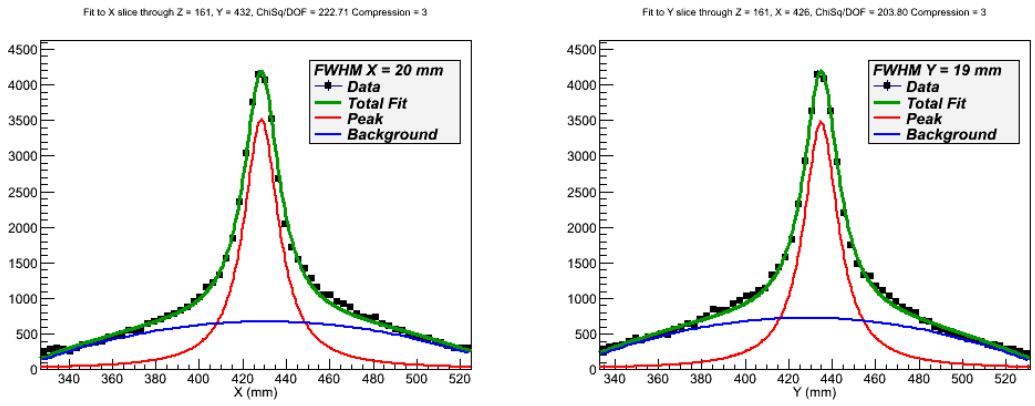

(b) (c)

Figure A.4: The image produced by gating on the 778keV γ ray transition is shown in (a). The average FWHM of the image is 19.5mm $\pm$ 1.1mm. (b) and (c) are cross sections through the X and Y axis respectively, showing the Lorentzian fit to the data used to create the image.

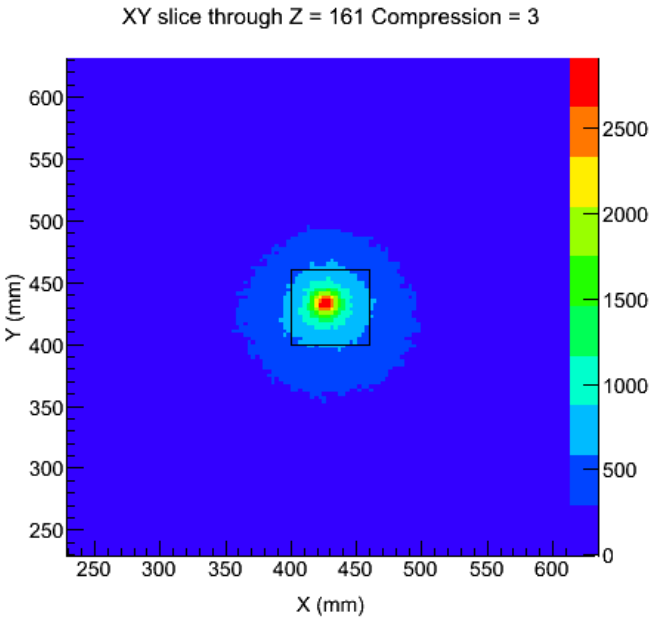

(a)

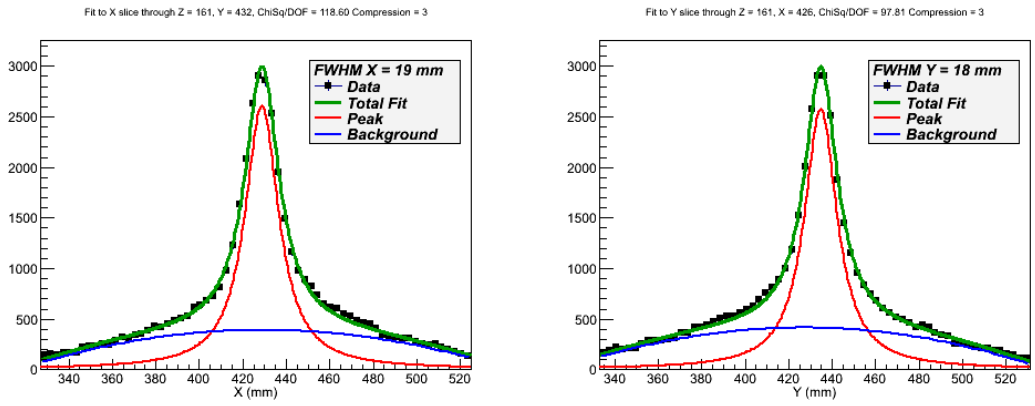

(b) (c)

Figure A.5: The image produced by gating on the 964keV γ ray transition is shown in (a). The average FWHM of the image is 18.6mm $\pm$ 1.1mm. (b) and (c) are cross sections through the X and Y axis respectively, showing the Lorentzian fit to the data used to create the image.

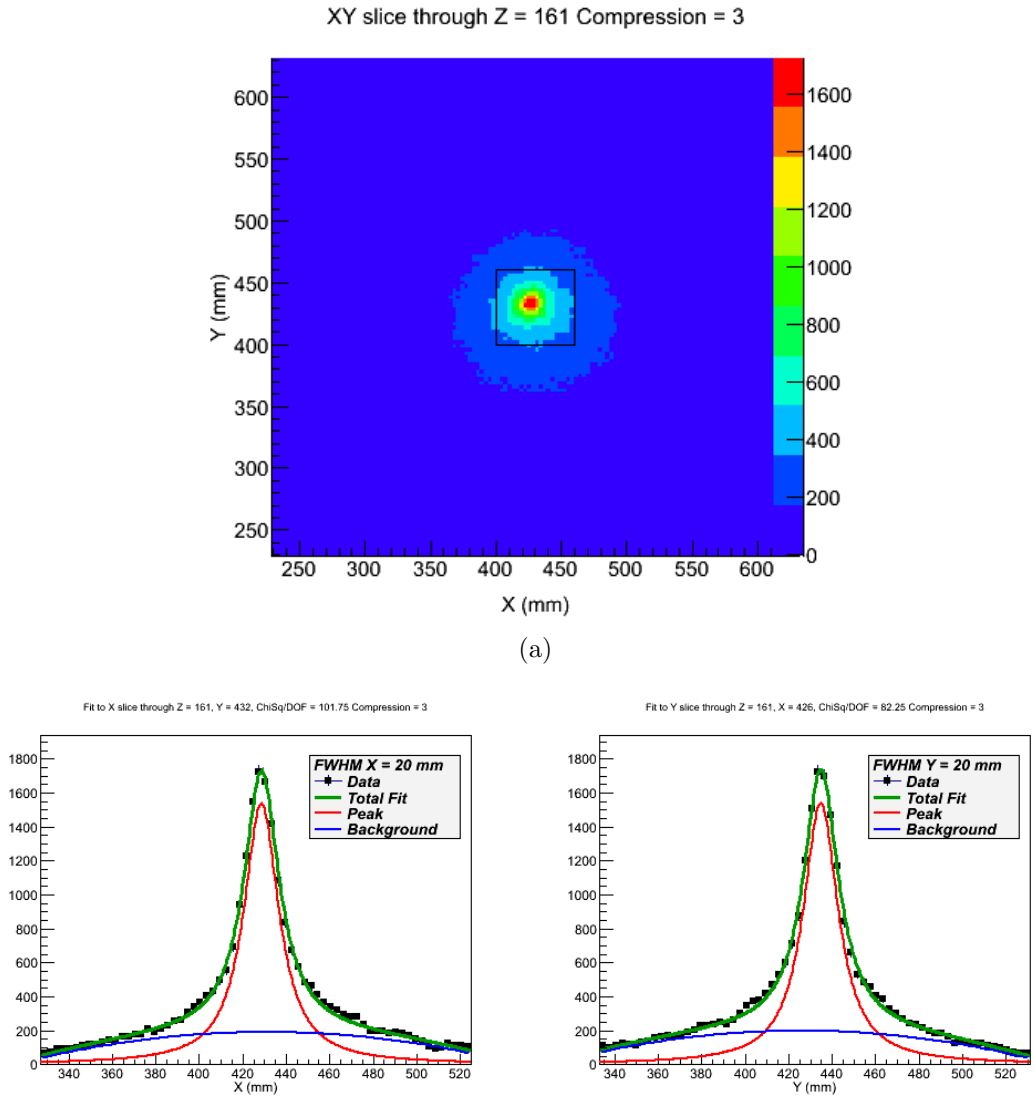

(a)

(b)

(c)

Figure A.6: The image produced by gating on the 1112keV γ ray transition is shown in (a). The average FWHM of the image is 19.6mm $\pm$ 1.1mm. (b) and (c) are cross sections through the X and Y axis respectively, showing the Lorentzian fit to the data used to create the image.

Appendix B

Experimental images taken in Aldermaston

B.1 ^{152}Eu Images

Experimental images produced from the ^{152}Eu data taken at Aldermaston, with each photopeak being imaged separately.

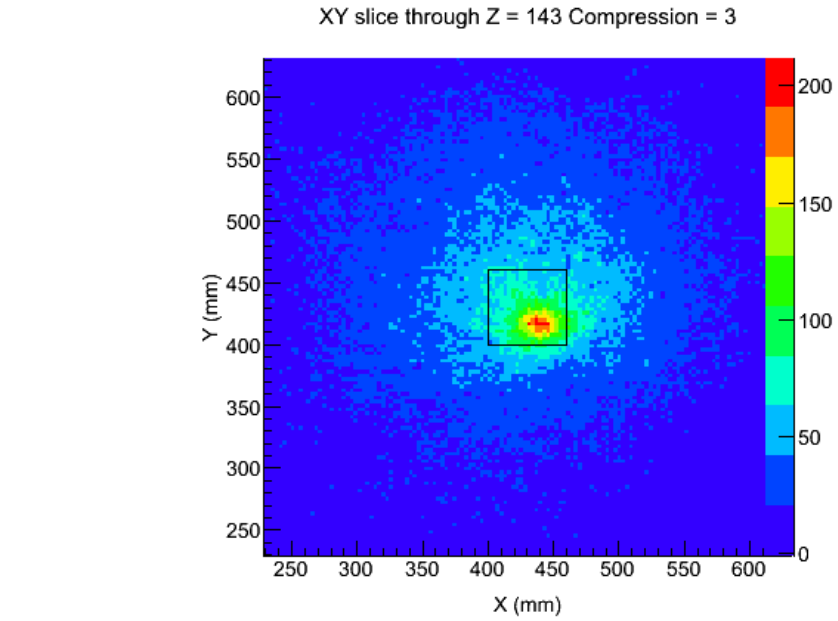

(a)

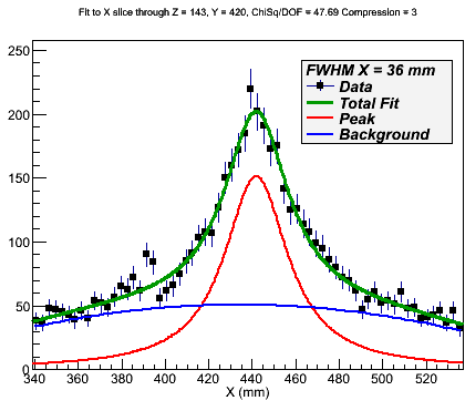

(b)

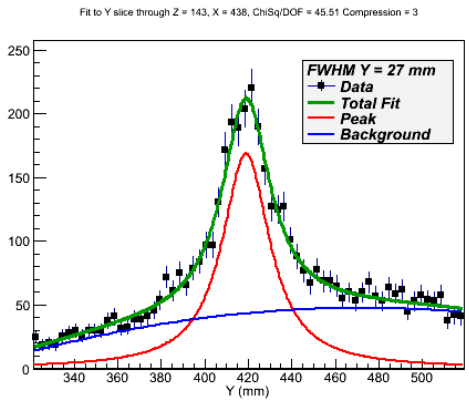

(c)

Figure B.1: The image produced by gating on 122keV γ ray transition is shown in (a). The average FWHM of the image is 30.8mm $\pm$ 1.8mm. (b) and (c) are cross sections through the X and Y axis respectively, showing the Laplacian fit to the data used to create the image.

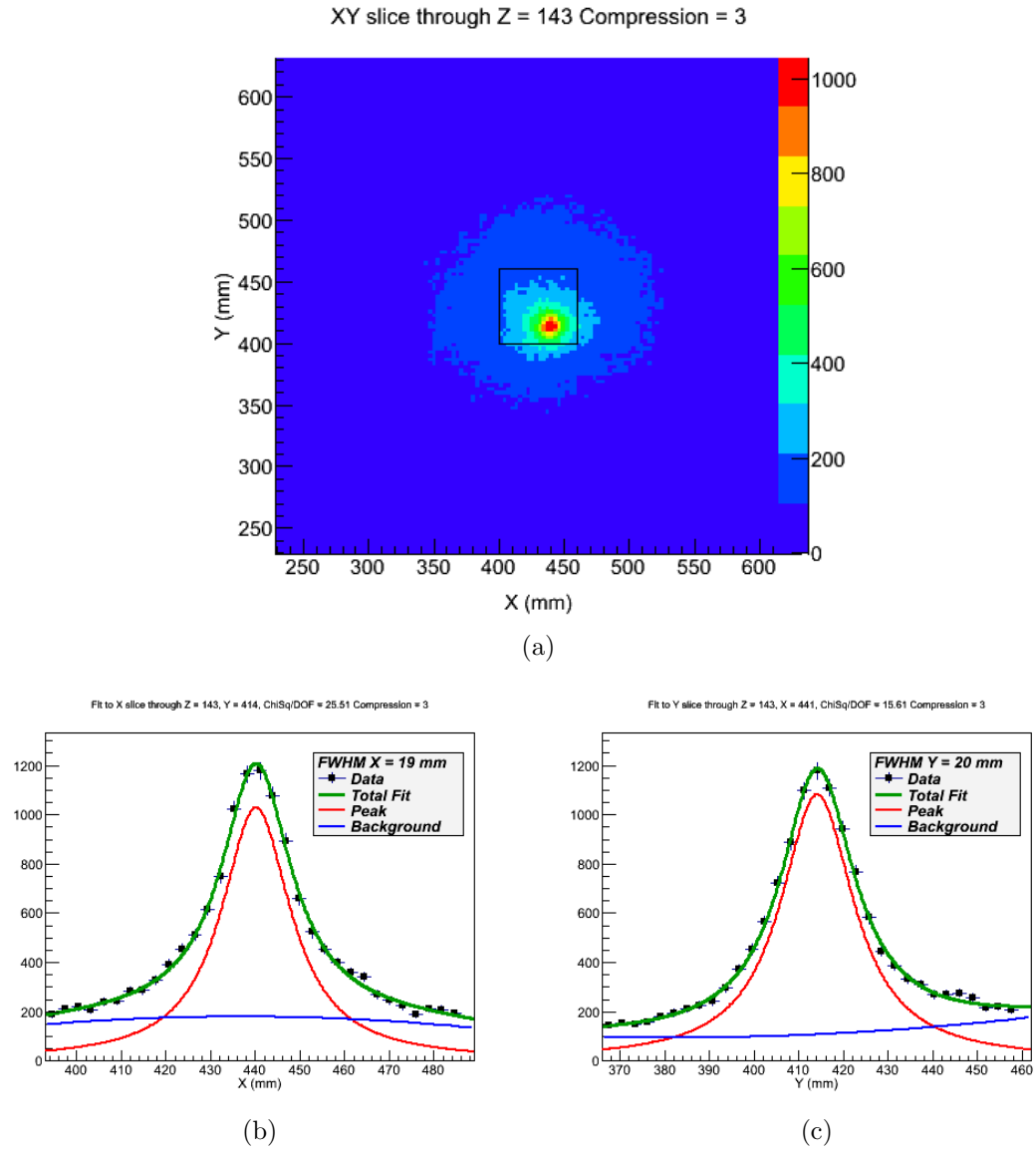

(a)

(b)

(c)

Figure B.2: The image produced by gating on 244keV γ ray transition is shown in (a). The average FWHM of the image is 20.4mm $\pm$ 1.2mm. (b) and (c) are cross sections through the X and Y axis respectively, showing the Laplacian fit to the data used to create the image.

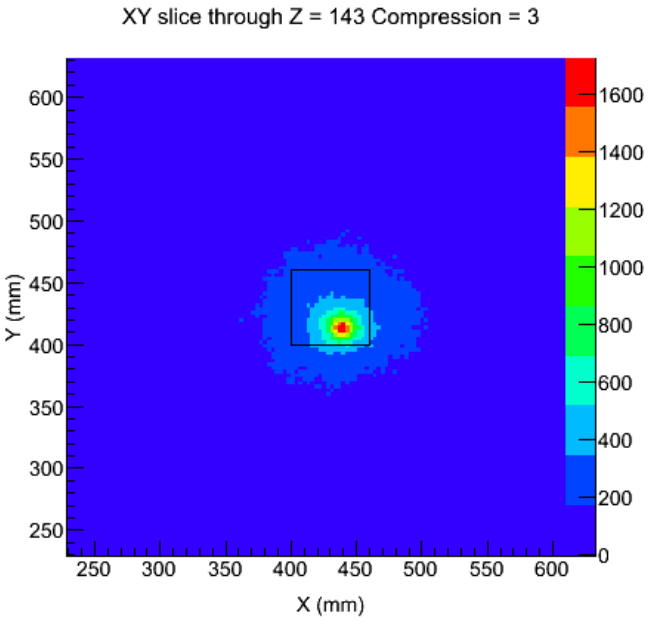

(a)

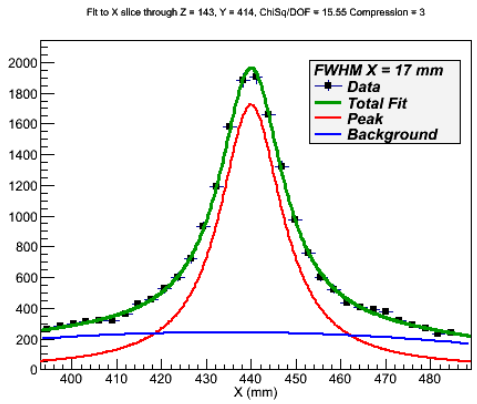

(b)

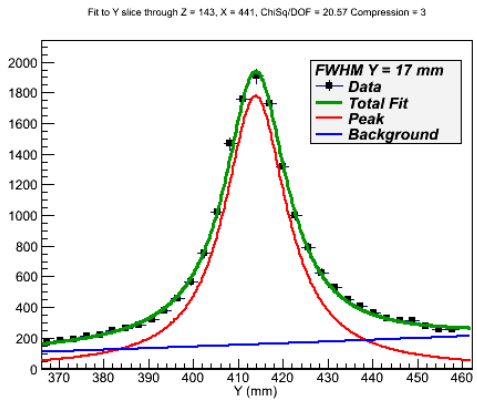

(c)

Figure B.3: The image produced by gating on 344keV γ ray transition is shown in (a). The average FWHM of the image is 17.6mm $\pm$ 1.1mm. (b) and (c) are cross sections through the X and Y axis respectively, showing the Laplacian fit to the data used to create the image.

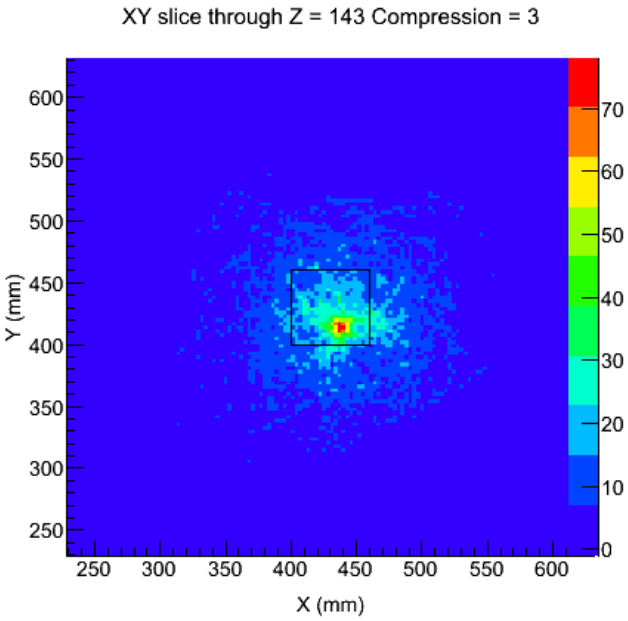

(a)

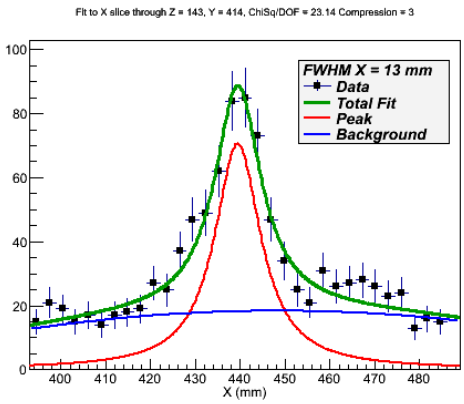

(b)

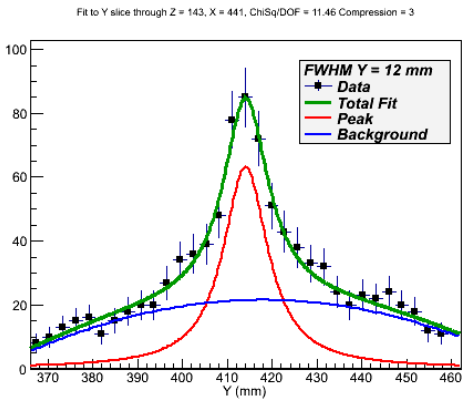

(c)

Figure B.4: The image produced by gating on 443keV γ ray transition is shown in (a). The average FWHM of the image is 12.8mm $\pm$ 1.5mm. (b) and (c) are cross sections through the X and Y axis respectively, showing the Laplacian fit to the data used to create the image.

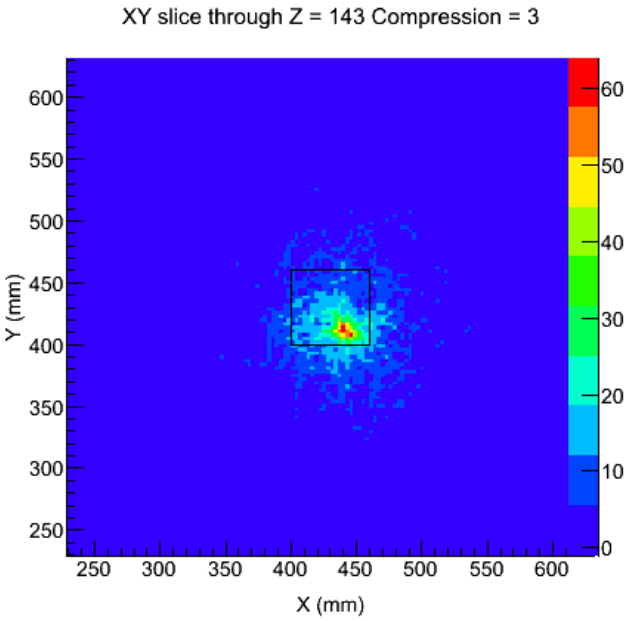

(a)

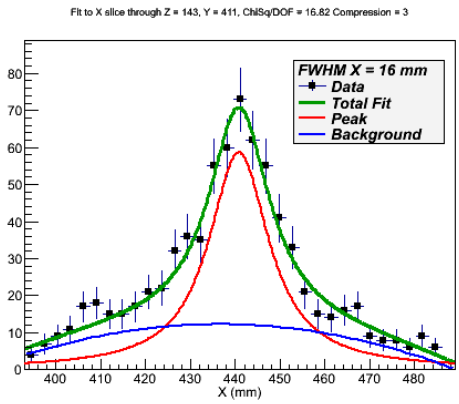

(b)

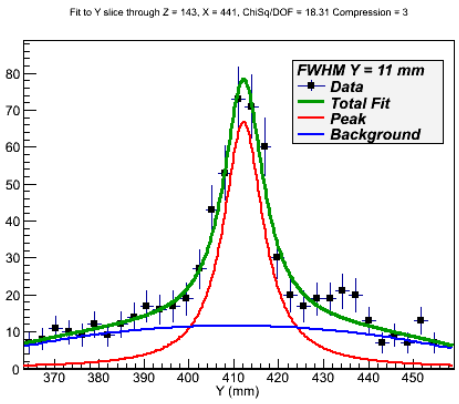

(c)

Figure B.5: The image produced by gating on 778keV γ ray transition is shown in (a). The average FWHM of the image is 17.0mm $\pm$ 1.6mm. (b) and (c) are cross sections through the X and Y axis respectively, showing the Laplacian fit to the data used to create the image.

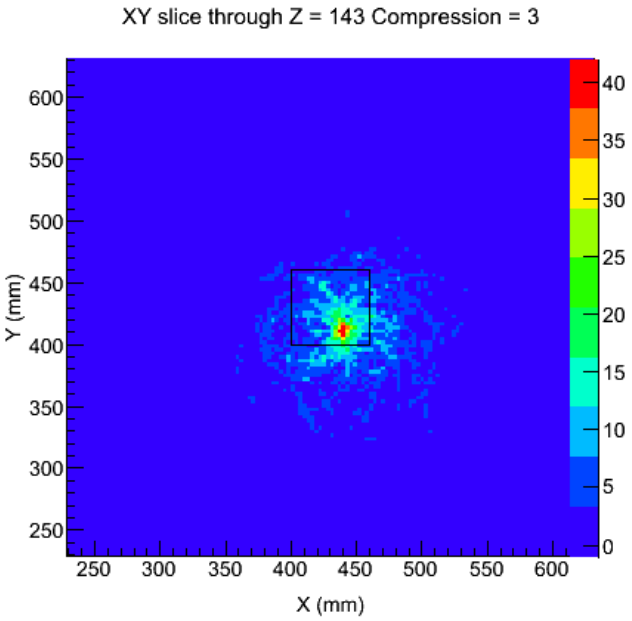

(a)

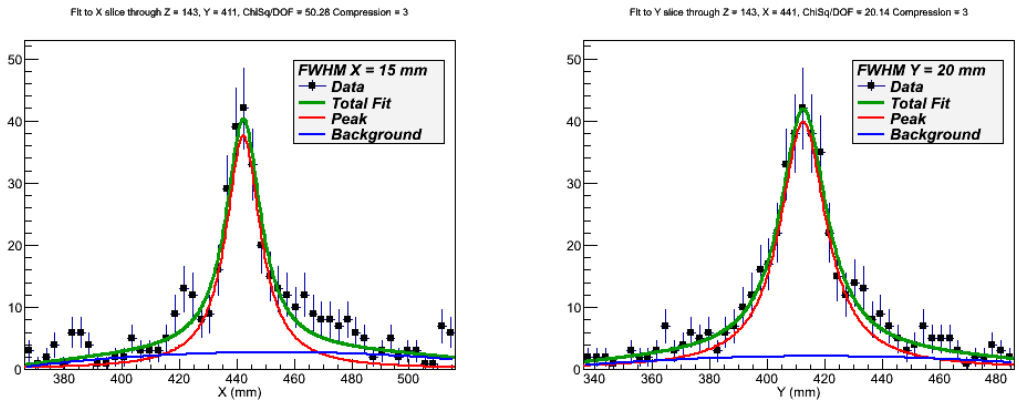

(b) (c)

Figure B.6: The image produced by gating on 964keV γ ray transition is shown in (a). The average FWHM of the image is 17.1mm $\pm$ 2.0mm. (b) and (c) are cross sections through the X and Y axis respectively, showing the Laplacian fit to the data used to create the image.

Appendix C

Branching ratios of multiple gamma ray sources

To show the relative intensities of the source used within this work that emit multiple gamma rays the branching ratios for each energy are presented here. All data presented here is taken from [46], only the peaks used within this work are included here, please see the reference for information on any other gamma rays emitted by the sources.

^{57}Co	
Energy (keV)	Branching ratio (%)
122.0612	85.5
136.4730	10.69

Table C.1: Branching ratios of the gamma ray energies emitted by ^{57}Co.

^{133}Ba	
Energy (keV)	Branching ratio (%)
80.989	34.2
276.388	7.09
302.851	18.4
355.999	62.2
383.841	8.92

Table C.2: Branching ratios of the gamma ray energies emitted by ^{133}Ba.

^{152}Eu	
Energy (keV)	Branching ratio (%)
121.7758	28.4
244.6923	7.51
344.286	26.6
443.894	2.80
778.920	12.98
964.110	14.5
1112.075	13.6
1408.002	20.8

Table C.3: Branching ratios of the gamma ray energies emitted by ^{152}Eu.

^{22}Na	
Energy (keV)	Branching ratio (%)
511	190
1274	99.937

Table C.4: Branching ratios of the gamma ray energies emitted by ^{22}Na.

^{235}U	
Energy (keV)	Branching ratio (%)
143.786	10.5
163.379	4.7
185.739	53.0
205.333	4.7

Table C.5: Branching ratios of the gamma ray energies emitted by ^{235}U.

^{239}Pu	
Energy (keV)	Branching ratio (%)
203.52	0.000560
332.81	0.000505
344.94	0.00057
375.018	0.00158
413.691	0.00151
451.44	0.000192

Table C.6: Branching ratios of the gamma ray energies emitted by ^{239}Pu.

Bibliography

[1] International Atomic Energy Authority. Measures against illicit trafficking in nuclear materials and other radioactive sources. `http://www.iaea.org/About/Policy/GC/GC40/Documents/gc40-15.html`, August 1996.

[2] R.W. Todd, J.M. Nightingale, and D.B. Everett. A proposed γ camera. *Nature*, 251(1):132 – 134, 1974.

[3] V. Schnfelder, A. Hirner, and K. Schneider. A telescope for soft gamma ray astronomy. *Nuclear Instruments and Methods*, 107(2):385 – 394, 1973.

[4] L.J. Harkness et al. Semiconductor detectors for Compton imaging in nuclear medicine. *Journal of Instrumentation*, 7, 2012.

[5] L. Mihailescu, K.M. Vetter, M.T. Burks, E.L. Hull, and W.W. Craig. SPEIR: A Ge Compton camera. *Nuclear Instruments and Methods in Physics Research Section A: Accelerators, Spectrometers, Detectors and Associated Equipment*, 570(1):89 – 100, 2007.

[6] K Hughes and S Walker. The use of a gamma ray imaging device for in cell assay. In *Proc. of WM2008 conference*, volume Feb 24-28, 2008.

[7] A Fisher and P Chard. Use of a gamma-imaging device to optimise measurement of uranium hold-up. In *Proc. of the 25th annual safeguards research and development association ESARDA symposium on safeguards and nuclear materials management, Stockholm*, 2003.

[8] S Hepworth and P Griffiths. Remote two dimensional gamma imaging of wide area high dose environments using the radscan 800 4pi gamma imager. In *Proc of 10th international conference on environmental remediation and radioactive waste management*, volume Sep 4-8, 2005.

[9] Olivier Gal, Mehdi Gmar, Oleg P. Ivanov, Frdric Lain, Fabrice Lamadie, Christophe Le Goaller, Charly Mah, Erwan Manach, and Vyacheslav E. Stepanov. Development of a portable gamma camera with coded aperture. *Nuclear Instruments and Methods in Physics Research Section A: Accelerators, Spectrometers,*

Detectors and Associated Equipment, 563(1):233 – 237, 2006. Proceedings of the 7th International Workshop on Radiation Imaging Detectors {IWORID} 2005 7th International Workshop on Radiation Imaging Detectors.

[10] V. Schnfelder. The imaging gamma-ray telescope {COMPTEL} aboard {GRO}. *Advances in Space Research*, 11(8):313 – 322, 1991.

[11] TEPCO. Measurement of environmental radiation distribution in kusano, iidate village. `http://www.jaxa.jp/press/2012/03/20120329_compton_2_e.pdf`, Feb 2012.

[12] K.S. Krane. *Introductory Nuclear Physics*. John Wiley & Sons, first edition, 1988.

[13] R.D. Evans. *The Atomic Nucleus*. McGraw-Hill Book Company, first edition, 1955.

[14] C.E. Ordonez, A. Bolozdynya, and W. Chang. Doppler broadening of energy spectra in Compton cameras. In *Nuclear Science Symposium, 1997. IEEE*, volume 2, pages 1361 –1365 vol.2, nov 1997.

[15] G. Knoll. *Radiation Detection and Modelling*. John Wiley & Sons, fourth edition, 2010.

[16] S.M. Sze. *Semiconductor devices Physics and technology*. John Wiley & Sons, first edition, 1985.

[17] H.P. Myers. *Introductory Solid State Physics*. Taylor and Francis, second edition, 1997.

[18] L Mihailescu, W Gast, R.M Lieder, H Brands, and H Jger. The influence of anisotropic electron drift velocity on the signal shapes of closed-end HPGe detectors. *Nuclear Instruments and Methods in Physics Research Section A: Accelerators, Spectrometers, Detectors and Associated Equipment*, 447(3):350 – 360, 2000.

[19] Hans R. Bilger. Fano factor in germanium at 77k. *Phys. Rev.*, 163:238–253, Nov 1967.

[20] W. Shockley. Currents to conductors induced by a moving point charge. *Journal of Applied Physics*, 9(10):635 –636, oct 1938.

[21] S. Ramo. Currents induced by electron motion. *Proceedings of the IRE*, 27(9):584 – 585, sept. 1939.

[22] Zhong He. Review of the ShockleyRamo theorem and its application in semiconductor gamma-ray detectors. *Nuclear Instruments and Methods in Physics*

Research Section A: Accelerators, Spectrometers, Detectors and Associated Equipment, 463(12):250 – 267, 2001.

[23] V. Radeka. Low noise techniques in detectors. *Annual Review of Nuclear and Particle Science,*, 38:217–277, 1988.

[24] F.C.L. Crespi, F. Camera, O. Wieland, G. Benzoni, S. Brambilla, B. Million, and D. Montanari. A pulse shape analysis algorithm for HPGe detectors. *Nuclear Instruments and Methods in Physics Research Section A: Accelerators, Spectrometers, Detectors and Associated Equipment*, 570(3):459 – 466, 2007.

[25] R.J. Cooper, A.J. Boston, H.C. Boston, J.R. Cresswell, A.N. Grint, A.R. Mather, P.J. Nolan, D.P. Scraggs, G. Turk, C.J. Hall, I. Lazarus, A. Berry, T. Beveridge, J. Gillam, and R.A. Lewis. SmartPET: Applying HPGe and pulse shape analysis to small-animal PET. *Nuclear Instruments and Methods in Physics Research Section A: Accelerators, Spectrometers, Detectors and Associated Equipment*, 579(1):313 – 317, 2007.

[26] E. Rutherford and H. Geiger. An electrical method of counting the number of α-particles from radioactive substances. *Proceedings of the royal society of London*, 81(546):141 – 161, 1908.

[27] Rapiscan systems. Portal monitors. `http://tsasystems.com/products/portal.html`, Feb 2012.

[28] Ortec. Handheld radio-isotope identification device (RIIDS). `http://www.ortec-online.com/Solutions/homeland-security.aspx?tab=3`, Feb 2012.

[29] Ortec. Nai-ss gamma and neutron search systems. `http://www.ortec-online.com/Solutions/homeland-security.aspx?tab=3`, Feb 2012.

[30] Smith's detection. Radseeker, handheld radioisotope identifier. `http://www.smithsdetection.com/RadSeeker.php`, Feb 2012.

[31] VT Nuclear services. Radscan 800, 4 π gamma imager. `http://www.pbcasia.com.cn/datasheets/bci/RadScan.pdf`, Feb 2012.

[32] K.P. Ziock. Gamma ray imaging spectrometry. `https://www.llnl.gov/str/pdfs/10_95.2.pdf`, Feb 2012.

[33] K.P. Ziock, editor. *A Mechanically-Cooled Highly-Portable HPGe-Based Coded-Aperture Gamma-Ray Imager*, July 2010.

[34] D.S. Judson, A.J. Boston, P.J. Coleman-Smith, D.M. Cullen, A. Hardie, L.J. Harkness, L.L. Jones, M. Jones, I. Lazarus, P.J. Nolan, V. Pucknell, S.V. Rigby,

P. Seller, D.P. Scraggs, J. Simpson, M. Slee, and A. Sweeney. Compton imaging with the PorGamRays spectrometer. *Nuclear Instruments and Methods in Physics Research Section A: Accelerators, Spectrometers, Detectors and Associated Equipment*, 652(1):587 – 590, 2011. Symposium on Radiation Measurements and Applications (SORMA) XII 2010.

[35] J.W. LeBlanc, N.H. Clinthorne, C.-H. Hua, E. Nygard, W.L. Rogers, D.K. Wehe, P. Weilhammer, and S.J. Wilderman. C-SPRINT: a prototype Compton camera system for low energy gamma ray imaging. *Nuclear Science, IEEE Transactions on*, 45(3):943 –949, jun 1998.

[36] G.L Zeng. Image reconstruction a tutorial. *Computerized Medical Imaging and Graphics*, 25(2):97 – 103, 2001.

[37] Philippe P Bruyant. Analytic and iterative reconstruction algorithms in SPECT. *Journal of Nuclear Medicine*, 43(10):1343–1358, 2002.

[38] L.J. Harkness, D.S. Judson, A.J. Boston, H.C. Boston, J.R. Cresswell, P.J. Nolan, A. Sweeney, J. Beau, M. Lampert, B. Pirard, and M. Zuvic. Characterisation of a Si(Li) orthogonal-strip detector. *Nuclear Instruments and Methods in Physics Research Section A: Accelerators, Spectrometers, Detectors and Associated Equipment*, 726(0):52 – 59, 2013.

[39] R.J. Cooper, A.J. Boston, H.C. Boston, J.R. Cresswell, A.N. Grint, L.J. Harkness, P.J. Nolan, D.C. Oxley, D.P. Scraggs, A.R. Mather, I. Lazarus, and J. Simpson. Positron emission tomography imaging with the SmartPET system. *Nuclear Instruments and Methods in Physics Research Section A: Accelerators, Spectrometers, Detectors and Associated Equipment*, 606(3):523 – 532, 2009.

[40] DC Oxley, AJ Boston, HC Boston, JR Cresswell, AN Grint, LJ Harkness, M Jones, DS Judson, PJ Nolan, M Slee, et al. A semiconductor-based positron emission tomography system. In *AIP Conference Proceedings*, volume 1194, page 96, 2009.

[41] R.J. Cooper, A.J. Boston, H.C. Boston, J.R. Cresswell, A.N. Grint, L.J. Harkness, P.J. Nolan, D.C. Oxley, D.P. Scraggs, I. Lazarus, J. Simpson, and J. Dobson. Charge collection performance of a segmented planar high-purity germanium detector. *Nuclear Instruments and Methods in Physics Research Section A: Accelerators, Spectrometers, Detectors and Associated Equipment*, 595(2):401 – 409, 2008.

[42] R.J. Cooper, G. Turk, A.J. Boston, H.C. Boston, J.R. Cresswell, A.R. Mather, P.J. Nolan, C.J. Hall, I. Lazarus, J. Simpson, A. Berry, T. Beveridge, J. Gillam, and R.A. Lewis. Position sensitivity of the first SmartPET HPGe detector. *Nuclear*

Instruments and Methods in Physics Research Section A: Accelerators, Spectrometers, Detectors and Associated Equipment, 573(12):72 – 75, 2007.

[43] H.C. Boston, A.J. Boston, R.J. Cooper, J. Cresswell, A.N. Grint, A.R. Mather, P.J. Nolan, D.P. Scraggs, G. Turk, C.J. Hall, I. Lazarus, A. Berry, T. Beveridge, J. Gillam, and R. Lewis. Characterisation of the SmartPET planar germanium detectors. *Nuclear Instruments and Methods in Physics Research Section A: Accelerators, Spectrometers, Detectors and Associated Equipment*, 579(1):104 – 107, 2007.

[44] CAEN. V1724 8 channel 14 bit 100ms/s digitizer. `http://www.caen.it/csite/CaenProd.jsp?idmod=483&parent=11`, July 2013.

[45] CAEN. V1495 general purpose VME board. `http://www.caen.it/csite/CaenProd.jsp?idmod=484&parent=11`, July 2013.

[46] E. Browne and R.B. Firestone. *Table of radioactive isotopes*. John Wiley & Sons, first edition, 1986.

[47] Dirk P. Kroese and Reuven Y. Rubinstein. Monte Carlo methods. *Wiley Interdisciplinary Reviews: Computational Statistics*, 4(1):48–58, 2012.

[48] Pedro Arce, Pedro Rato, Mario Canadas, and Juan Ignacio Lagares. GAMOS: A Geant4-based easy and flexible framework for nuclear medicine applications. In *Nuclear Science Symposium Conference Record, 2008. NSS '08. IEEE*, pages 3162 –3168, oct. 2008.

[49] S. Agostinelli et al. Geant4a simulation toolkit. *Nuclear Instruments and Methods in Physics Research Section A: Accelerators, Spectrometers, Detectors and Associated Equipment*, 506(3):250 – 303, 2003.

[50] Judith F Briesmeister. *MCNP: a general Monte Carlo code for neutron and photon transport; version 3A*. Los Alamos Nat. Lab., Los Alamos, NM, 1986.

[51] L.J. Harkness, A.J. Boston, H.C. Boston, R.J. Cooper, J.R. Cresswell, A.N. Grint, P.J. Nolan, D.C. Oxley, D.P. Scraggs, T. Beveridge, J. Gillam, and I. Lazarus. Optimisation of a dual head semiconductor Compton camera using Geant4. *Nuclear Instruments and Methods in Physics Research, Section A: Accelerators, Spectrometers, Detectors and Associated Equipment*, 604(1-2):351–354, 2009. cited By (since 1996)13.

[52] S.W. Peterson, Robertson D., and J. Polf. Optimizing a three-stage Compton camera for measuring prompt gamma rays emitted during proton radiotherapy. *Physics in Medicine and Biology*, 55(22):6841–6856, 2010. cited By (since 1996)13.

[53] L.J. Harkness, P. Arce, D.S. Judson, A.J. Boston, H.C. Boston, J.R. Cresswell, J. Dormand, M. Jones, P.J. Nolan, J.A. Sampson, D.P. Scraggs, A. Sweeney, I. Lazarus, and J. Simpson. A Compton camera application for the GAMOS Geant4-based framework. *Nuclear Instruments and Methods in Physics Research Section A: Accelerators, Spectrometers, Detectors and Associated Equipment*, 671(0):29 – 39, 2012.

[54] David Scraggs, Andrew Boston, Helen Boston, Reynold Cooper, Chris Hall, Andy Mather, Paul Nolan, and Gerard Turk. Signal analysis and processing for SmartPET. *Nuclear Instruments and Methods in Physics Research Section A: Accelerators, Spectrometers, Detectors and Associated Equipment*, 573(12):95 – 98, 2007.